POLITECNICO DI MILANO
Corso di Laurea Magistrale in Ingegneria Aeronautica
Scuola di Ingegneria Industriale e dell'Informazione
Dipartimento di Scienze e Tecnologie Aerospaziali

Experimental analysis of turbulent flow in a drag-reducing device

Relatore: Prof. Marco Belan
Co-relatore: Prof. Franco Auteri
Co-relatore: Prof. Maurizio Quadrio

Tesi di Laurea di:
Domenico Marino, matricola 784217

Anno Accademico 2013-2014

C'est en faisant n'importe quoi qu'on devient n'importe qui.

Remi Gaillard

To my family

Contents

List of Figures

List of Tables

Abstract

The main aim of this work is the experimental analysis of the spatial transient at the outlet of a drag reduction device for the turbulent flow in a pipe. The reduction of turbulent friction is achieved by means of a streamwise travelling wave of spanwise wall velocity in a closed-circuit water pipe. The waves are generated by independent azimuthal oscillations of axial pipe slabs. The measurements of turbulent statistics are carried out by means of a single hot-film probe normal to the streamwise velocity, while the drag reduction rate is measured by means of a differential pressure transducer. The drag reduction rate is measured over a wide range of wave frequencies at two different wavelenghts; the mean streamwise velocity profile and the streamwise component of the Reynolds stress tensor are measured along the spatial transient region. The streamwise friction at the pipe wall and the turbulence statistics are largely attenuated by the waves and are in line with direct numerical simulation data. Eventually, turbulent energy spectra at the outlet of the active section of the pipe are measured at different frequencies and wavelengths of the wall forcing.

Keywords: Drag reduction, Streamwise travelling wave, Turbulent pipe flow, Hot-film anemometry, Spatial transient, Reynolds Stress

Sommario

Lo scopo principale di questa tesi è l'analisi sperimentale del transitorio spaziale che si genera in un flusso turbolento a valle di un dispositivo per la riduzione di resistenza. La riduzione della resistenza di attrito turbolenta è ottenuta tramite onde longitudinali viaggianti di velocità azimutale a parete. Le onde sono generate mediante rotazione indipendente dei diversi sottili segmenti nei quali è suddiviso il tratto di tubo. Pe r le misure di turbolenza è stata utilizzata una sonda a film singolo posizionata perpendicolarmente alla componente assiale della velocità del flusso, mentre la riduzione di resistenza è stata misurata a cavallo della sezione attiva attraverso un trasduttore differenziale di pressione. Le misure di riduzione di resistenza sono state svolte su un ampio intervallo di frequenze a due diverse lunghezze d'onda, mentre le misure di turbolenza sono state svolte lungo il transitorio spaziale. Lo sforzo d'attrito alla parete e le fluttuazioni di velocità sono ampiamente attenuati dalle onde viaggianti ed i risultati mostrano un buon accordo con le simulazioni numeriche. Come risultati finali vengono mostrati gli spettri di turbolenza misurati alla fine della sezione attiva del tubo per diverse frequenze e lunghezze d'onda della forzante.

Keywords: Riduzione di resistenza, Onde viaggianti, Flusso turbolento in un tubo, Anemometria a film caldo, Transitorio spaziale, Sforzi di Reynolds

Acknowledgments

First and foremost, I would like to express my sincere gratitude to my advisor Prof. Marco Belan, whose advices and insight have been invaluable to me. Without his continuous support, patience and knowledge this thesis would not have been completed.

I would really like to thank my co-advisor Prof. Franco Auteri for his kindness and willingness to help me with whatever problem I've had.

I would also like to thank my co-advisor Prof. Maurizio Quadrio for his precious advices on practical and theoretical aspects.

I am really grateful to engineer Donato Grassi and Roberto Berté, who provided assistance in numerous and fundamental ways.

I want to express my gratitude to my colleague Domenico Muti with whom I shared a good portion of the work.

Eventually I would really like to thank my colleagues and friends Antonello Nistoro, Andrea Natali, Nicola Rozzini and Federico Messanelli for their precious help and for the time spent together in the draft of our thesis.

Chapter 1

Introduction

In this chapter, the phenomenon of drag reduction is described. In section 1.1 a general overview of flow control techniques is provided. In section 1.2 the suppression of wall turbulence is illustrated in detail with particular attention to wall-motion techniques. Afterwards, in section 1.3, the experimental setup is briefly described and the drag reduction results obtained are provided. Eventually, in section 1.4 the thesis is outlined.

1.1 Flow control

1.1.1 Motivation

In the last two decades flow control has become one of the most interesting challenges in the field of fluid dynamics. Many flow control techniques, both passive and active, have been developed in order to improve several technological processes and to achieve economic and energetic benefits. Modern control systems are able to modify the flow field in order to obtain: lift increase, drag reduction, transition delay, separation suppression, noise suppression and turbulence enhancement. Some of those systems are still quite distant from any practical application mostly due to lack of efficiency: the economic and energetic cost is still too high with respect to achievable benefits. As sug-

gested by Gad-el-Hak in [1], flow control devices can be classified depending on energy consumption and control loop. As shown

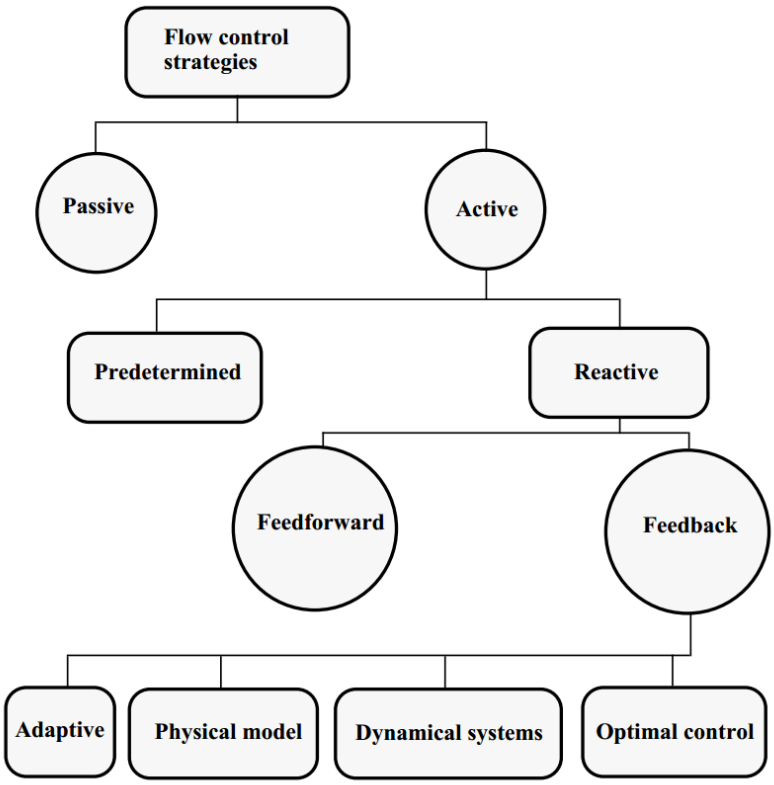

Figure 1.1: *Flow control strategies from Gad-el-Hak 2001 [1]*

in figure 1.1, control strategies can be roughly grouped into two categories: active, requiring energy consumption to control the flow such as plasma actuation and travelling-wave motion, and passive, where the goals are achieved without a direct energy input (riblets, polymers). Furthermore, active control systems can be classified into predetermined controls, which do not require any information about the flow field, and reactive, in which the flow state is suitably measured. Reactive controls can be further classified with respect to the type of control loop used: feedfowrward control, where the measured state is different from the regulated one, and feedback control, where the measured state

coincides with the regulated one. Nevertheless, choosing the control strategies is not easy because many important factors have to be taken into account:

- each flow shows peculiar features according to wall presence and properties, Mach number, Reynolds number and character of instabilities.
- many control strategies can be far more effective than others depending on the nature of the flow and on the goal to be achieved.
- the various control goals are closely linked to each other as depicted in Figure 1.2, and improving a specific performance does not systematically end up in a general performance improvement. The right balance between the desired flow behaviour and possible side effects of the control actuation must be obtained.
- the control system is subject to technological and economic constraints for its application.
- operating conditions may differ significantly from laboratory conditions and the control system has to be reliable and efficient in a wide enough working range.

As described by Leschziner et al. in [12], the best practical results achieved so far in flow control mostly concern:

- transition delay by means of active control strategies, using plasma-driven actuators, or by passive control strategies, that modify surfaces roughness.
- separation prevention and vortex shedding control by means of pulsed and synthetic-jet actuators.
- near-wall turbulence reduction by means of spanwise and travelling waves wall oscillations.

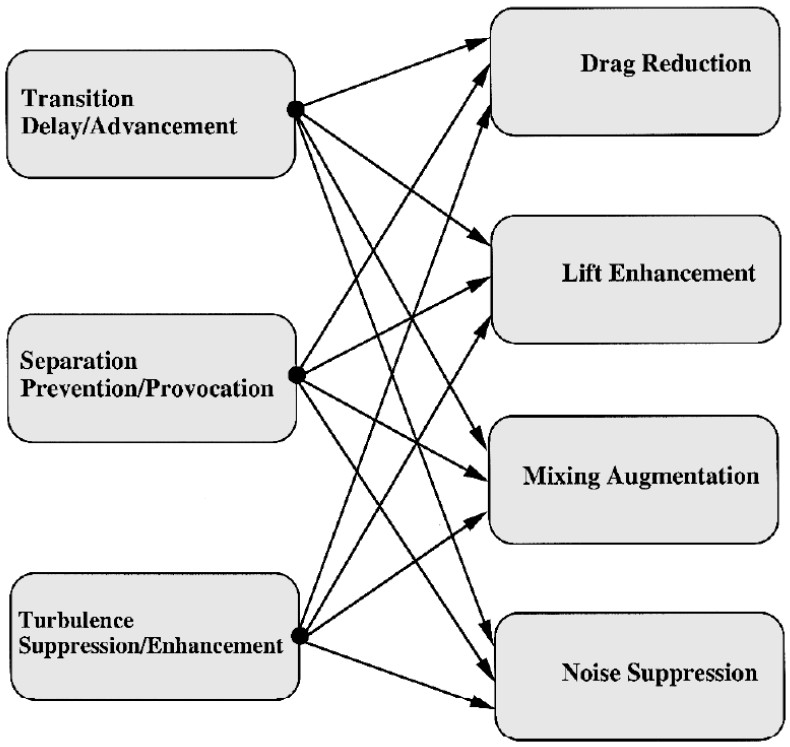

Figure 1.2: *Engineering goals and corresponding flow changes from Gad-el-Hak 2000 [2]*

This work will be focused on reducing near-wall turbulence to reduce friction drag.

1.1.2 Drag reduction

Drag reduction is one of the main goals of flow control and perhaps it is one of the most difficult because of the complexity of the physical phenomena involved. To better understand the working principles of the drag reduction, the drag force has to be decomposed in its different sources. As a first step, as shown in Figure 1.3, the total drag can be decomposed into:

- skin-friction drag, streamwise component of the total force due to tangential stresses acting on the body.

- pressure drag, streamwise component of the total force due to normal stresses acting on the body.

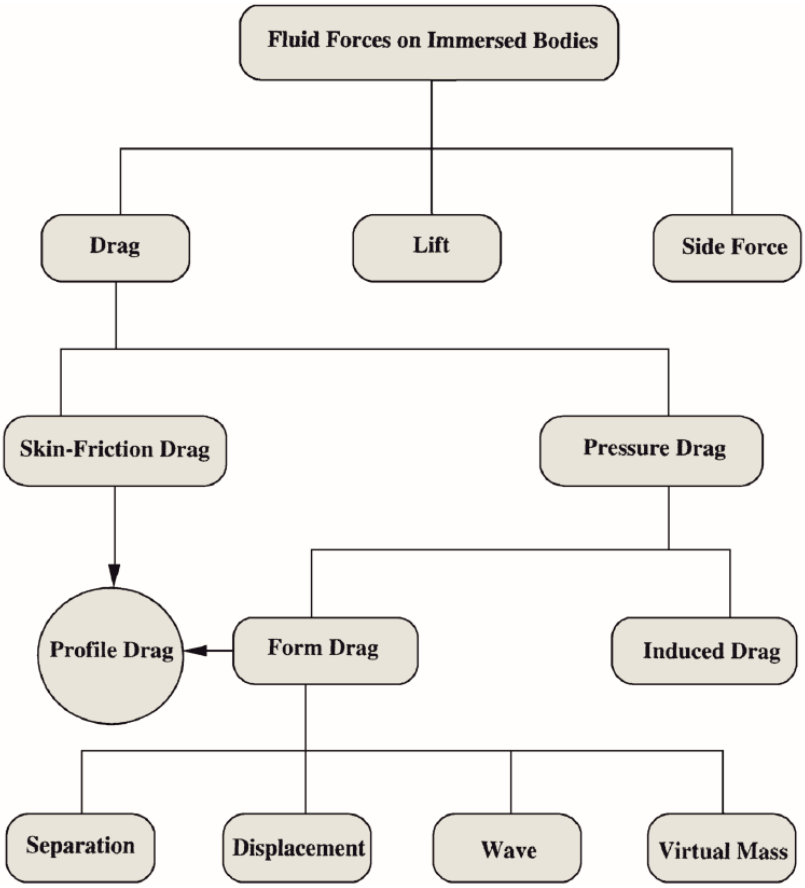

Figure 1.3: *Fluid forces on immersed bodies from Gad-el-Hak 2000 [2]*

As shown in Figure 1.2, drag reduction can be obtained in several ways:

- separation control leads to pressure drag reduction thanks to the reattachment of the flow.

- transition control means skin-friction drag reduction, because the skin-friction drag for a laminar boundary layer is lower than that of a turbulent one.

- near-wall turbulence suppression produces a decrease in the shear stress.

Depending on the properties of the flow some methods could be more effective than others. E.g. in wall-bounded flows, such as the channel and pipe flow, the near-wall turbulence suppression seems to be the only option.

1.2 Near-wall turbulence suppression

1.2.1 Turbulent structures

In order to obtain the desired drag reduction in wall-bounded flow, control devices have to alter the turbulent coherent structures. Coherent structures are regions of space and time, significantly larger than the smallest flow or turbulence scales, within which the flow field has a characteristic coherent pattern, as described by Pope in [13]. As analyzed by Kline and Robinson in [14], eight different quasi-coherent structures can be recognised in wall-bounded flows:

- Low-speed streaks
- Ejections of low-speed fluid outward from the wall.
- Sweeps of high-speed fluid toward the wall.
- Vortical structures.
- Strong internal shear layers.
- Near-wall pockets.
- Backs.
- Large-scale motions in the outer layers.

Although quasi-coherent structures have been widely analyzed by means of experimental and computational studies, their interactions and their contribution to turbulent drag are still not clear. Willmarth and Lu in [15] and Wallace et al. in [16] suggested that ejections and sweeps contribute a 80% of the total turbulent energy production. As depicted in Figure 1.4, ejections and sweeps are related to events in which the fluctuating velocities u and v have opposite sign.

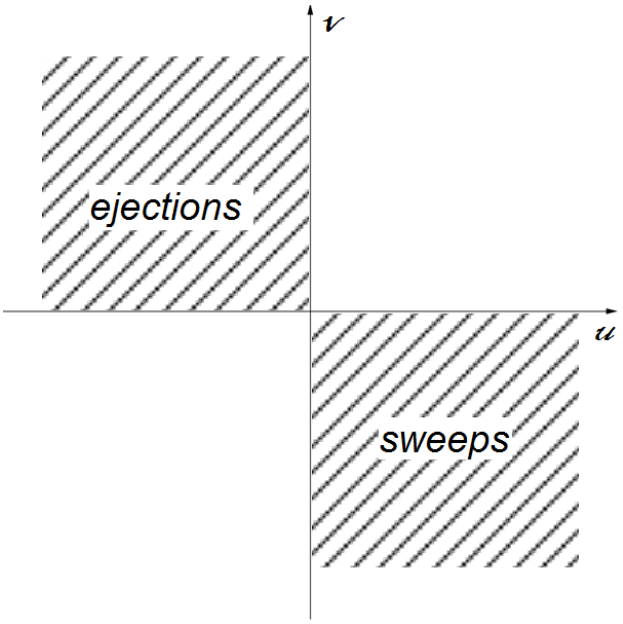

Figure 1.4: *Ejections and sweeps in the u-v sample space*

Kravchenko et al. [3] described a close relation between sweeps and turbulent wall-shear stress. As shown in Figure 1.5, streamwise vortices are mainly located in high skin-friction regions. In [17], Jimenez and Pinelli demonstrated that turbulence cycle is exclusively influenced by low-speed wall streaks and their interaction with near-wall quasi-streamwise vortices. The instability of wall streaks leads to quasi-streamwise vortices generation and similarly, streamwise vortices feed low-speed streaks. Interrupting this near-wall cycle is the main working principle of the most efficient drag reduction control systems. Near-wall

turbulence control devices must interact with structures that lie close to wall surface ($y^+<15$, where y^+ is the distance from the wall measured in viscous lengths) and thus riblets, wall-motion and plasma actuators seem to guarantee better results. From now on we will discuss transverse wall-motion control techniques only.

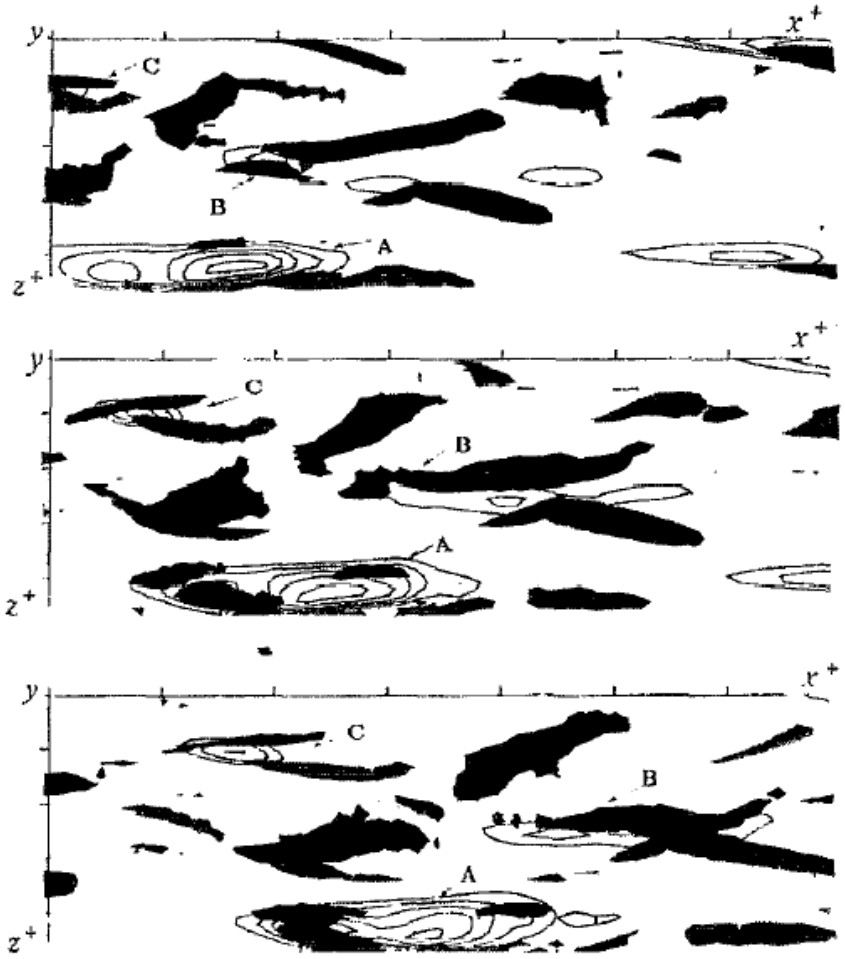

Figure 1.5: *Streamwise vortices (black and gray) and skin-friction region (contour lines) from Kravchenko et al.[3]*

1.2.2 Spanwise wall oscillations

A spanwise wall oscillation is perhaps the easiest wall-motion suitable for drag deduction. In case of channel flow, one or both the channel walls are moved in the spanwise direction as shown in Figure 1.6.

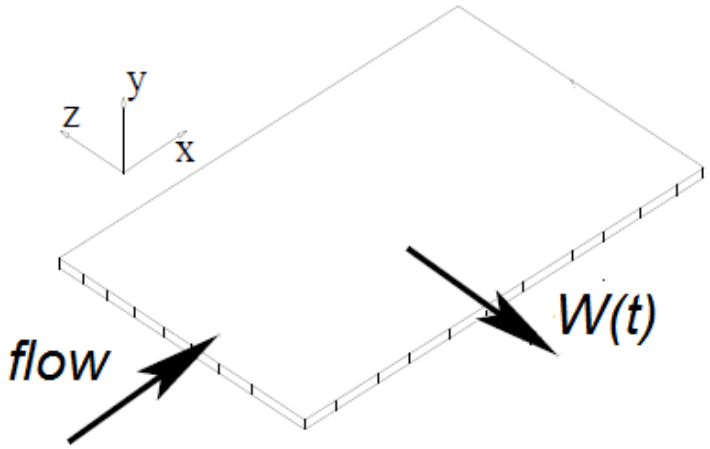

Figure 1.6: *Spanwise wall-motion in a channel flow*

The wall-motion is harmonic and can be described by the following law:

$$W(t) = A \sin\left(\frac{2\pi}{T} t\right) \tag{1.1}$$

where t is time, T is the oscillation period and A is the amplitude. In [4], Jung et al. were the first to study the possibility of suppressing wall turbulence by means of wall oscillation in order to obtain drag reduction. Wall turbulence quantities were investigated by direct numerical simulations in a plane channel flow subject to oscillating spanwise cross-flow or to oscillating spanwise motion of one of the channel walls. A reduction of the turbulence production and of the skin friction have been observed for different period of the wall oscillation. As shown in

Figure 1.7, there is a drop in the magnitude and in the number of turbulent events. With respect to the unperturbed turbulent channel flow, the drag has been reduced up to 40 % as shown in Figure 1.8. The results show that reductions of streamwise wall shear stress reductions are not transient. Furthermore, some frequencies lead to drag increase. The drag reduction depends on the amplitude of the oscillation too. The results were fully confirmed by Baron and Quadrio in [5]. As shown in Figure 1.9, a positive power balance $P_{net}(\%) = P_{saved}(\%) - P_{spent}(\%)$ is possible only if the amplitude of the oscillation is low.

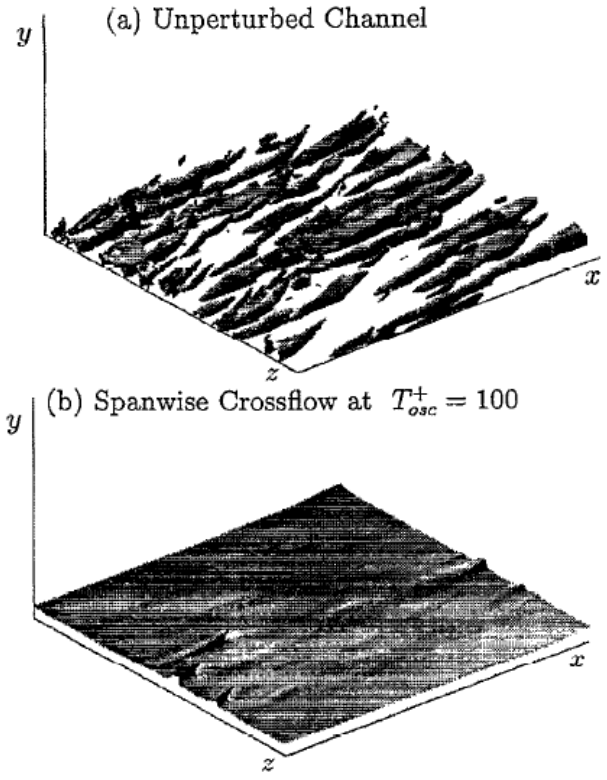

Figure 1.7: *Turbulence structures in the unperturbed channel compared to the structures in a channel with cross-flow oscillations. The turbulence structures are represented by contour surfaces of constant vorticity magnitude from Jung et al.[4]*

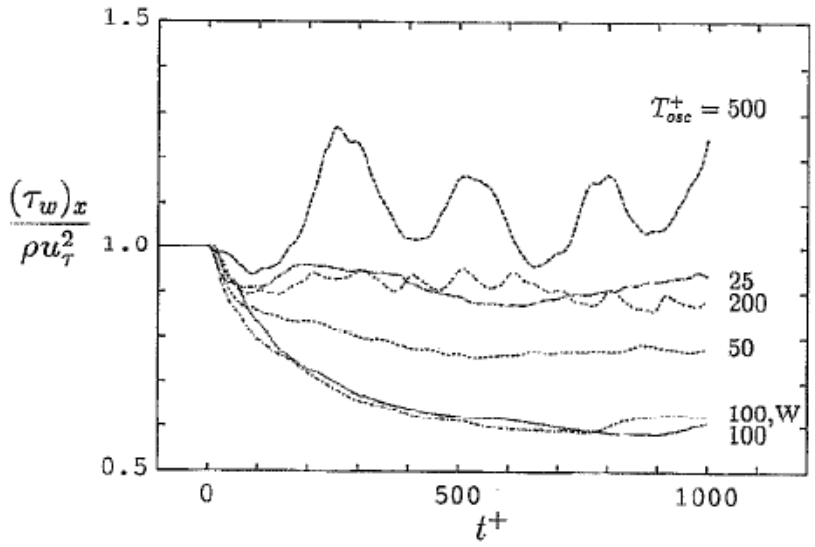

Figure 1.8: *Time evolution of the streamwise wall shear stress subsequent to the start of oscillations at various frequencies from Jung et al.[4]*

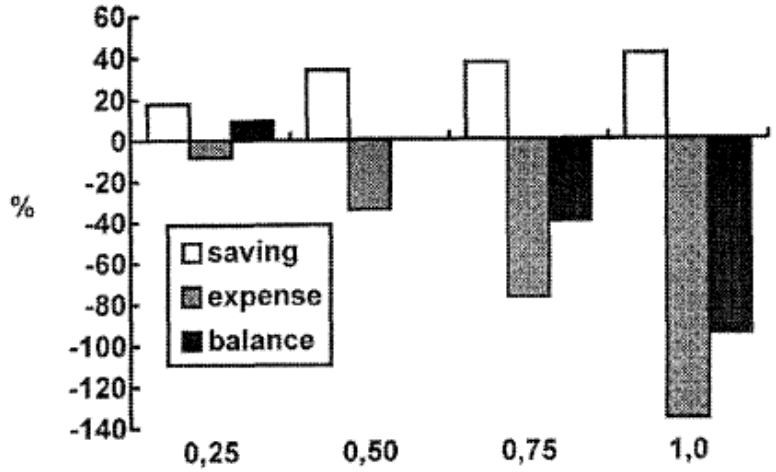

Figure 1.9: *Friction power saved (white); power spent to move the wall (grey); power budget (black) from Baron and Quadrio[5]*

Other direct numerical simulations were carried out by Quadrio and Ricco in [18], with a detailed analysis of the $A^+ - T^+$ space. Defining the percentage of drag reduction as:

$$\%DR = 100\frac{f_0 - f}{f_0} \tag{1.2}$$

where f_0 indicates reference flow friction factor and f the oscillating-wall one, they observed a drag reduction of up to 45% as shown in Figure 1.10.

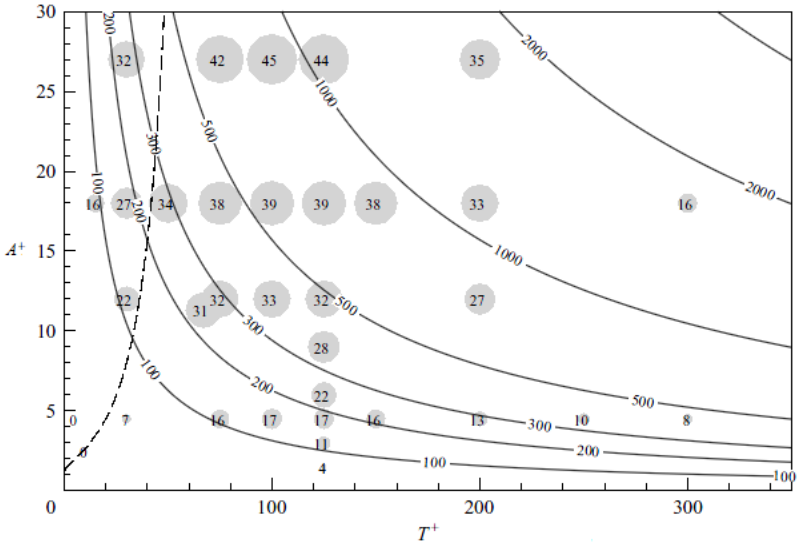

Figure 1.10: *Drag reduction percentage in the $A^+ - T^+$ space from Quadrio and Ricco[18]*

Taking into account the power required to move the wall, the maximum energy saving percentage reaches 7% as shown in Figure 1.11. Experimental investigations were carried out by Laadhari et al. in [19], who showed a reduction of the mean velocity gradient near the oscillating wall with a maximum drag reduction of 35%, and by Choi and Graham in [20], who showed a drag reduction up to 25% in a turbulent pipe flow, indicating lower drag reduction values than those shown by direct numerical simulations.

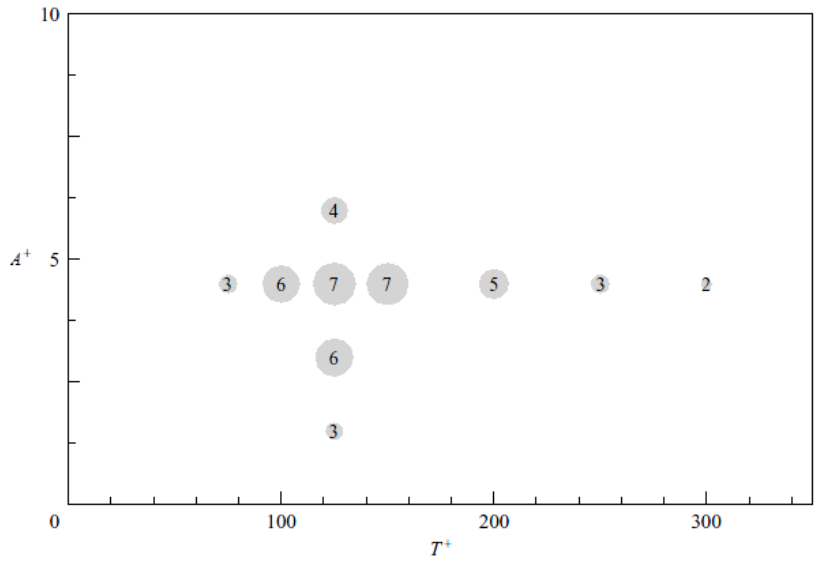

Figure 1.11: *Energetic saving percentage in the $A^+ - T^+$ space from Quadrio and Ricco[18]*

1.2.3 Streamwise oscillation of spanwise velocity at the wall

In the case of a streamwise distribution of spanwise velocity, a steady actuation can be employed as shown in Figure 1.12.

The steady wall-motion can be described by the following law:

$$W(x) = A \sin\left(\frac{2\pi}{\lambda_x} x\right) \tag{1.3}$$

where x is the streamwise coordinate and λ_x is the spatial wavelength of the distribution. In [6], Viotti et al. investigated by direct numerical simulations this type of steady forcing in a channel flow. The time scale is transformed into a length scale by means of the convection velocity U_w^+, whose value is constant and independent of the wall distance below $y^+ \simeq 15$ as described by Kim and Hussain in [21]. As expected, the optimal wavelength is:

$$\lambda_{x,opt}^+ = U_w^+ T_{opt}^+ \tag{1.4}$$

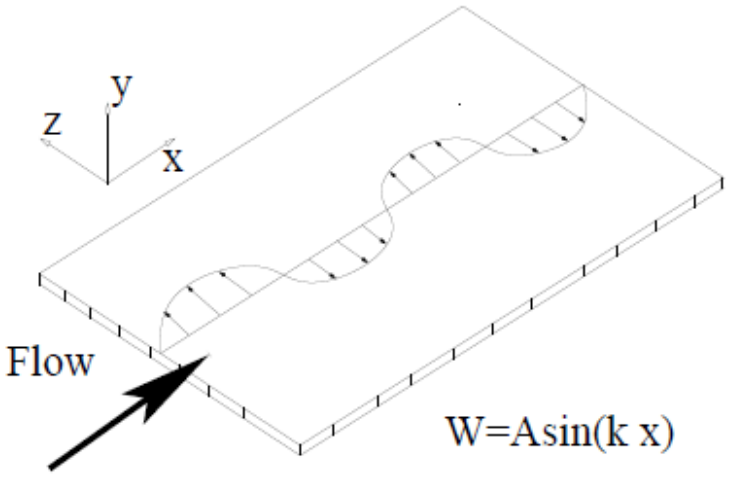

Figure 1.12: *Spanwise wall-velocity distribution in a channel flow from Viotti et al.[6]*

where T^+_{opt} is the optimum value of the oscillation period found in [4] and [18]. It is therefore possible to compare these results with those published by Jung and Quadrio as shown in Figure 1.13. From a comparison between temporal forcing and spatial forcing, it is clear that spatial forcing guarantees a larger drag reduction for a given wall-motion amplitude, up to 20-30% larger than the equivalent temporal forcing. The maximum drag reduction reached by Viotti et al. in [6] is about 52%. However, the maximum value lies in a region of the $A^+ - \lambda^+$ space in which the energy saving percentage is negative, and as shown in [4] and [18] the net power balance is positive only when the amplitude of the oscillation is comparable with the convective velocity U_w. As shown in Figure 1.14, the spatial forcing works better than the temporal one at fixed wall-oscillation amplitude, leading to a net power saving of 23% in the optimum case.

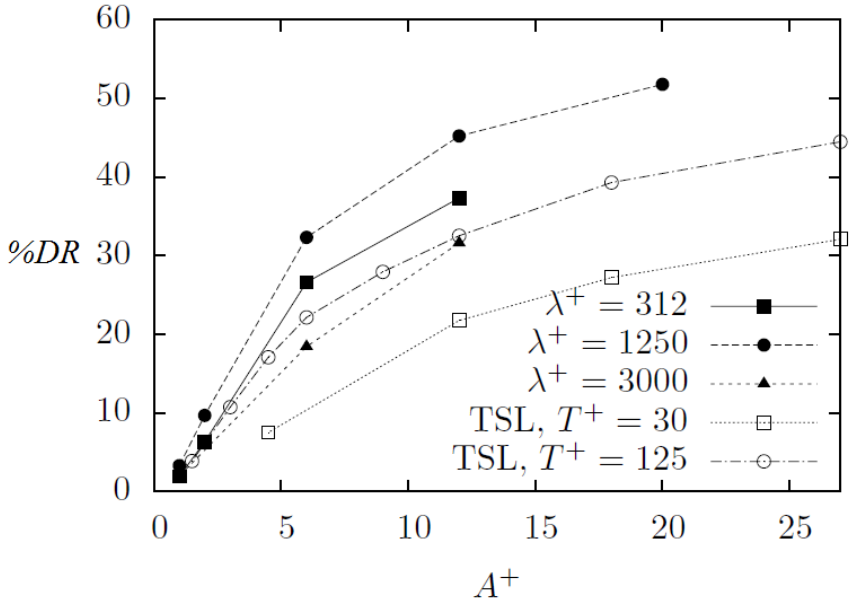

Figure 1.13: *Drag reduction percentage as a function of wall oscillation amplitude from Viotti et al.[6]. Empty symbols are temporal cases from Quadrio and Ricco [18] ($\lambda^+ = U_w^+ T^+$).*

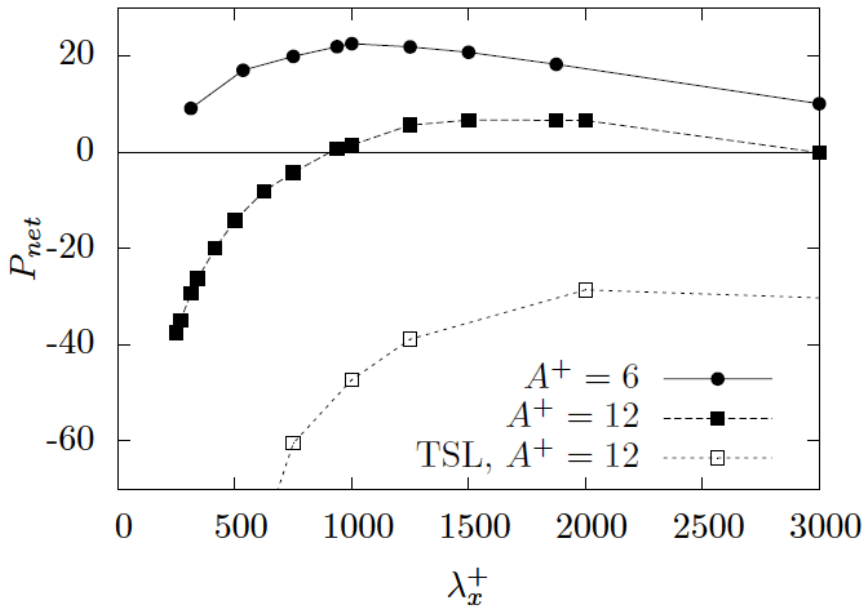

Figure 1.14: *Net power saving percentage as a function of wall oscillation wavelength from Viotti et al.[6]. Empty symbols are temporal cases from Quadrio and Ricco [18] ($\lambda^+ = U_w^+ T^+$).*

1.2.4 Streamwise-travelling wave

In [22], Du et al. introduced the concept of spanwise travelling wave forcing analyzing the effects of the following spanwise Lorentz force in a channel flow:

$$F_z(z,t) = Ie^{-y/\Delta} \sin\left(\frac{2\pi}{\lambda_z}z - \frac{2\pi}{T}t\right) \tag{1.5}$$

where I is the interaction parameter, λ_z is the wavelength in the spanwise direction, T the period of the oscillation and Δ is the distance from the wall where the force acts. As shown in Figure 1.15, a drag reduction of about 30% is observed.

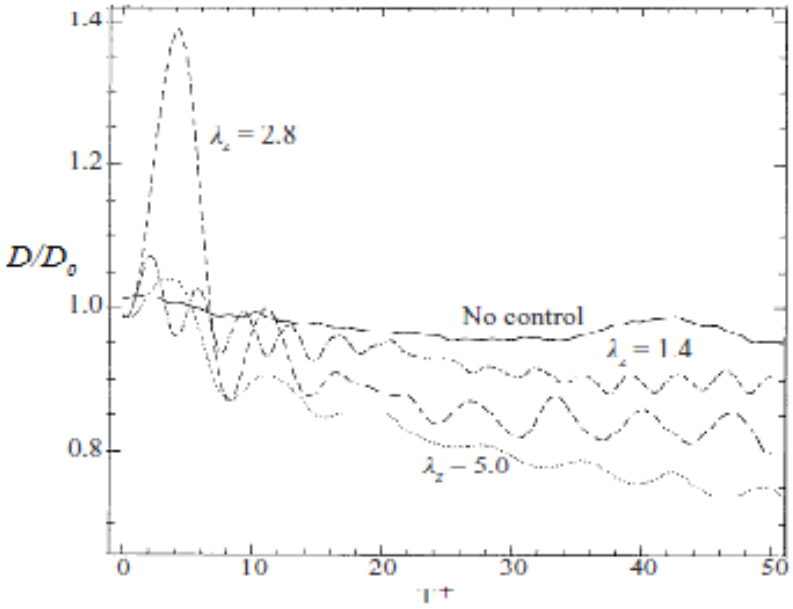

Figure 1.15: *Drag reduction percentage as a function of wall oscillation wavelength from Du et al.[22].*

In [7], Quadrio et al. proposed an extension of temporal and spatial forcing to the space-time case, imposing a time-dependent and streamwise-modulated sinusoidal wave of spanwise velocity at the wall as shown in Figure 1.16. The travelling

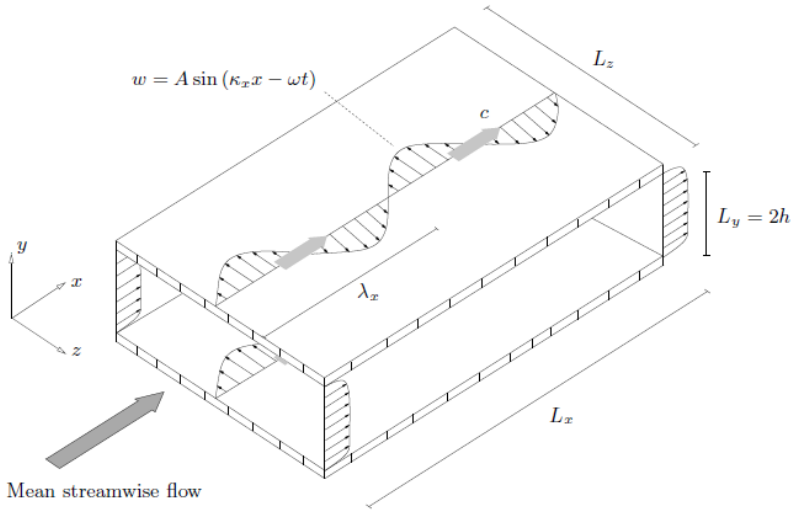

Figure 1.16: *Streamwise travelling wave in a channel flow from Quadrio et al.[7]*

wave is described by:

$$W_w(x,t) = A\sin(k_x x - \omega t) \tag{1.6}$$

where A is the amplitude of the wall oscillation, k_x is the wavelength in the streamwise direction, and ω is the oscillation frequency. The phase speed of the wave described by 1.6 is:

$$c = \frac{\omega}{k_x} \tag{1.7}$$

The percentage of friction drag reduction in the $k_x - \omega$ plane, at fixed Re and A, is shown in Figure 1.17. The region of drag reduction corresponds to a slow forward-travelling wave where $c \simeq 0.15$ and shows a maximum drag reduction of 47%-48%, against 45% of the steady wave and 34% of the oscillating wall. A region of drag increase occurs when the phase speed c is near the convection speed value $U_w = 0.5$. As shown in Figure 1.18, travelling waves are more efficient than steady waves and the oscillating wall. Thanks to the correspondence between the large drag reduction region and the minimum spent power region, travelling waves guarantee a maximum net energy saving

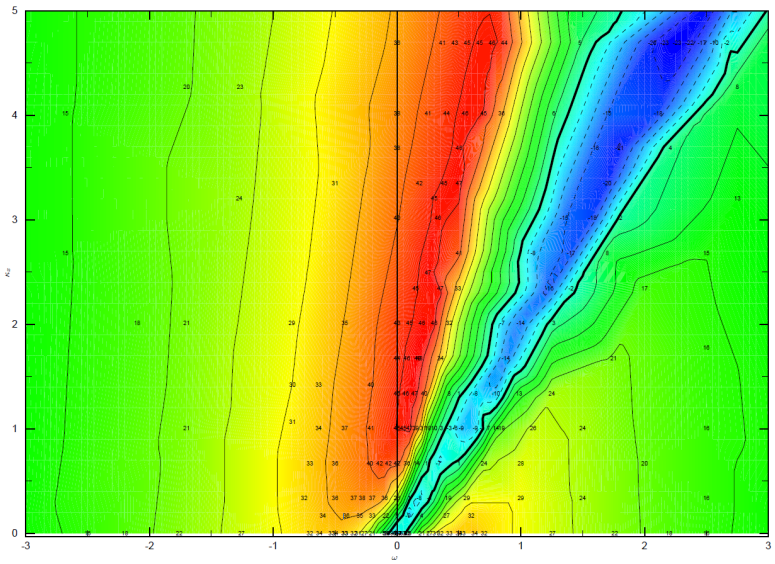

Figure 1.17: *Friction drag reduction percentage for $A = 0.5$ and $Re = 4760$ from Quadrio et al.[7]. Contours are spaced by 5% intervals, loci of zero DR are indicated by thick lines and negative values are represented by dashed lines.*

of 18% at Re and A fixed (in [6] and [5], at this value of A, the net power balance was 5% for steady wave and negative for oscillating wall).

Another interesting effect of travelling waves is their interaction with turbulent wall structures, whose behaviour is depicted in Figure 1.20. As described by Karniadakis and Choi in [23], when drag reduction occurs the wall-cycle of the turbulent structures is weakened, and the turbulent production is interrupted. In the drag increase case, there is a phase-lock between the turbulent wall-cycle and the wall waves, and thus turbulent production is enhanced. There is an increase in the intensity of the components of the Reynolds stress tensor when drag increase occurs, while a marked attenuation in the intensity is found in the case of drag reduction as shown in Figure 1.21. The mean velocity profile changes in the different situations as shown in Figure 1.19, with a huge change in the velocity gradient near the wall in the drag reduction case.

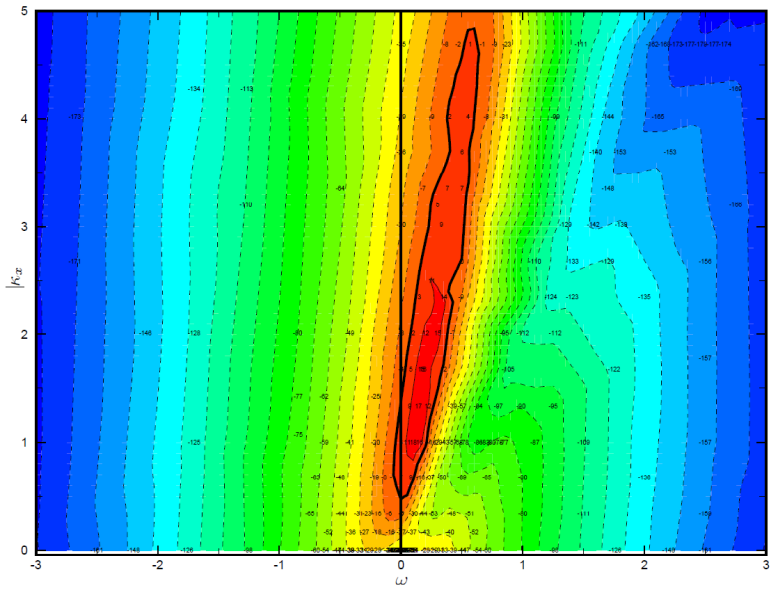

Figure 1.18: *Net power saving percentage for $A = 0.5$ and $Re = 4760$ from Quadrio et al.[7]. Contours are spaced by 10% intervals, locus of zero power saving is indicated by thick curve,solid lines denote positive balance, dashed lines denote negative balance.*

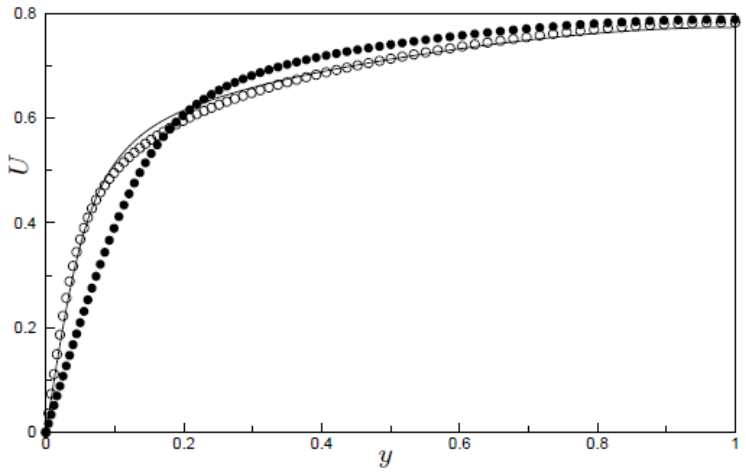

Figure 1.19: *Mean streamwise velocity: reference case (solid line), drag reduction (filled dots) and drag increase (empty dots) for $A = 0.5$ and $Re = 4760$ from Quadrio et al.[7].*

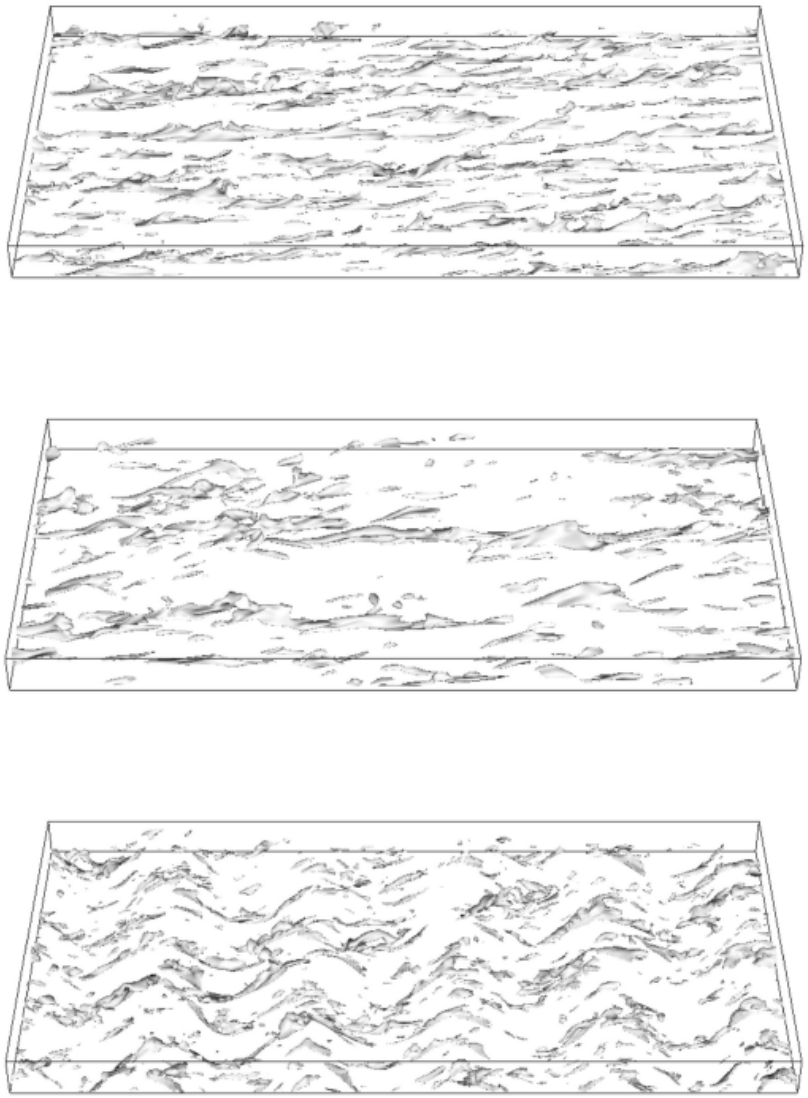

Figure 1.20: *Instantaneous flow field for the reference flow (top), drag reduction (middle) and drag increase (bottom) for* $A = 0.5$ *and* $Re = 4760$ *from Quadrio et al.[7]. Iso-surfaces for the quantity* $q = sgn(u)\sqrt{u^2 + w^2}$

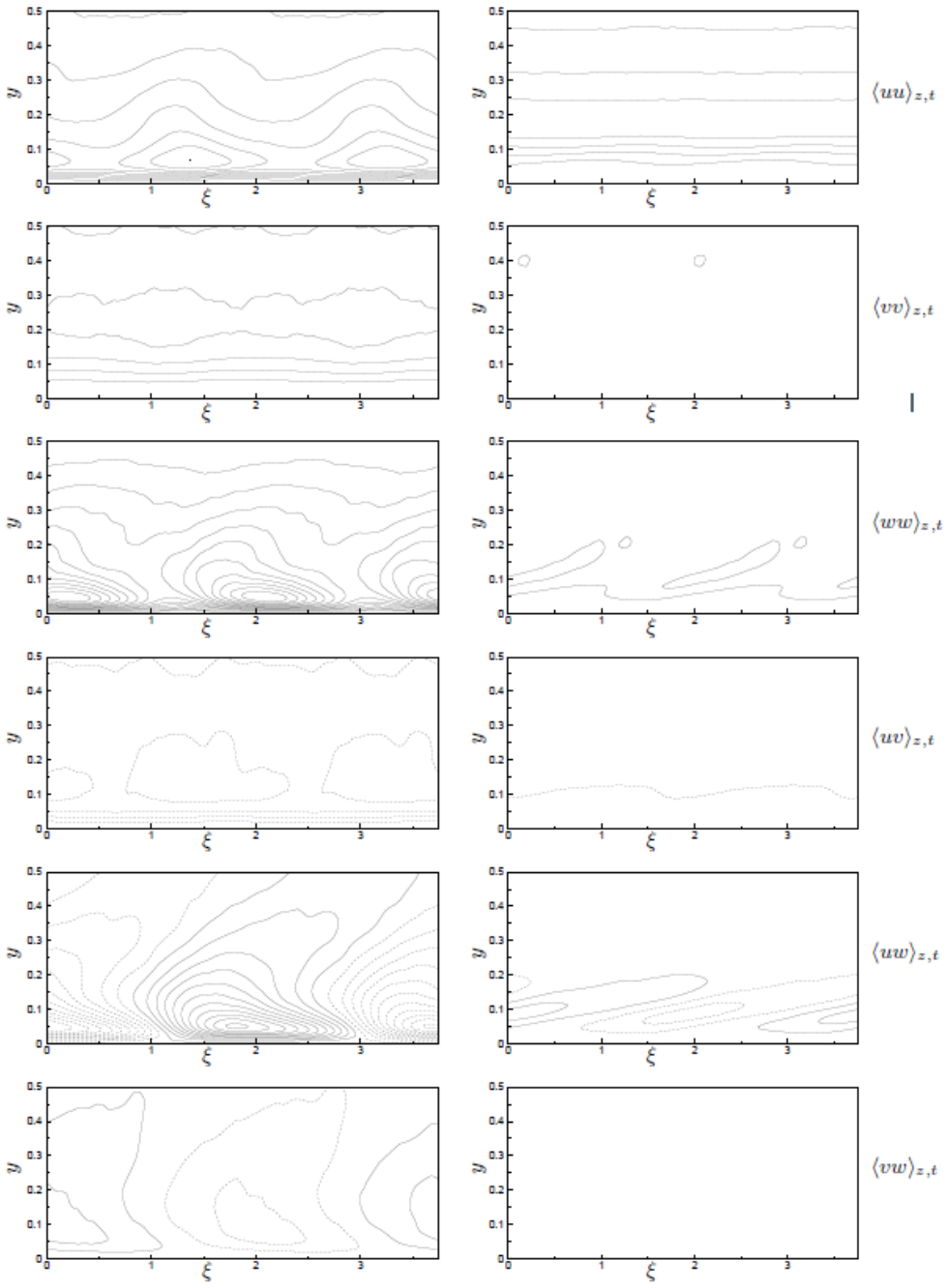

Figure 1.21: *Components of the Reynolds stress tensor: drag increase (left) and drag reduction (right) for* $A = 0.5$ *and* $Re = 4760$ *from Quadrio et al.[7].*

1.3 Drag reduction in a turbulent pipe flow

1.3.1 Experimental setup

An experimental facility has been designed in order to confirm the results obtained by Quadrio in [7] by means of streamwise travelling waves. Due to practical issues in the design of a reliable moving wall for a plane channel flow, a streamwise travelling wave device for a closed-circuit water pipe flow was realized instead, as shown in Figure 1.22. The active section has an inner

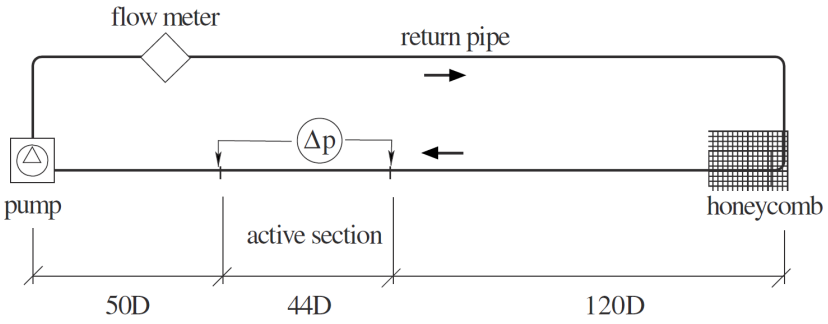

Figure 1.22: *Closed-circuit water pipe setup composed by an active section, a pump, a return pipe with a flow meter and an honeycomb from Auteri et al.[8]*

diameter $D = 50mm \pm 0.05mm$ and it is $44D$ long. In this case travelling waves are implemented by means of 60 rotating segments, that act as shown in Figure 1.23. The active section is connected to the pump by a straight, $50D$ long, aluminum pipe. A flow meter is placed in the return pipe to evaluate the bulk velocity , U_b and therefore the Re. A straight $120D$ long aluminum pipe, preceded by honeycombs to avoid swirl, guarantees a fully developed turbulent flow at the active section inlet. The pressure drop along the active section is measured to evaluate the friction drag reduction. The 60 segments are driven by six independent dc motors, so that every motor moves ten segments in phase. In this way the wavelength can be discretized by 2,3 or 6 segments (all segments moving in phase correspond to the os-

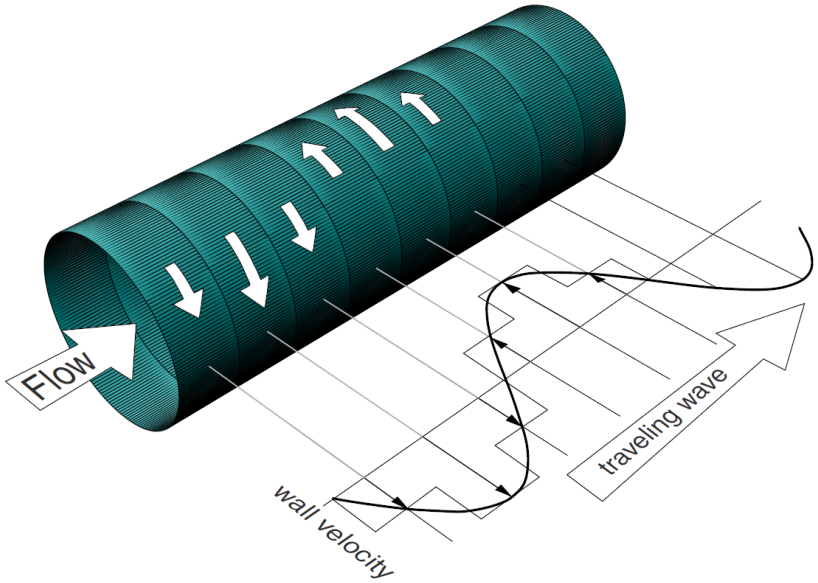

Figure 1.23: *Streamwise travelling wave implementation in a pipe flow from Auteri et al.[8]*

cillating wall). A thermocouple, located upstream of the pump, and an absolute pressure transducer are used to measure water thermodynamic properties. Further details of the experimental facility can be found in chapter 2.

1.3.2 Drag reduction results

In [8], Auteri et al. presented the results obtained in the facility described. The operating Reynolds number is $Re = 4900$ and the measured reference friction velocity is $u_\tau = 6.7mm/s$. The Karman number, based on the friction velocity and pipe radius, is $R^+ \simeq 175$.

The travelling wave wavelengths adopted in the experiments, normalized by the viscous length, are $\lambda^+ = 511$, $\lambda^+ = 766$ and $\lambda^+ = 1532$ corresponding to 2,3 or 6 independent segments, respectively. The frequency range adopted for the wave is $\omega = \pm 1.8Hz$, or, adimensionalized, $\omega^+ = \pm 0.20 - 0.25$ while the amplitude value is $A^+ = 13.8$. The experimental region is

indicated by dashed lines in Figure 1.24.

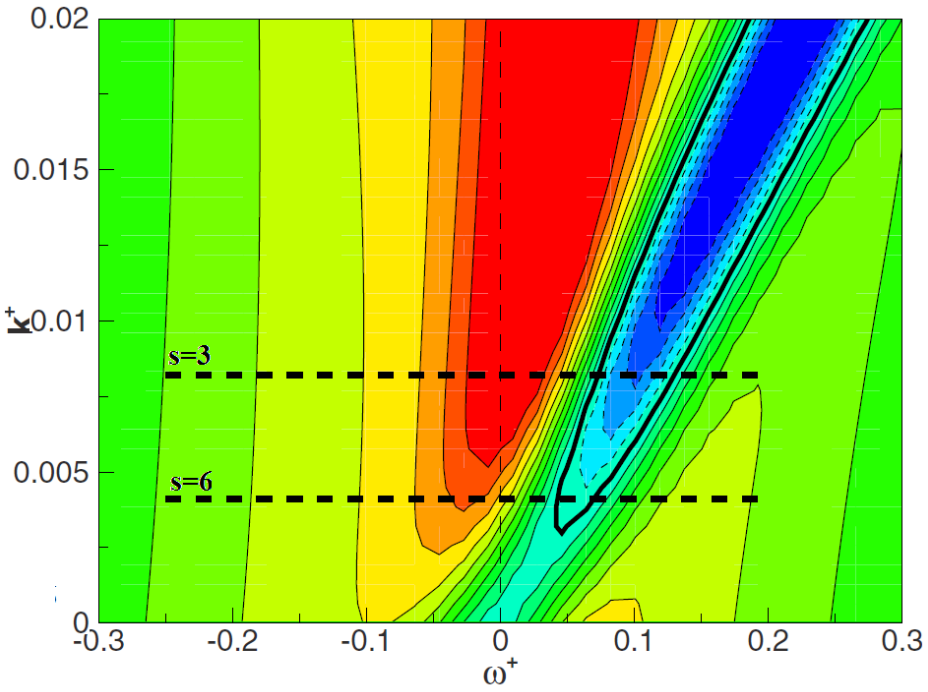

Figure 1.24: *Discretized wave number in the $k^+ - \omega^+$ plane from Auteri et al.[8].*

In Figure 1.25, the drag reduction rate obtained with 3 and 6 independent segments, that guarantee a better discretization of the wave, is illustrated.

At a qualitative level, the results show good agreement with DNS data. The drag reduction rate depends strongly on the frequency and wavelength of the travelling waves. As expected from DNS analysis, the maximum drag reduction rate for the wave discretized with 6 independent segments is observed for a steady-wave, while a 3 segments discretization shows a reduction of up to 33% in the region of slow travelling waves. Although there is a good correspondence between the DNS parameters from [7] and the adopted experimental parameters, drag increase was not observed experimentally. As shown in Figure 1.26, there is a large drop in drag reduction, but still no drag increase, in correspondence of the drag increase zone caught by DNS, where

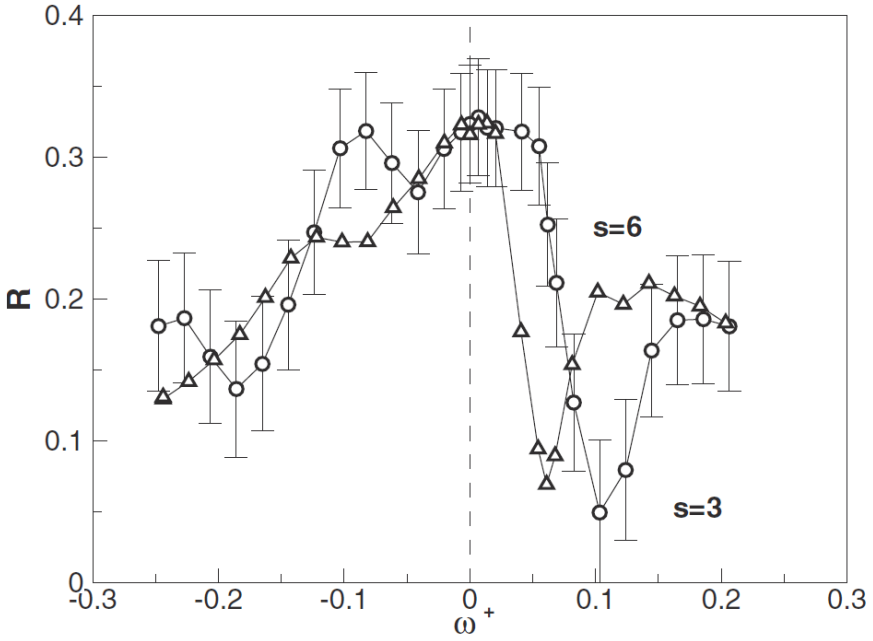

Figure 1.25: *Drag reduction at different oscillation frequencies from Auteri et al.[8]. Wave discretized by 3 segments (circles) and 6 segments (triangles). Bars correspond to uncertainties in the measurements.*

the phase speed is $c^+ \simeq 12$.

The reasons for the mismatch between numerical and experimental data, at a quantitative level, have been attributed to:

- the different geometry and hence a different behaviour of near-wall turbulent cycle.

- the presence of a spatial transient at the beginning of the active section of the pipe. For this reason drag reduction, and thus drag increase, is not fully developed in the initial region of the active section and consequently its magnitude is lower than expected from DNS data.

- spatial discretization of the wave (further details can be found in [8]).

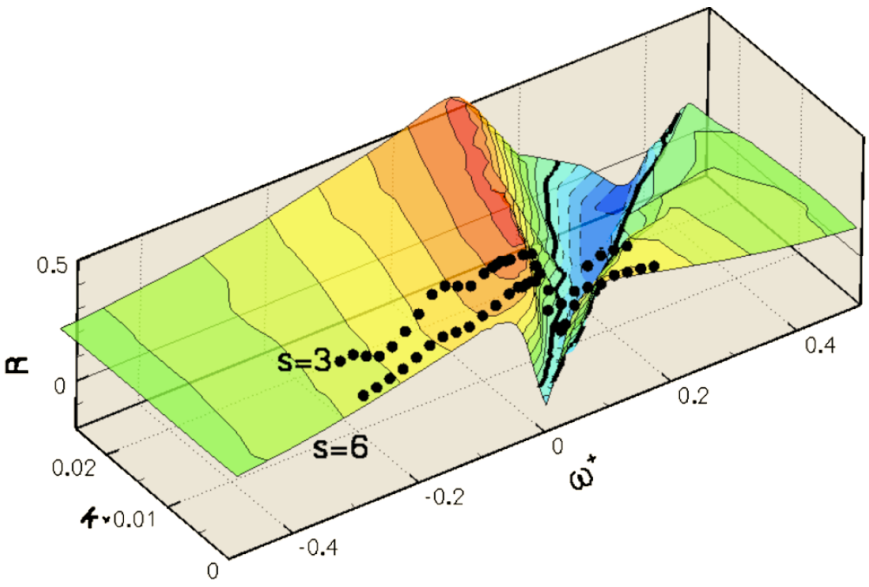

Figure 1.26: *Drag reduction rate in the $k^+ - \omega^+$ plane from Auteri et al.[8]. A comparison between DNS data from [7] and experimental data.*

1.4 Outline of the thesis

The aim of our facility is to reduce the skin friction drag of a turbulent flow by means of near-wall turbulence active control. It is interesting to analyse the mechanisms responsible for turbulent skin friction reduction. A detailed analysis of the spatial transient downward to the end of the active section of the pipe, where the controlled flow slowly changes into the unperturbed turbulent flow, can provide us with interesting information about the influence of streamwise travelling wave on turbulent structures. The thesis work is organised as follows. In chapter 2 the experimental facility is described. Every component of the closed-circuit water pipe will be presented, with a careful look at the active section and its actuation system and to the hot film support and its positioning system. A detailed description of instrumentation and data acquisition system is provided. Eventually, the filling procedure and maintenance of the facility are illustrated in order to simplify possible future

operations. In chapter 3 issues concerning the hot-film probe equipment placement are reported. The encountered problems are explained together with the detailed troubleshooting procedure necessary to obtain a safe displacement of the probe. Then the equipment placement calibration procedure, in both the radial and axial direction, is analyzed in order to identify a repatable positioning procedure. Finally the assembling procedure of the equipment is illustrated. In chapter 4 the hot-film anemometry is described with a survey of its working principle and some indications about its practical use. The directional sensitivity of a single wire probe is described with particular attention to the turbulent pipe flow. Eventually, the calibration and thermal correction procedures are illustrated. In chapter 5, the drag reduction results are illustrated and compared to other experimental and numerical data. The spatial transient is analyzed and the friction coefficient along the streamwise direction is evaluated. Finally turbulent kinetic energy spectra are illustrated at different frequencies and wavelengths of the travelling wave. In chapter 6 the obtained experimental results are discussed and possible future developments of the experimental campaign are suggested.

Chapter 2

Experimental facility

In this chapter the experimental facility is described in detail. In section 2.1 every component of the closed-circuit water pipe will be presented, with a careful look at the active section and at the hot-film support. Descriptions of instrumentation and data acquisition system are provided in section 2.2 and 2.3 respectively. Eventually in section 2.4 the filling procedure and maintenance of the facility are described. Further information about the facility can be found in [24] and [9].

2.1 Mechanical components

As described in section 1.3 and as shown in Figure 1.22, the experiment will be carried out in a closed-circuit water pipe flow.

2.1.1 Active section

The active section, where the travelling waves are generated, represents the core of our facility. It is made up of 60 segments, each one of 36.5 mm in length with an inner diameter of 50 mm. As shown in figure 2.1, each rotating segment is mounted on two bearings and is provided with a cogwheel. A 50-100 μm gap, filled with water-resistant grease, between each segment has been designed in order to avoid friction and consequent damages.

Of course o-rings are located at the interfaces of the segments. The segments are fixed over a ground rail of 2200 mm in length by means of 61 bearing housings, and driven by six dc motors by means of 60 belts. Each motor driven shaft hosts 10 cogwheels in order to control a maximum of 10 segments per shaft. The six driven shafts are supported by 36 slides fixed on six supporting portals. In order to avoid any interference the even motors are mounted upstream the active section while the odd motors downstream.

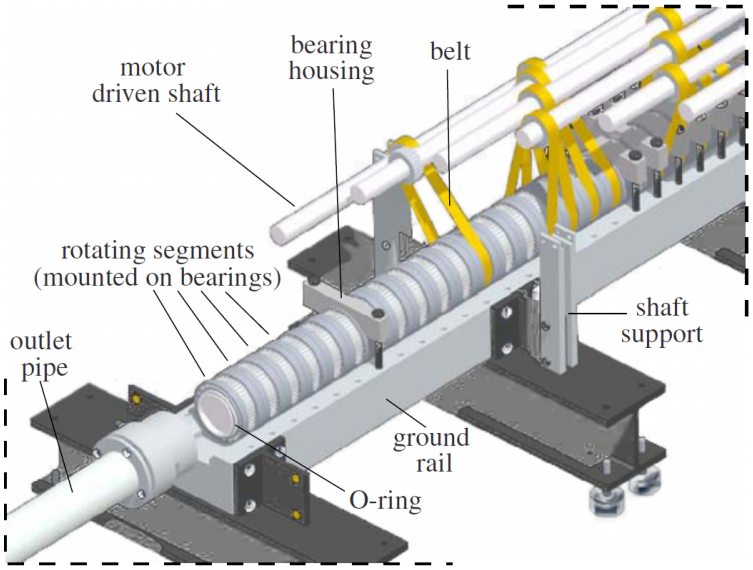

Figure 2.1: *The active section of the pipe and its main components from Auteri et al.[8]*

2.1.2 Hot-film probe support

An outlet aluminum pipe of 3 m in length with an inner diameter of 50 mm is located downstream of the active section. The hot-film probe support is placed along this pipe immediately after the active section. As shown in Figure 2.2 the probe is mounted on an extensible shaft that is free to slide in the steel

main shaft. The backward axial motion of the extensible shaft is provided by a steel cable fixed to a calibrated wheel: rotating the wheel the probe can be placed in the desired axial position and afterward the wheel can be secured by means of a screw. The forward motion is guaranteed by means of 2 springs that push the shaft forward once the wheel is released. The probe is fixed to an aluminum support, placed at the extremity of the extensible shaft, by means of a grab screw. In order to guarantee a radial motion of the probe, two vertical supports are connected to the main shaft. Two vertical rods are screwed in two supporting bushings located on the main shaft: the steel pulling cable and the electrical cable of the probe go through the rear and frontal vertical support respectively. Two press fit bushings act as interface between the support system and the pipe. The vertical rods are secured to a transverse beam that is moved by means of a stepper motor with a 2.5 μm step, secured to the pipe. In Figure 2.3 the interface between the probe support and the active section is shown.

2.1.3 Centrifugal pump and return pipe

The centrifugal pump that moves the water across the circuit is located at the end of the aluminum straight pipe. The circuit is filled with water by a vent located upstream of the pump, while a valve allows discharge of the facility.

A vertically moving reservoir linked to the circuit driven by a stepper motor guarantees an internal pressure higher than the external one in order to prevent air bubble and grease from being sucked in the circuit.

The return pipe is composed of two different ducts: a semi-rigid pipe with an inner diameter of 42 mm, where the flow meter is located, and a straight aluminum pipe, 6 m in length, with an inner diameter of 50 mm, in order to guarantee a fully developed

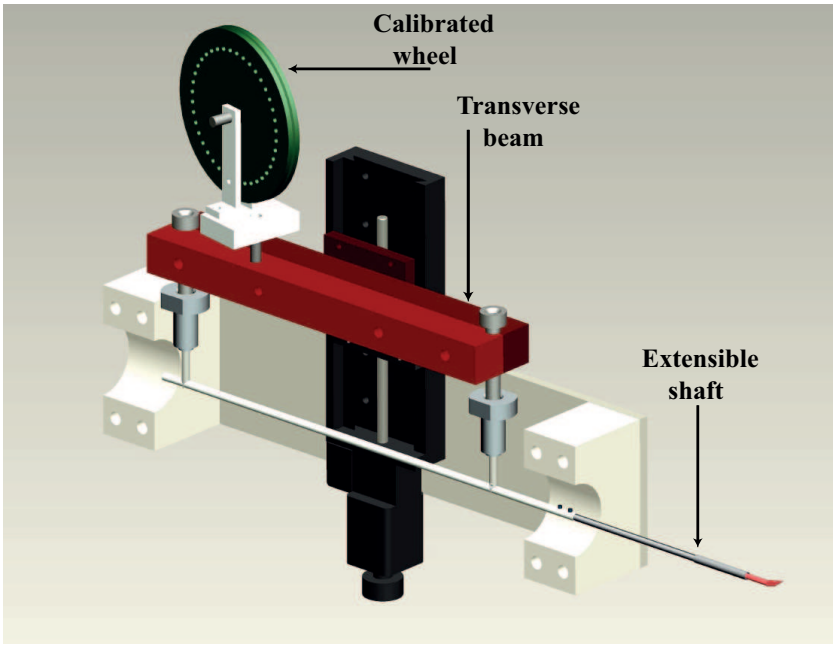

Figure 2.2: *The hot-film probe support equipment from [9]*

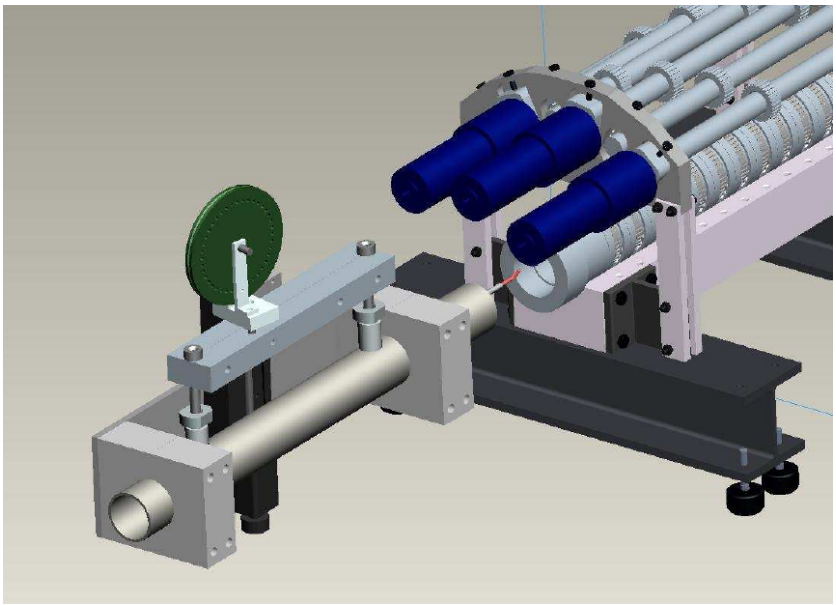

Figure 2.3: *Interface between the hot-film probe support equipment and the pipe from [9]*

turbulent flow at the inlet of the active section. Honeycombs are located at the inlet of the straight aluminum pipe in order to

avoid any swirl of the flow.

2.2 Instrumentation

Several sensors are placed along the water circuit in order to collect the maximum number of information about the fluid state and thus compute the real Reynolds number of the pipe flow:

- A Siemens MAG5100W electromagnetic flow meter with accuracy of 0.2% is located in the return pipe in order to measure the flow rate and therefore the bulk velocity.
- A PT100 thermocouple with accuracy of $\pm 0.2K$ is placed upstream of the pump. The value measured is used to compute water kinematic viscosity.
- A Druck RPT410 barometric pressure sensor with accuracy of $\pm 50Pa$ is used to measure the absolute pressure in the facility and to compute water kinematic viscosity.
- A Druck LPM9481 differential pressure sensor measures the head loss coefficient along the active section of the pipe.
- Six dynamos located on the driven shafts of the dc motors are used in order to give a feedback about the real shaft angular velocity and therefore adjust the frequency of the travelling waves.
- A Dantec 55R15 boundary-layer hot-film probe is used to measure the local velocity of the flow in the spatial transient generated by the travelling wave downstream of the active section.

Sensors specifications are presented in table 2.1.

Table 2.1: *Sensors specifications*

Druck LPM9481 differential pressure sensor				
Op.range$[Pa]$	**Op.range**$[K]$	**Accur.**$[Pa]$	**Resol.**$[Pa]$	**Resp.time**$[ms]$
$-20 \div 20$	253.15-353.15	$0.1\%FS$	Infinite	10
Druck RPT410 barometric pressure sensor				
Op.range$[MPa]$	**Op.range**$[K]$	**Accur.**$[Pa]$	**Resol.**$[Pa]$	**Freq.res.**$[Hz]$
$0.06 \div 0.11$	233.15-333.15	± 50	1	3.33
Dantec 55R15 boundary-layer hot-film probe				
Op. range$[m/s]$	**Max temp.**$[K]$	**length**$[mm]$	**dia.**$[\mu m]$	**Freq.res.**$[kHz]$
$0.01 \div 10$	373.15	1.25	70	30
Siemens MAG5100W flow meter				
Op. range $[m/s]$	**Max pressure**$[MPa]$	**Accuracy**[%]	**Freq. res.** $[kHz]$	
$0 \div 10$	1.6	0.2	10	
PT100 thermocouple				
Operating range $[K]$	**Accuracy** $[K]$	**Response frequency** $[kHz]$		
$173.15 \div 273.15$	± 0.2	1		

2.3 Data acquisition system

A computer controls the whole facility by means of a purposely designed LabVIEW software that manages data stream of the digital interface chassis NI PXI-1010. The chassis hosts several signal acquisition and control modules:

- NI PXI-6733: analog control, 16 bits resolution, 8 analog output channels.
- NI PXI-6284: data acquisition, 18 bits resolution, 32 single-ended channels, 625 *kS/s* sample rate.
- NI PXI-6123: data acquisition, 16 bits resolution, 8 simultaneously sampled analog inputs , 500 *kS/s* sample rate.
- NI PXI-2567: relay driver, 64 channels.

The NI PXI-6733 module controls the six dc motors and the pump inverter. The six analog outputs to control the motors are handled by six closed-loop power amplifier: the six dynamo outputs, that provide information about shafts real angular velocity, are used in an analog control loop. The dynamo outputs are also acquired by NI PIXI-6284 and used as feedback by a digital control loop in order to increase the accuracy of the angular velocity of the shafts. The NI PXI-6123 module acquires thermocouple, flow meter, pressure sensor and hot-film probe signals. The hot-film signal is amplified by an A.A.Lab anemometer and then acquired. Finally the NI PXI-2567 controls the relay to lift and lower the vertically moving reservoir. A block diagram of the experimental setup is shown in Figure 2.4.

2.4 Filling procedure and maintenance

The filling procedure of the facility is obviously critical in order to obtain a fully developed turbulent flow. First of all, all

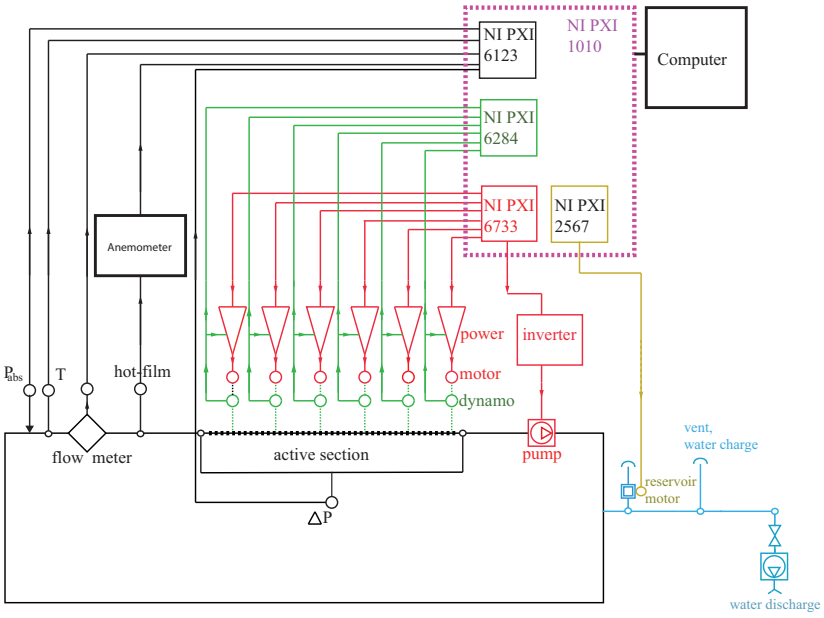

Figure 2.4: *Block diagram of the experimental setup.*

pressure taps must be closed and the drain valve of the circuit must be shut off. The air relief valves have to be opened in order to allow air to escape from the circuit during the filling procedure. The circuit has to be filled with de-ionized water to protect the hot-wire probe and the pressure sensor. The filling phase must be very slow in order to avoid the formation of air bubbles in different sections of the circuit. For this reason the semi-rigid pipe must be manually moved so that air bubbles are collected in correspondence to the main vent. Once the circuit is almost full of water the air relief valves must be closed and the pump has to be powered up in order to remove residual air microbubbles from the facility. Once the pipes are full of water the differential pressure transducer can be carefully filled with water. A cathodic protection of the whole facility is essential to prevent galvanic corrosion at the contact surfaces between aluminum and steel pipes. Thus every time the facility is shut off a copper bar, connected to a power supply, is immersed in the water and acts as anode while the metal components act as

cathode. A centrifugal pump, connected to the drain valve, is used to empty the circuit in the discharging phase. Once the facility is empty a complete opening of the circuit in correspondance of the pipes joints is preferable in order to prevent any water stagnation. After periods of long inactivity of the facility the tachymetric dynamos have to be recalibrated: a photodiode is located in correspondence with the black and white strips placed over the motors shafts in order to measure the real angular velocity. The real angular velocity is then related to the dynamo output.

Chapter 3

Experimental setup tuning

In this chapter issues about hot-film probe traversing system are reported. In section 3.1 all problems found are shown and in the different subsections their causes and the improvements brought, in order to obtain a safe and repeatable displacement of the probe, are explained in detail. Then in section 4.3 the traversing system calibration procedure in both the radial and axial direction is analyzed. Eventually in section 3.3 the assembling procedure of the equipment is illustrated.

3.1 Hot film support issues

During the first maintenance of the facility we faced several problems connected to the probe positioning equipment shown in figure 2.2. A bad, and sometimes impossible, movement of the probe in the spatial transient region was found. The principal issues were:

- Faulty axial movement because of friction of the springs against the extendible shaft, preventing the elastic response of the springs.
- Insufficient radial movement to analyze the near-wall region because of the vertical shift of the shaft in elongated position.

- Instability of the probe equipment due to unreliability of the front vertical support of the main shaft.

- Impossibility to retract the hot-film probe cable, resulting in a danger for the probe head.

- Press fit bushings migration after a movement of the motorized beam.

- Vertical support sliding through the transverse beam resulting in an unrepeatable radial motion.

3.1.1 Axial motion

The shaft axial motion turned out to be faulty, as the possible run was about 5 cm. This issue was related to two springs in series placed over the extensible shaft: in order to make them work properly, the springs ends have been closed and squared, avoiding unwanted overlaps. The springs inner diameters were too narrow to permit a free sliding of the extensible shaft, especially for the shorter spring. We decided thus to use open-ended springs, placing an empty steel cylinder between the springs with the aim to prevent overlaps, as shown in Figure 3.1. The cylinder is 5 mm in length, with an inner nominal diameter of 5 mm and an outer one of 7 mm. In order to extend the axial motion of the shaft, we eventually modified springs configuration adopting three springs and two cylinders instead of two springs and one cylinder: the total length of the three springs and two cylinders in the compressed configuration was 1 cm shorter than in the previous arrangement. The introduction of these improvements has led to a safe and repeatable axial motion up to 18 cm in the region of interest.

3.1.2 Radial motion

The supporting rods of the main shaft were designed in order to guarantee a total radial run of 25 mm. This run allowed us to examine the region of interest only in the total compressed springs configuration, in which the extensible shaft is not affected by the vertical shift due to mechanical play between the main shaft and the extensible one. The probe requires a total run of 28 mm in order to reach the wall from the pipe centerline when the probe is near the first rotating segment of the active section, where the maximum vertical shift of the shaft occurs. For this reason we decided to design new longer vertical rods in order to guarantee a total radial run of 28 mm. The new rods allow us to act on the turns of the screw between rods and bushings in order to align properly the shaft with the pipe centerline.

3.1.3 Shaft stability

In order to retract the hot-film electric cable throughout the front support of the shaft, we decided to realize a new steel front supporting bushing with an outer diameter of 16 mm instead of the 12 mm of the previous bushing. We machined the new bushing in such a a way as to make the cable free to move, as shown in Figure 3.2. The front bushing has been eventually glued to the support shaft by means of an epoxy resin with a resulting shaft support stable and easier to assemble than the previous one.

3.1.4 Electrical cable

The Dantec electrical cable of the hot-film probe was damaged as a result of the older tests and the retraction was difficult even with the new bushing. Because of the size of the cable and

of the throughout hole we were unable to insert a PVC runner in order to have an easier sliding. We chose thus to not retract the cable solving at the same time two other issues: the Dantec cable was too stiff, preventing a repeatable radial motion, and it could damage the probe head after the compression of the springs. We replaced thus the portion of Dantec cable upon the motion shaft with a flat cable, extremely flexible, that does not influence the radial motion. We have welded the two cables, sealed the area with silicone and then covered it by heat shrink tubings to avoid any water infiltration. The cable was then fixed to the main shaft with a clamp, in order to avoid any interaction with the radial motion, as shown in Figure 3.2.

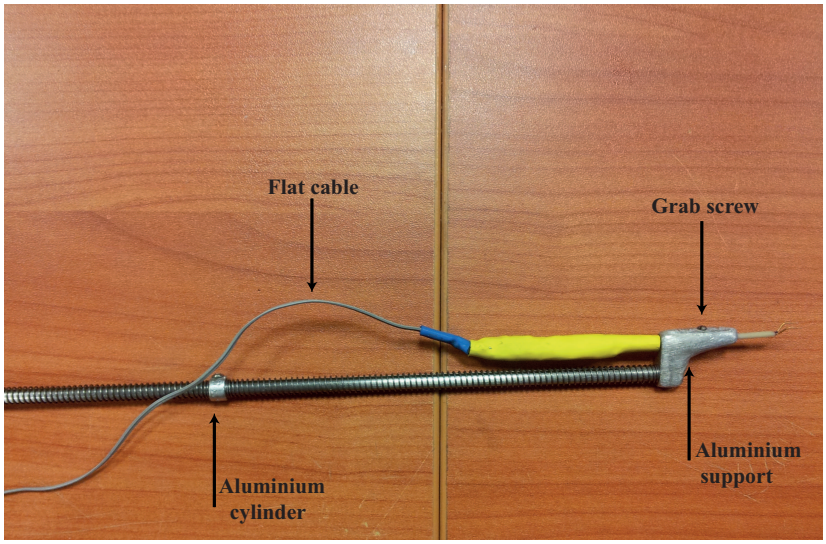

Figure 3.1: *Extensible shaft after the improvements. We can see the cylinder between the springs, the flat cable.*

3.1.5 Press fit bushings and vertical supports

In the original setup, when the transverse beam that controls the probe position moved, the two press fit bushings went out of position because of the friction between their o-rings and the

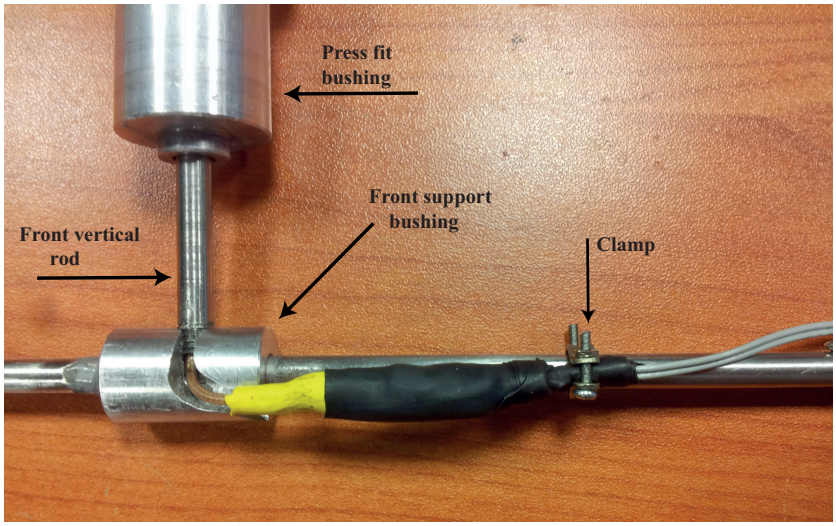

Figure 3.2: *Shaft supports after the improvements. We can see the stable coupling between the new supporting bushing and the new vertical rod, the milled cable rail and the cable clamp.*

vertical rods. We have thus placed two aluminum plates over the press fit bushings and then fixed them to the pipe by means of hose ties. The joint between bushings and pipes were eventually sealed by means of silicone. The support vertical rods of the main shaft slid through the transverse beam during the radial motion making a repeatable positioning impossible to achieve. In order to avoid this sliding, two aluminum clamps were realized to secure the rods to the transverse beam.

3.2 Hot-film probe motion calibration

The changes implemented made necessary to proceed with a new calibration of the probe traversing system in both the axial and radial direction.

3.2.1 Axial positioning calibration

It was decided to put the axial zero position in correspondence with the total compressed springs configuration. In this

way the probe reaches the first moving segment after 18 cm against the 17 cm of the previous set-up: the new set-up allows us to analyze a longer spatial transient than the previous one. On the other hand using 3 springs instead of 2 forces us to pay specific attention to the repeatability of the equipment positioning and thus the effective movements of the probe had to be verified. Looking carefully at the set-up it is quite clear that the biggest issue is related to the elastic response of the set of springs, which acts differently during compression and pushing-back: starting at the axial zero position, with 3 springs totally compressed, and moving the probe forward by using the calibrated wheel, it is not absolutely certain that the springs total displacement is equal to the displacement of the steel that pulls the extensible shaft; starting instead at an elongated springs position and moving the probe backward, supposing that the steel wire does not yield, the springs total displacement corresponds to the one of the steel wire. Hence several forward and backward runs have been performed in order to confirm our theory and establish the correct probe positioning procedure during the experiments. The real position of the probe was measured by means of a caliper. Results are shown in tables 3.2 and 3.3. Mean error and standard deviation between nominal and real position of the probe have been evaluated, as shown in table 3.1.

Table 3.1: *Mean error and standard deviation of the probe axial positioning from the nominal position*

	Mean error [cm]	**Standard deviation [cm]**
Forward run	-0.084	0.0243
Backward run	0.018	0.0139

It can be seen that the mean error made during a backward run of the probe is smaller than the forward run one. Furthermore, it is of the order of the caliper precision and thus we

decided to use a backward run for a repeatable axial positioning.

Table 3.2: *Equipment axial positioning using a forward run*

Nom. pos.[cm]	Run 1	Run 2	Run 3	Run 4	Run 5	Run 6
1	0.91	0.92	0.915	0.905	0.955	0.92
2	1.875	1.88	1.885	1.92	1.915	1.89
3	2.91	2.925	2.905	2.88	2.92	2.885
4	3.89	3.945	3.925	3.91	3.925	3.895
5	4.91	4.91	4.925	4.885	4.93	4.89
6	5.895	5.975	5.96	5.92	5.97	5.915
7	6.89	6.91	6.885	6.92	6.895	6.91
8	7.9	7.91	7.915	7.885	7.92	7.915
9	8.925	8.925	8.925	8.925	8.925	8.935
10	9.915	9.895	9.905	9.915	9.935	9.88
11	10.895	10.925	10.915	10.905	10.915	10.935
12	11.815	11.935	11.855	11.955	11.935	11.895
13	12.89	12.96	12.935	12.91	12.955	12.895
14	13.915	13.96	13.925	13.92	13.905	13.925
15	14.92	14.955	14.915	14.925	14.93	14.915
16	15.915	15.945	15.92	15.895	15.925	15.905
17	16.96	16.94	16.945	16.92	16.915	16.9
18	17.935	17.95	17.935	17.905	17.925	17.955

Table 3.3: *Equipment axial positioning using a backward run*

Nom. pos. [cm]	Run 1	Run 2	Run 3	Run 4	Run 5	Run 6
1	1.035	1.015	1.02	1.0150	1.005	1.035
2	2.05	2	2.03	2.04	2.035	2.025
3	3.005	3.015	3.025	3.015	3	3.01
4	4.02	4.035	4	4.015	4.015	4.045
5	5.025	5.035	5.005	5.01	5	5.035
6	6.015	6.035	6.005	6.005	6.035	6
7	7.025	7.005	7	7.015	7.005	7.035
8	8.025	8.025	7.995	8.025	8.01	8.03
9	9.015	9.035	9.025	9.015	9.025	9
10	10.015	10.035	10.015	10.04	10.02	10.025
11	11.045	11.015	11.035	11	11.015	11.005
12	12.02	12.015	12.015	12.015	12.035	11.995
13	13.015	13.035	12.99	13.025	13.04	13
14	14.05	14.02	13.99	14	14.015	14.02
15	15.015	15	15.025	15.045	15.005	15.01
16	16.02	16.025	16.025	16.03	16	16.015
17	16.995	17.025	17.01	17.005	17.025	17.01
18	18.025	18.01	18.02	18	18.015	18.005

3.2.2 Radial positioning calibration

The radial positioning was analyzed in the same way as the axial one. Therefore we disposed several radial runs from the centerline of the pipe (that corresponds to the radial zero position) to the wall (that corresponds to 24.25 mm) using a stepper motor with 2.5 μm step. The real position of the probe was measured by means of a caliper and results are shown in tables 3.4 and 3.5.

Table 3.4: *Mean error and standard deviation of the probe radial positioning from the nominal position*

	Mean error [mm]	**Standard deviation [mm]**
Radial run	-0.002	0.0483

Table 3.5: *Equipment radial positioning*

Nom. pos.[mm]	Run 1	Run 2	Run 3	Run 4	Run 5	Run 6
1	1.05	1	1.1	0.95	1	0.95
2	2	2.05	2	2.05	2	2
3	3.05	3.05	2.95	3	3	3
4	3.95	4	4	4.05	4.1	4.05
5	5	5.05	5	5.15	5	5.05
6	6	6.05	6.1	6	6	6.15
7	7	7	7.05	6.95	6.9	7
8	7.95	7.95	8	8.05	8	8
9	8.95	9	9	9	9	9.05
10	10	10.05	9.9	10	9.95	10.05
11	11	10.95	10.95	11	10.95	11
12	12.05	11.95	11.85	11.95	12	12
13	13	13	13.05	12.95	12.95	12.95
14	13.95	13.95	14	14.05	14.05	14
15	15	14.95	15	15	14.9	15
16	16	16	16	16	15.95	15.95
17	17.05	17	17	17.1	17.15	17
17	18	18.05	18.05	18.05	18	18.1
19	18.9	18.95	19	19	18.95	18.95
20	20	19.95	19.95	19.95	19.9	20
21	21.05	21	20.95	21	21	21
22	21.95	21.95	22	21.95	22	21.9
23	23.05	23	23	23	22.95	23
24	24	23.95	24	24	24	23.95
24.25	24.25	24.25	24.25	24.25	24.25	24.25

The mean error measured is far smaller than the caliper precision and we can thus infer that errors are due to our imprecision in taking the measure and that the radial positioning is well precise and accurate. This is supported by the fact that we always reached the wall after a total run of 24.25 mm.

3.2.3 Shaft alignment in the horizontal plane

We have also verified the alignment of the shaft to the pipe centerline by checking the distance of the probe center from the pipe walls in the horizontal plane in 3 different axial positions. We measured, by means of a caliper, the distance of the probe from the left wall and the right one and in each of these positions the probe was centered. We can safely say that there is an alignment of the probe in the horizontal plane.

3.3 Assembling procedure

The assembling procedure of the probe support is really critical because a bad positioning of the shaft will affect the measures. We can divide the procedure in several steps:

- All the pieces of the supporting equipment must be clean in order to avoid contamination of the water flow. The springs and the extensible shaft have to be lubricated to help the sliding while a PVC runner has to be inserted in the main shaft rear bushing to prevent damages to the steel cable. A grab screw must be inserted on the top of the aluminum support of the probe in order to avoid a contact between the probe needles and the pipe wall. This will influence the minimum distance from the wall that can be analyzed.

- The main shaft must be placed on the retaining structure and inserted in the pipe so that the supporting bushings match with the pipe holes. The steel pulling cable and the electrical cable must be pulled through those holes.

- The cables must be pushed through the vertical rods and the press fit bushings have to be assembled. The retaining structure can be safely removed from the pipe and place the press fit bushings in the correct position. At this point the

screws between rods and bushings must be adjusted in order to properly align the shaft with the pipe centerline, and the probe radial run in each axial position must be checked. A little torque has to be applied to the main shaft, rotating one of the press fit bushing, because of a little misalignment of the pipe holes and then the alignment of the probe in the horizontal plane must be checked.

- The joint between the press fit bushings and the pipe must be sealed with silicone and each bushing has to be fixed to the pipe by means of an aluminum plate and two hose ties.
- We can eventually close the transverse beam, insert the steel cable in the wheel and proceed with the axial calibration. Two aluminum clamps must be placed over the joint between the transverse beam and the vertical support rods.
- Finally we must check again the axial and the radial motion before closing the pipe .

Chapter 4

Hot-film anemometry

In this chapter hot-film anemometry is described. In section 4.1 a theoretical description of the working principle of the hot-film anemometry is provided with a description of the practical implementation. In section 4.2 the directional sensitivity of the probes is described with particular regard to our case. In section 4.3 the calibration procedure adopted in our case is described in detail.

4.1 Thermal anemometry

4.1.1 Governing equations

Thermal anemometry is an intrusive technique to measure the local velocity in a fluid with good spatial and temporal resolution. Its working principle is based on the heat balance of a small heated sensor immersed in the fluid. Considering a differential element of the probe of length dx and cross-sectional area A, the heat transfer is due to:

- The conduction heat transfer rate that enters into the left end of the element:

$$Conduction\ heat\ in\ = -KA\frac{\partial T_s}{\partial x} \tag{4.1}$$

where K and T_s are the sensor thermal conductivity and temperature respectively.

- The conduction heat transfer rate that goes out from the right end of the element:

$$Conduction\ heat\ out\ = -KA\frac{\partial T_s}{\partial x}\bigg|_{x+dx} \tag{4.2}$$

Using a first order Taylor expansion the conduction heat out results:

$$Conduction\ heat\ out\ \simeq -KA\frac{\partial T_s}{\partial x} - KA\frac{\partial^2 T_s}{\partial^2 x}dx \tag{4.3}$$

assuming a constant cross-sectional area and thermal conductivity along the x coordinate of the sensor.

- The convection heat loss rate from the external surface of the differential element:

$$Convection\ heat\ loss\ rate = -2\pi r h(\mathbf{U})(T_s - T_f)dx \tag{4.4}$$

where T_f is the fluid temperature, r is the sensor diameter and h is the coefficient of convective heat transfer that depends on the fluid velocity $\mathbf{U}$.

- The radiation heat loss rate from the external surface of the differential element:

$$Radiation\ heat\ loss\ rate = 2\pi r\sigma\epsilon(T_s^4 - T_{sur}^4)dx \tag{4.5}$$

where σ is the Stefan-Boltzmann constant, ϵ the emissivity of the sensor and T_{sur} is the surroundings temperature.

- The heat storage rate of the differential element:

$$Heat\ storage\ rate\ = \rho cA\frac{\partial T_s}{\partial t}dx \tag{4.6}$$

where ρ and c are the sensor density and specific heat respectively.

- The heat production rate of the differential element by Joule heating:

$$Joule\ heating\ rate\ = \frac{I_s^2 \rho_r}{A} dx \tag{4.7}$$

where ρ_r is the sensor resistivity and I_s is the intensity of the heating current.

The heat balance is summarized in Figure 4.1

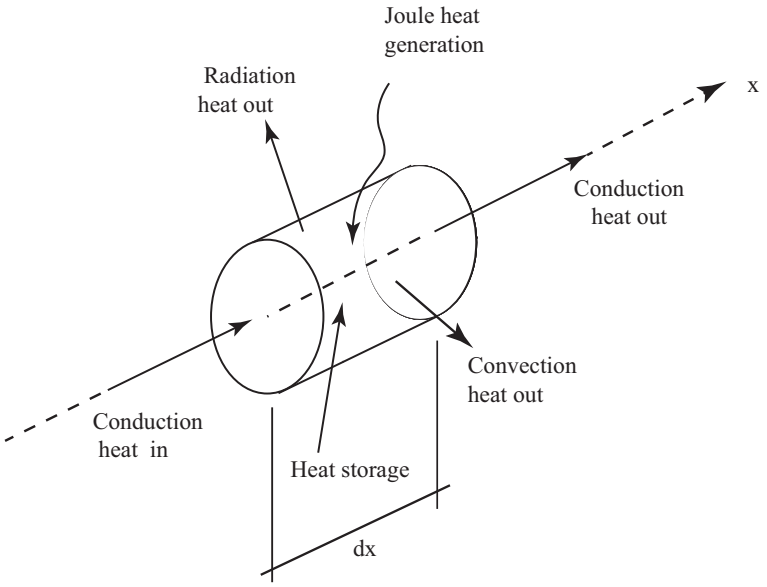

Figure 4.1: *Differential element heat balance*

We obtain thus the following heat balance differential equation for the differential element:

$$\rho c A \frac{\partial T_s}{\partial t} - K A \frac{\partial^2 T_s}{\partial^2 x} - \frac{I_s^2 \rho_r}{A} + 2\pi r \sigma \epsilon (T_s^4 - T_{sur}^4) + 2\pi r h(\mathbf{U})(T_s - T_f) = 0 \tag{4.8}$$

As suggested by Lomas in [25] the radiation heat transfer is negligible and thus:

$$\rho c A \frac{\partial T_s}{\partial t} = K A \frac{\partial^2 T_s}{\partial^2 x} + \frac{I_s^2 \rho_r}{A} + 2\pi r h(\mathbf{U})(T_s - T_f) \tag{4.9}$$

We can further simplify the equation 4.9 by analyzing the temperature profile above the sensor at different length-to-diameter ratios as shown in Figure 4.2.

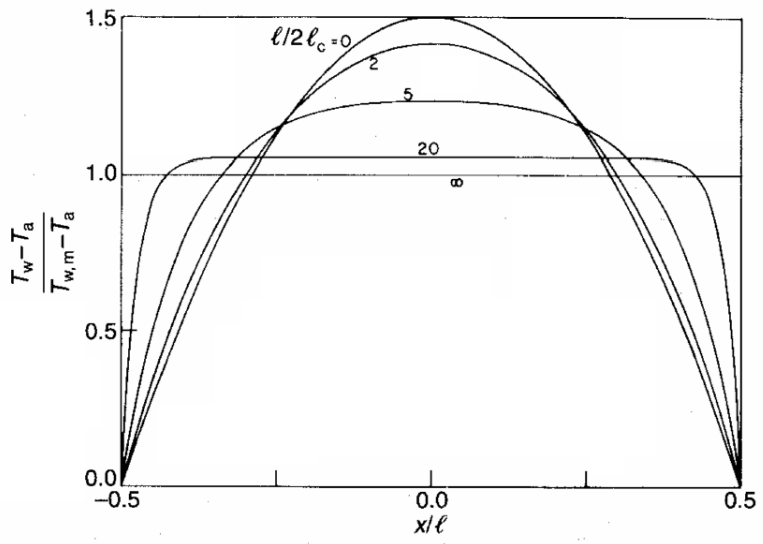

Figure 4.2: *Temperature profile above the sensor at different length to diameter ratio*

The temperature is almost uniform along the sensor axis when the length to diameter ratio reaches values around 20, a normal value for a modern sensor. We can therefore assume a constant temperature profile along the sensor and simplify 4.9 in:

$$\rho c A \frac{\partial T_s}{\partial t} = \frac{I_s^2 \rho_r}{A} + 2\pi r h(\mathbf{U})(T_s - T_f) \tag{4.10}$$

Considering a finite sensor of length l we can integrate along the coordinate x the equation 4.10 and write:

$$m_s c \frac{\partial T_s}{\partial t} = I_s^2 R_s - S h(\mathbf{U})(T_s - T_f) \tag{4.11}$$

where m_s is the sensor mass, R_s its resistivity and S its surface.

The equation 4.11 is the governing equation of the thermal anemometry: under appropriate hypothesis the velocity **U** can be determined by the relation between T_s, T_f, R_s and I in several ways.

4.1.2 Operating modes

Using the results obtained in 4.11 it is possible to develop an intrusive technique for measurements of temperature and velocity fluctuations. A suitable sensor, whose resistance depends on the temperature, can be used to generate a measurable signal. Depending on measurements typology, the electrical signal can be obtained in three different ways:

- Constant-current anemometry (CCA): the current in the wire I_s is kept constant and thus any change in the flow velocity causes a variation in the wire resistance R_s. Since I_s is constant any variation of R_s creates a change in the voltage drop V_s along the filament that can be used as the measurable signal.

- Constant-temperature anemometry (CTA): the resistance of the wire R_s and hence its temperature T_s are kept constant so that any change in the flow velocity causes a variation of the current in the wire I_s. In the same way as the CCA the voltage drop V_s along the filament is used as the measurable signal.

- Constant-voltage anemometry (CVA): the voltage drop along the wire V_s is maintained constant so that any change of the flow velocity causes a variation in the wire resistance R_s. In this case the measurable signal is the change of the current I_s in order to keep V_s constant.

For our measurement the CTA was chosen in order to automatically compensate the thermal inertia of the sensor since T_s is kept constant. In a CTA the governing equation 4.11 simplifies further in:

$$I_s^2 R_s = Sh(\mathbf{U})(T_s - T_f) \tag{4.12}$$

In order to keep the working temperature of the wire constant, an electronic feedback loop is essential, as shown in Figure 4.3 The sensor is placed in one arm of a Wheatstone bridge in order

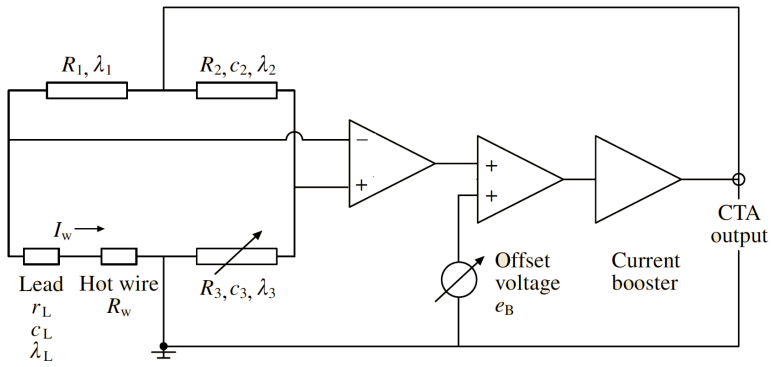

Figure 4.3: *Block diagram of a constant temperature anemometer (CTA) from [10]*

to achieve a larger voltage signal that is further processed by an operational amplifier. Furthermore the bridge ratio R_2/R_1 is about $5 - 20$ so that the current goes mainly in the active arm of the bridge. The resistance R_3 can be adjusted in order to change the overheat ratio of the wire defined as:

$$a_w = \frac{T_s - T_f}{T_f} \tag{4.13}$$

It is quite clear that increasing the overheat ratio leads to a rise of the convection heat loss and thus, from 4.12, to a rise of the measurement signal V_s. The overheat ratio in water application is limited to 0.1 due to the formation of vapor bubbles as consequence of water boiling.

4.1.3 Sensors

The sensors for the thermal anemometry have to be chosen wisely: the spatial resolution and the frequency response of the sensor depends on its size; the mechanical strength must be high enough to sustain the measuring flow; the material resistivity influences sensor sensitivity. Close to the ends of the sensor are located two stabs, with a low electrical resistance in order not to be involved in the response of the probe, that connect the sensor to two supporting prongs. The best suitable solution for the thermal anemometry are undoubtedly wires or films 4.4:

- wire sensors are $0.5 \div 2\ mm$ long with a diameter of $0.5 \div 5\ \mu m$ and thus the length-to-diameter ratio is higher than 400. The most common wire materials are platinum and tungsten.
- film sensors are $0.5 \div 2\ mm$ long with a thickness of $0.1\ \mu m$ and are deposited on a cylinder of quartz $25 \div 50\ \mu m$ and thus the length-to-diameter ratio is lower than 50 but the hypothesis of constant temperature along the film is still acceptable. The most common wire materials are platinum and nickel.

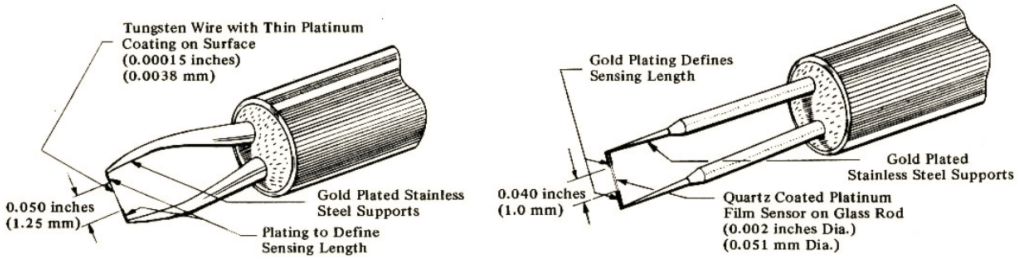

Figure 4.4: *A comparison between a typical hot-wire and a typical hot-film*

The hot-wire provides a better frequency response and spatial resolution than a hot-film but it is less resistant and not suitable for water flow measurements, where contaminant particles could

destroy the sensor. For those reasons we decided to use a hot-film sensor with boundary layer prongs to measure close to a solid wall without disturbance from the probe body as shown in Figure 4.6

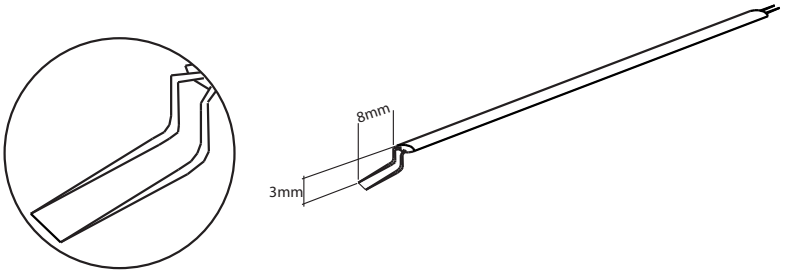

Figure 4.5: *Dantec 55R15 boundary-layer hot-film probe*

4.2 Directional sensitivity

4.2.1 Effective cooling velocity

In order to achieve a correct calibration of the probe, its directional sensitivity has to be taken into account. As shown in Figure 4.6, three reference directions and two angles can be defined in order to describe the orientation of the velocity vector **U** with respect to the wire axis:

- the tangential direction, parallel to the wire axis.
- the normal direction, laying in the plane of the wire and the prongs and normal to the wire axis.
- the bi-normal direction, perpendicular to the tangential and normal ones.
- the angle α between the normal-bi-normal plane and the velocity vector **U**.
- the angle β between the normal-tangent plane and the velocity vector **U**.

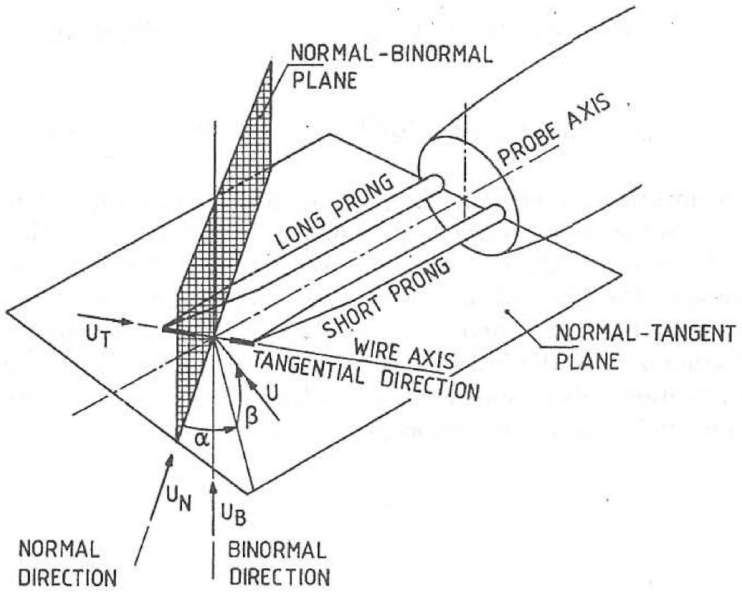

Figure 4.6: *Hot-film probe sensitivity from [11]*

An effective cooling velocity can thus be defined as a function of the magnitude U of the velocity vector and of the angles α and β:

$$U_{eff} = F(U,\alpha,\beta) \tag{4.14}$$

As described by Jorgensen in [26], the effective cooling velocity depends strongly on α and weakly on β. This is due to the fact that the normal and bi-normal flows can be considered to be at constant temperature T_f, while the tangential flow is heated all along the wire reducing its cooling efficiency. Furthermore, the solid blockage of the prongs makes the tangential flow less effective than the other two. The effective velocity can thus be expressed as:

$$U_{eff}^2 = U_N^2 + k_T^2 U_T^2 + k_B^2 U_B^2 \tag{4.15}$$

where k_B is usually 1.1, to take into account the flow acceleration in the binormal direction due to the prongs configuration, and k_T is usually 0.1.

4.2.2 Hot-film sensitivity in a pipe

Considering the axi-symmetric nature of the pipe flow, we can take into account the steady Reynolds-averaged Navier-Stokes equations (RANS) for incompressible flows written in cylindrical coordinates. The streamwise, radial and azimuthal coordinates are denoted by x, r and θ while $\langle U\rangle$, $\langle V\rangle$, $\langle W\rangle$ and u, v, w represent the mean and fluctuation values for velocity and $\langle P\rangle$ represents the mean pressure. The Reynolds stresses are denoted by $\langle u^2\rangle$, $\langle v^2\rangle$, $\langle w^2\rangle$, $\langle uv\rangle$, $\langle uw\rangle$ and $\langle wv\rangle$. The pipe flow can be assumed invariant to rotation around and translation along the x-axis so that the statistics depend exclusively on r and furthermore the mean azimuthal velocity can be assumed negligible. For those reasons the RANS equations for a steady turbulent pipe flow translate into:

$$\begin{cases} \dfrac{1}{r}\dfrac{\partial r\langle V\rangle}{\partial r} = 0 \\ \langle V\rangle\dfrac{\partial\langle U\rangle}{\partial r} = -\dfrac{1}{\rho}\dfrac{\partial\langle P\rangle}{\partial x} + \dfrac{1}{r}\left(r\nu\dfrac{\partial\langle U\rangle}{\partial r} - \langle uv\rangle\right) \\ \langle V\rangle\dfrac{\partial\langle V\rangle}{\partial r} = -\dfrac{1}{\rho}\dfrac{\partial\langle P\rangle}{\partial r} + \dfrac{1}{r}\left(r\nu\dfrac{\partial\langle V\rangle}{\partial r} - \langle v^2\rangle\right) - \nu\dfrac{\langle V\rangle}{r^2} + \dfrac{\langle w^2\rangle}{r} \\ \dfrac{\partial\langle vw\rangle}{\partial r} + 2\dfrac{\langle vw\rangle}{r} = 0 \end{cases} \tag{4.16}$$

From the averaged continuity equation we obtain:

$$\langle V\rangle r = cost \tag{4.17}$$

But since V is null at the boundary, V is therefore null everywhere. In regards to the hot wire in our configuration we can thus identify an incident velocity U_I composed by the mean velocity $\langle U\rangle$ and the fluctuation velocities u, v and w as shown in Figure 4.7.

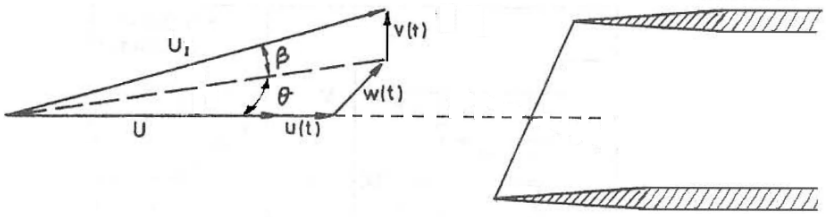

Figure 4.7: *Hot-film incident velocity in a pipe flow*

As k_T is in the order of 0.1, v is smaller than u and α is null we can hypotesize in first approximation that the anemometer voltage output is proportional to $U_{eff} = \langle U \rangle + u$. In our setup this hypothesis holds only when the rotating segments do not move and thus can be applied only during the calibration procedure. The swirl component of the turbulent flow has to be taken into account once the pipe slabs are set into motion since the wall velocity is comparable to the flow streamwise velocity and thus a correction of the measured values is fundamental.

4.3 Calibration

4.3.1 Calibration curve

In order to find a direct relation between electrical quantities and flow velocity we can introduce a dimensionless heat flow, the Nusselt number, defined as:

$$Nu = \frac{hl}{k} \tag{4.18}$$

Thus the equation 4.12 can be rewritten as:

$$I_s^2 R_s = \frac{S}{l} KNu(T_s - T_f) = \pi DKNu(T_s - T_f) \tag{4.19}$$

From the dimensionless analysis the Nusselt number is a function of:

$$Nu = Nu\left(M, Re, Gr, Pr, \gamma, \frac{T_s - T_f}{T_f}\right) \tag{4.20}$$

where M is the Mach number, Re is the Reynolds number, Gr is the Grashov number, Pr is the Prandtl number and γ is the ratio of the heat capacities at constant pressure and constant volume. Since we are dealing with a subsonic flow we can neglect the effect of M and γ and assume Pr fixed. If we further hypothesize that forced convection is much larger than natural one, the Nusselt number reduces to:

$$Nu = Nu\left(Re, \frac{T_s - T_f}{T_f}\right) \tag{4.21}$$

Thus the heat-transfer law for forced convection can be written:

$$Nu = (A_{Nu} + B_{Nu} Re^n)\left(\frac{T_s + T_f}{2}\right)^m \tag{4.22}$$

where A_{Nu},B_{Nu},m and n are constants. Introducing equation 4.22 in 4.19 we obtain the King's law:

$$I_s^2 R_s = A + B U_{eff}^n \tag{4.23}$$

where A and B depend on the wire geometry and fluid temperature and n is generally 0.5 for low Reynolds numbers. Since we are dealing with a low Reynolds number and are interested in the analysis of the near wall statistic, where the flow velocity is very low, the natural convection cannot be neglected and thus the King's law doesn't fulfil our requirements. In order to achieve a good fit between experimental data and calibration curve, maintaining a good stability of the curve, we chose a 3

constants rational fit of the type:

$$U = \frac{A + BV_s}{C + V_s} \tag{4.24}$$

4.3.2 Fluid temperature drift

Since the temperature of the fluid T_f is different day to day and also during a single test because a little part of the mechanical energy of the centrifugal pump is transformed in thermal energy, the calibration procedure has to take into account this effect. From equation 4.19 we can notice that the voltage output signal of the wire decreases as the fluid temperature increases and this effect is shown in Figure 4.8. We have thus decided

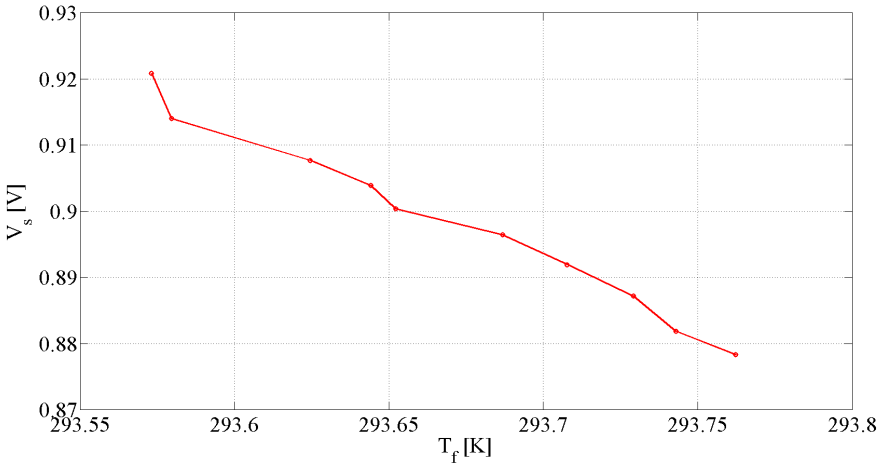

Figure 4.8: *Anemometer voltage output as a function of the fluid temperature*

to introduce as calibration variable in 4.25 the output signal corrected for the temperature drift of the flow as suggested by Lemonis and Dracos in [27]:

$$V_s^{corr} = \frac{V_s^{meas}}{G} \left(\frac{T_s - T_{f0}}{T_s - T_f} \right)^{0.5} \tag{4.25}$$

where T_{f0} is the temperature of the fluid during the calibration and G is the anemometer gain.

4.3.3 Calibration velocity profiles

In order to cover the velocity range of our interest it is essential to acquire the voltage signal of both a laminar and a turbulent flow. Considering a steady fully developed laminar pipe flow, using the axisimmetry of the flow and its invariance along the pipe axis, we can obtain the Hagen-Poiseuille solution for the velocity profile:

$$U(r) = \frac{2Q}{\pi R^4}(R^2 - r^2) \tag{4.26}$$

where Q is the volumetric flow rate through the cross-section of the pipe and R the pipe radius. The velocity profile for a laminar flow at $Re = 1400$ is shown in Figure 4.9. For the fully

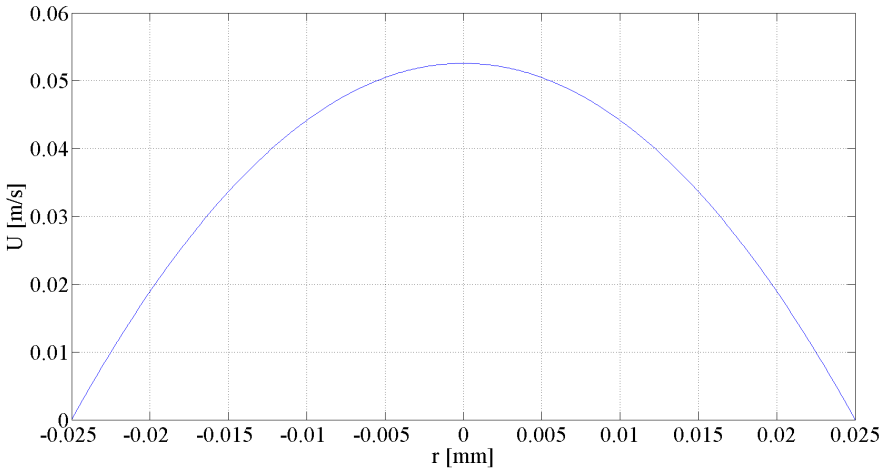

Figure 4.9: *Poiseuille velocity profile for a laminar flow at* $Re = 1400$

developed turbulent pipe flow we use instead the data from den Toonder and Nieuwstadt [28] at $Re = 4900$, as shown in Figure 4.10.

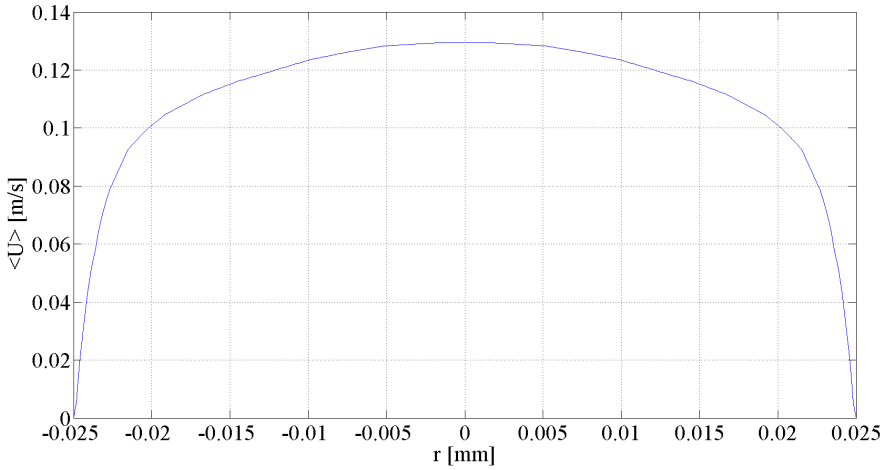

Figure 4.10: *Velocity profile for a turbulent flow at* $Re = 4900$

We have thus acquired eight points in the turbulent flow and four in the laminar one at different radii and the calibration curve obtained is shown in Figure 4.11:

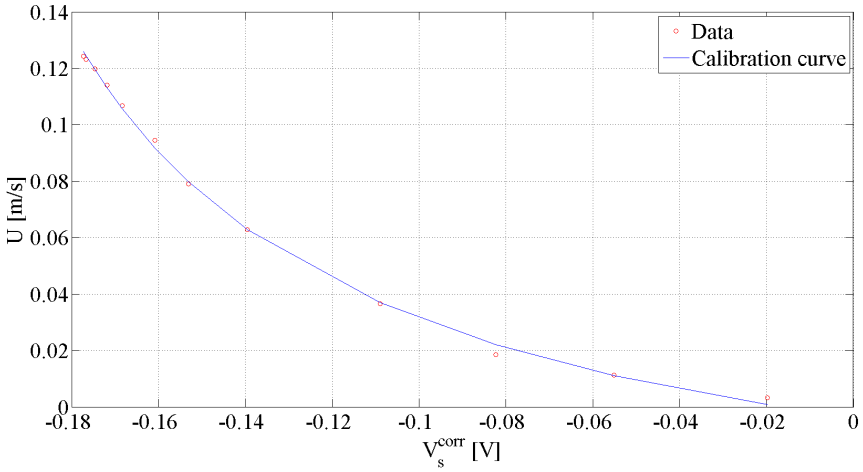

Figure 4.11: *Calibration curve for the velocity* U *as a function of the corrected voltage signal* V_s^{corr}

In order to verify our calibration we have acquired 7 velocity profiles with a total temperature drift from curve 1 to curve 7 of $0.9K$. The results are shown in Figure 4.12. The maximum error is 0.0031 m/s with a standard deviation of 0.0012 m/s, with a

local percentage error lower than 5.24%. In order to improve the accuracy of our measures, we decided to carry out the calibration procedure each morning before every experimental campaign.

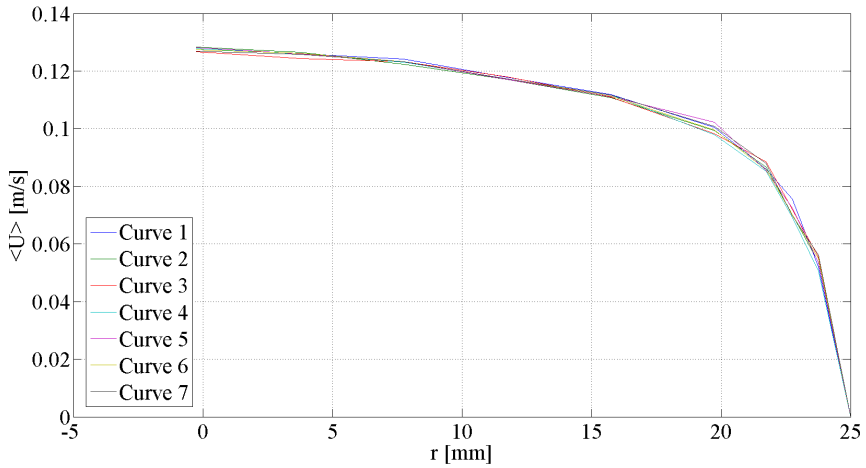

Figure 4.12: *A comparison between 7 velocity profiles acquired at different fluid temperature T_f. The total drift is about $0.9K$*

4.3.4 Flow centerline investigation

As described in chapter 3 the extensible shaft is not always in the centerline of the pipe and thus we have to verify the real position at the start of the radial run in each axial positions in order to obtain accurate measurements. We have thus compared the velocity profile obtained with a calibration in the total compressed springs configuration, where the true position of the probe is known, with the profiles acquired at different axial position: in this way we were able to evaluate the displacement between the pipe centerline and the probe at the start of the radial run. In Figure 4.13 is quite clear that the head of the probe is not aligned with the flow centerline at the start of the radial run.

Using a parabolic interpolation for the measured velocity profile it is possible to evaluate the displacement between the center-

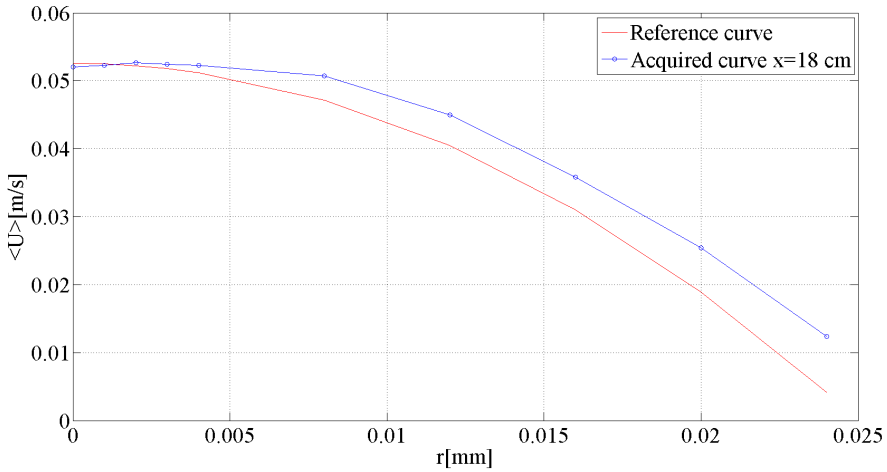

Figure 4.13: *A comparison between the reference profile and the velocity profile acquired at* $x = 18\ cm$

line and the parabola maximum. The displacement behaviour through the axial run is shown in Figure 4.14. The displacement found was then used to correctly place the probe during our experiment (a positive displacement corresponds to a probe position below the pipe centerline).

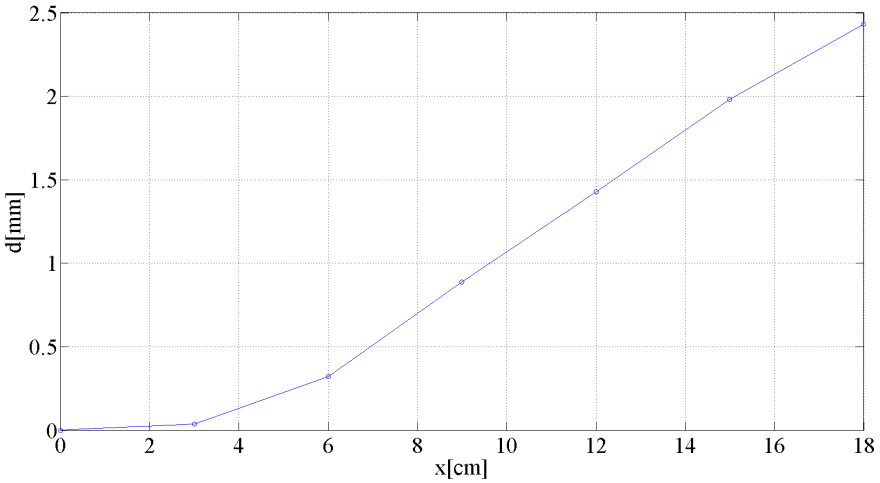

Figure 4.14: *Displacement between the centerline and probe position at the start of the radial run at different axial position*

Chapter 5

Results

In this chapter the results obtained are described. In section 5.1 the determination of the Jorgensen tangential coefficient is illustrated with a discussion of the influence of the generalized Stokes layer. In section 5.2 the drag reduction results are illustrated with a comparison with other experimental and numerical data, while in section 5.3 the spatial transient is analyzed. In section 5.4 the turbulent statistics are illustrated at different frequencies and wavelengths of the travelling wave.

5.1 K_T determination

The influence of the azimuthal component of the flow velocity must be taken into account once the travelling wave is generated because its magnitude is comparable with that of the streamwise component one. We can thus introduce the laminar generalized Stokes layer to describe the spanwise flow.

5.1.1 Generalized Stokes layer

As described by Quadrio and Ricco in [29], considering a laminar channel flow subjected to a travelling wave wall oscillation described by equation 1.6, an analytical solution for the spanwise velocity induced by the wave can be provided under reasonable

hypothesis. The generalized Stokes layer (GSL) is an extention of the temporal Stokes layer (TSL), which is an unsteady boundary layer that develops with a wall motion described in 1.1 (second Stokes problem), and of the spatial Stokes layer (SSL), which is a steady boundary layer that develops when the wall moves according to 1.1. Under the hypothesis that the layer thickness is much smaller than the distance between the channel walls the spanwise velocity profile can be described in terms of Airy function using the reference system shown in Figure 1.16:

$$W(x,y,t) = A\Re\left\{Ce^{i(k_x x-\omega t)}Ai\left[e^{\pi i/6}\left(\frac{k_x\tau}{\nu}\right)^{1/3}\left(y-\frac{\omega}{k_x\tau}-\frac{ik_x\nu}{\tau}\right)\right]\right\} \tag{5.1}$$

where $\Re$ denotes the real part, k_x and ω are the travelling wave parameters, ν is the flow viscosity and τ is the streamwise velocity component near-wall slope. C is a constant defined as:

$$C = \left\{Ai\left[ie^{\pi i/3}\left(\frac{k_x\tau}{\nu}\right)^{1/3}\left(\omega/k_x + ik_x\nu\right)/\tau\right]\right\}^{-1} \tag{5.2}$$

Furthermore in the channel flow the streamwise flow is not affected by the spanwise flow and hence the two components can be separately investigated. However this result is only approximately valid in the pipe flow, where the streamwise velocity is slightly influenced by the generalized Stokes layer. Further details can be found in [29].

5.1.2 Travelling wave influence

In order to use the results obtained by Quadrio and Ricco in [29] at first we analyzed the laminar flow in the unperturbed case and the calibration curve obtained is shown in Figure 5.1.

The temperature drift was null and hence we decided to operate without temperature correction. The mean streamwise velocity at $r = 24.25\ mm$ is $\langle U \rangle (24.25\ mm) = 0.031\ m/s$. We then analyzed the velocity detected by the hot-wire in the

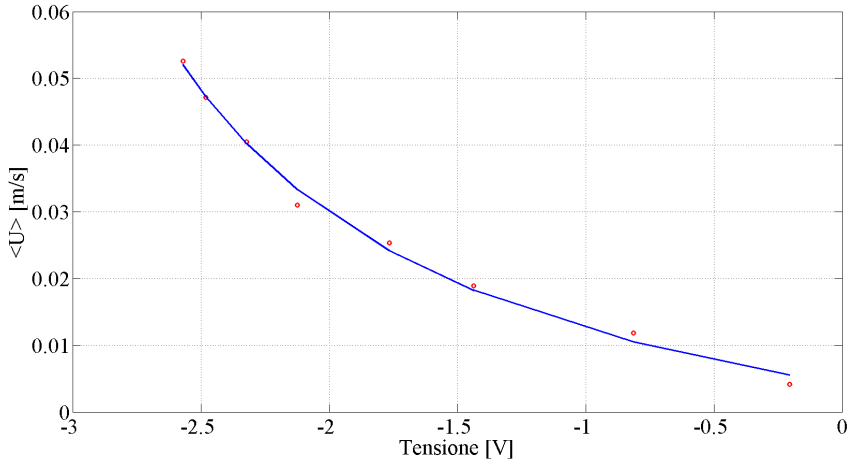

Figure 5.1: *Calibration curve in a laminar flow at* $Re = 1400$

travelling wave case with $A = 0.0796\ m/s$, $k_x = 28.65\ 1/m$ and $\omega = 0.44\ rad/s$. The temporal behaviour of the velocity seen by the hot-wire at $r = 24.25\ mm$ (distance from the wall $y = 0.75\ mm$) is shown in Figure 5.2, in which $U^{tot} = U + \widetilde{W}$ is the total velocity given by the hot-wire and $\widetilde{W}$ is a part of the spanwise velocity that influences the hot-wire measure. Considering that the maximum difference between the travelling wave signal and the reference one is $0.009\ m/s$ and that from equation 5.1 $W_{max}(24.25\ mm) = 0.0635\ m/s$, the influence of the spanwise velocity W is limited. Even though the frequency of the travelling wave is $f = 0.07\ Hz$, the hot-wires signal shows a doubled frequency: this is due to the fact that the wire is insensitive to the direction of the azimuthal velocity w and thus the signal is rettified. The differences between the peaks of the signals are related to small errors in the wave discretization because of different rotations between the clockwise

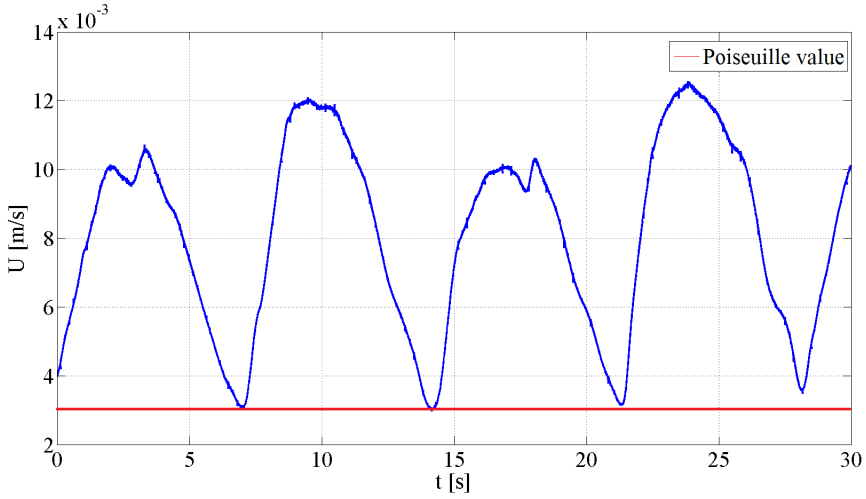

Figure 5.2: *Temporal behaviour of the velocity acquired at $r = 24.25\ mm$ (distance from the wall $y = 0.75\ mm$). Red line represents the Poiseuille solution for the streamwise velocity. This test is performed with W intentionally much larger than U in order to quantify the sensitivity of the hot film along the sensor axis.*

and counterclockwise phase and not to a misalignment of the hot film: a misalignment would modify the whole signal but the two wave semiperiods differ only in the peak region. The different rotations could be explained by different frictions in the two phases. We can notice that the minimum velocity, registered during the reversal phases where $W = 0$ and hence $U^{tot} = U$, is about $U^{tot}_{min} = 0.003\ m/s$, a value similar to the unperturbed case: the unconnection between the streamwise and spanwise components shown by Quadrio and Ricco in [29] is thus verified and the result can be used in order to evaluate the Jorgensen tangential coefficient K_T. Considering the pipe laminar flow, in which $V = 0$, equation 4.15 translates into:

$$U^2_{eff} = U^2_N + k^2_T U^2_T \tag{5.3}$$

In our case we can thus write:

$$U^{tot\ 2}_{max} = U^2 + k^2_T W^2_{max} \tag{5.4}$$

where W_{max} is the spanwise velocity in the GSL. We obtain:

$$k_T = \frac{1}{W_{max}} \sqrt{U_{max}^{tot\ 2} - \langle U \rangle^2} \tag{5.5}$$

Considering the equation at $r = 24.25mm$, where the maximum total velocity is $U_{max}^{tot} = 0.0143m/s$ and $W_{max} = 0.0635\ m/s$, from equation 5.5:

$$k_T \simeq 0.22 \tag{5.6}$$

Even if the value found is larger from those suggested by Jorgensen in [26], we can infer from 4.15 that that only the 4.82% of the square modulus of W influences the square modulus of the total velocity U^{tot}. In the turbulent case, where the thickness of the GSL is smaller and $\langle U \rangle$ is larger near the wall, the error committed is not significant.

5.2 Drag reduction

The experimental campaign was carried out at a fixed value of $Re = 4900$, in order to obtain a fully developed turbulent flow, and of the wall oscillation amplitude $A = 0.079\ m/s$. We investigated the range of frequency $f = -1.5 \div 1.5\ Hz$ for two different wave numbers: $k_{3s} = 57.33\ 1/m$ and $k_{6s} = 28.66\ 1/m$ that correspond to 3 and 6 independent segments respectively. For each wavelength the range of frequency is discretized by means of 28 points; each measurement points consists of an acquisition of 120 s at a frequency of 20 kHz, with a settling time of 40 s before each acquisition in order to achieve a fully developed wave in the active section. The parameters employed are summarized in the table 5.1.

Scaling by the friction velocity $u_\tau \simeq 0.0066\ m/s$ and the viscous length $l_\nu \simeq 0.15\ mm$ of the reference flow we obtain a $Re_\tau \simeq 179$ and $A^+ = 12$, $k_{3s}^+ = 0.008$ and $k_{6s}^+ = 0.004$. In order to evaluate the influence of the wall oscillation amplitude the

Table 5.1: *Experimental parameters of the drag reduction campaign*

Re	**A [m/s]**	**Fr.range[Hz]**	**Sampl.rate[kHz]**	**Sampl.period[s]**
4900	0.079	$-1.5 \div 1.5$	20	120

value of A^+ has been chosen slightly lower than the value of the drag reduction campaign in [8]. The wave parameters employed are summarized in the table 5.2.

Table 5.2: *Experimental parameters in terms of friction*

Re_τ	A^+	u_τ $[m/s]$	l_τ $[mm]$	k_{3s^+}	k_{6s^+}	ω^+
179	12	0.0066	0.15	0.008	0.004	$0.2 \div 0.2$

The pressure drop along the active section was measured and the friction factor is evaluated through:

$$f = \frac{2\Delta p}{\rho U_b^2 L/D} \tag{5.7}$$

The measured friction factor of the reference flow is $f_0 = 0.0405$, a value slightly higher than the value $f_0 = 0.0387$ estimated by using Colebrook formula:

$$\frac{1}{\sqrt{f}} = -2log\left(\frac{\epsilon/D}{3.71} + \frac{2.51}{Re\sqrt{f}}\right) \tag{5.8}$$

where $\epsilon = 50\ \mu m$ is the step between segments. The results obtained are shown in Figure 5.3, where the drag reduction rate R, evaluated according to equation 1.2, is plotted versus ω^+, for $k_{3s}^+ = 0.008$ (circles) and $k_{6s}^+ = 0.004$ (squares). The error bars have been evaluated as described in B

The maximum drag reduction rate observed is $R \simeq 0.35$ and in both cases the larger drag reduction region is achieved for slow forward-travelling waves with a maximum for $c^+ \simeq 3.24$, a value slightly smaller than $c^+ \simeq 3.5$ of the DNS plane channel flow in [7] where $A^+ = 12$ and $Re_\tau = 200$. In the experimental

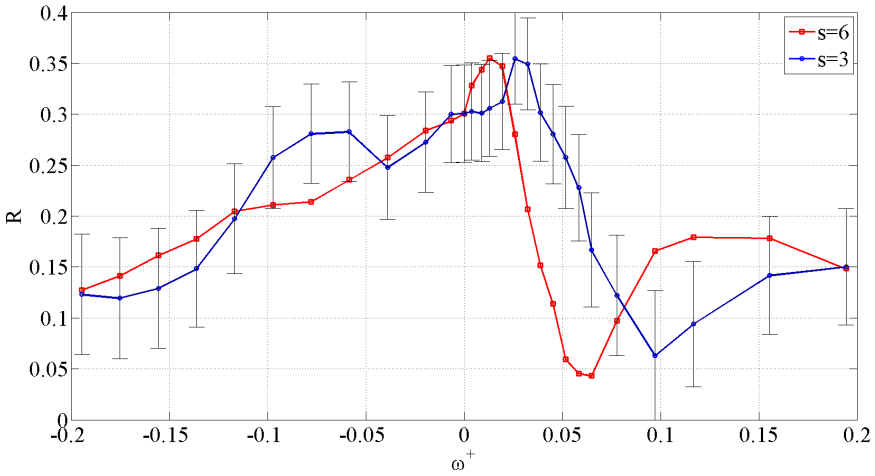

Figure 5.3: *Drag reduction rate as a function of the oscillation frequency for s=3(circle) and s=6(square).* $k_{3s}^{+} = 0.008$ *(circles) and* $k_{6s}^{+} = 0.004$ *(squares).*

campaign the drag increase region is not observed but a large drop in drag reduction is achieved for faster forward-travelling wave with $c^{+} \simeq 12.15$ and $c^{+} \simeq 14.5$ for $k_{3s}^{+} = 0.008$ and $k_{6s}^{+} = 0.004$ respectively, values larger than $c^{+} \simeq 11$ expected from the DNS plane channel flow.

As described in chapter 1 the main dissimilarities between experimental data and DNS data in [7] are related to the effect of a discrete spatial waveform. This issue can be solved comparing the experimental data with the numerical data by Biggi in [30] that are carried out in a turbulent pipe flow with a discrete spatial waveform with $A^{+} = 14.3$ and $Re_{tau} = 169$. As we can notice in Figure 5.4 the qualitative behaviour of the drag reduction rate as a function of ω^{+} is well described by the experimental data when the wave is discretized with 3 segments. Also there is a good agreement in the region of the large drop in drag reduction, with no evidence of drag increase. It should also be noted that at a quantitative level there is a large gap between the numerical and the experimental data. The effects of discretization in the 6 segments case are much smaller than

that of the 3 segments case and the curves show a smooth trend. Again the experimental data at $k_{6s}^{+} = 0.004$ do not show the drag increase expected, even if the drop in drag reduction is higher than that achieved at $k_{3s}^{+} = 0.008$.

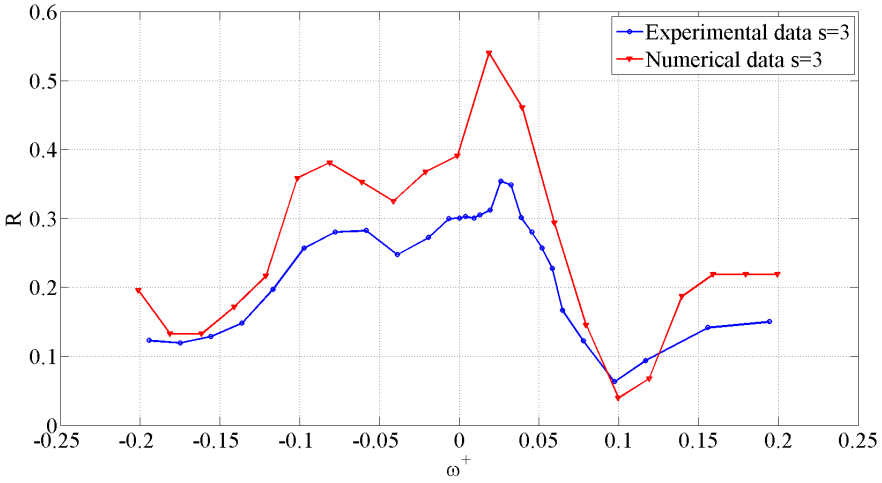

Figure 5.4: *Comparison between experimental and numerical data of drag reduction rate as a function of the oscillation frequency for* $k_{3s}^{+} = 0.008$. *The numerical data (triangles) are carried out at* $A^{+} = 14.3$ *and* $Re_{\tau} \simeq 169$, *while the experimental data at* $A^{+} = 12$ *and* $Re_{\tau} \simeq 179$

In order to explain the discrepancies between numerical and experimental data we have to address our attention to several sources of errors:

- the different values of A^{+} adopted.
- the influence of the spatial transient in the experimental data.
- the differences in wave discretization between numerical and experimental campaign.

Figure 5.5 shows that the drag reduction rate monotonically increases with A^{+} at fixed ω^{+}, but the difference between the numerical $A^{+} = 14.3$ and the experimental $A^{+} = 12$ is such that only a fraction of the deficit in drag reduction can be explained.

The residual gap is also due to the presence of a spatial transient

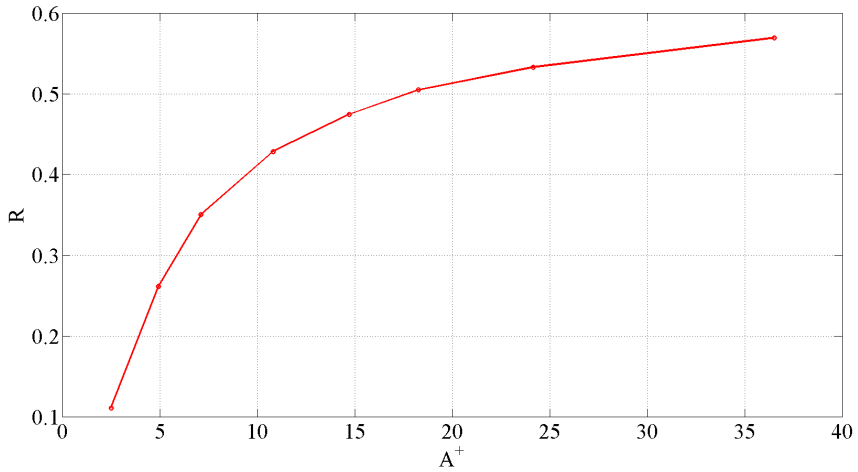

Figure 5.5: *Drag reduction rate versus* A^+ *at fixed* $\omega = 0.03$ *and* $k = 0.628$ *from DNS data*

at the inlet of the active section of the pipe: the regulated flow is fully developed only at a distance $x^+ \simeq 2000 - 5000$ [7] from the inlet and thus the magnitude of the drag reduction is lower than that estimated by the DNS. Furthermore, the mechanical system is obviously subject to mechanical friction and a perfect discretization of the wave, such as those adopted in the direct numerical simulation, is not an easy task. We can also compare the experimental data at $A^+ = 12$ with the experimental data at $A^+ = 13.8$ from [8]. Figure 5.6 and 5.7 shows different drag reduction magnitudes mainly due to the different amplitude of the waves. However the discrepancies at higher frequency values (both positive and negative) are slightly larger because of the increase of the mechanical friction due to wear of the facility. It has to be noted that the differences in the drag reduction peaks between the two campaigns are related to mechanical wave discretization issues at low frequencies.

In order to evaluate the influence of the spatial transient on the drag reduction values measured the friction velocity u_τ was

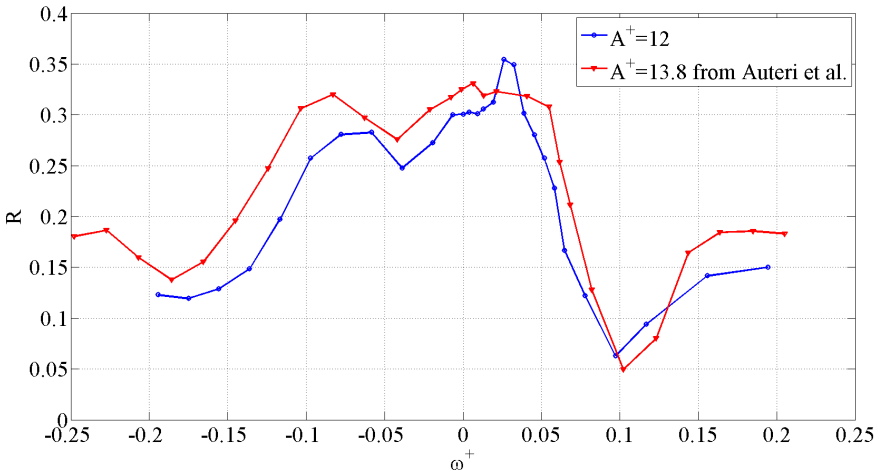

Figure 5.6: *Drag reduction rate as a function of the oscillation frequency for* $k_{3s}^{+} = 0.008$ *at* $A^{+} = 12$*(circles) and* $A^{+} = 13.8$*(triangles).*

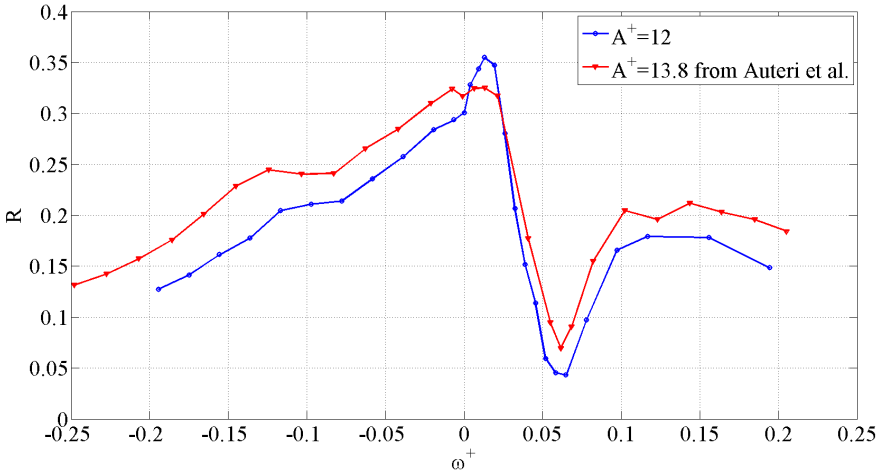

Figure 5.7: *Drag reduction rate as a function of the oscillation frequency for* $k_{6s}^{+} = 0.004$ *at* $A^{+} = 12$*(circles) and* $A^{+} = 13.8$*(triangles).*

estimated by means of the mean velocity gradient at the wall for several frequencies of the travelling wave as suggested by Ricco and Wu in [31]:

$$u_\tau = \sqrt{\frac{\tau_w}{\rho}} = \sqrt{\nu \frac{\partial \langle U \rangle}{\partial y}} \tag{5.9}$$

where τ_w is the local streamwise wall-shear stress and y is the distance from the wall. The mean velocity gradient at the wall has been discretized by:

$$\frac{\partial \langle U \rangle}{\partial y} \simeq \frac{\langle U \rangle (r = 24.25\ mm)}{y(r = 24.25\ mm)} \tag{5.10}$$

where y(r=24.25 mm) $= 0.75\ mm$ and thus $y^+ = 5$. As described by Ricco and Wu in [31], the error in the evaluation of the slope at $y^+ = 5$ is lower than 4%. It is therefore possible to evaluate the friction coefficient C_f:

$$C_f = 2\frac{u_\tau^2}{U_b^2} \tag{5.11}$$

where U_b is the bulk velocity of the flow. The drag reduction rate has been estimated according to 1.2 and the results for $k_{3s}^+ = 0.008$ (circles) and $k_{6s}^+ = 0.004$ are shown in Figure 5.8.

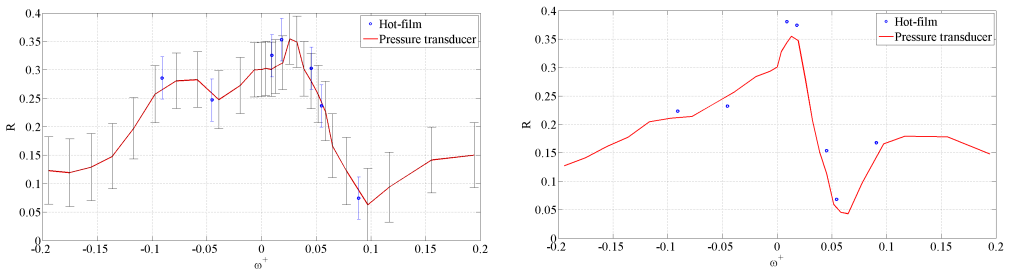

(a) **(b)**

Figure 5.8: *Comparison between drag reduction rate measured by means of pressure transducer (line) and hot-film (circle). $k_{3s}^+ = 0.008$ (a) and $k_{6s}^+ = 0.004$ (b). The error bars in (b) are of the same order of those in (a) and are omitted in order to make the figure readable.*

In both cases and for several frequencies the drag reduction rate measured by means of a hot-film at the outlet of the active section is slightly higher than the value obtained evaluating the pressure drop along the section with a maximum value of $R = 0.38$. The error bars of Figure 5.8 can explain the few

points in which this behaviour is not observed. This result is in line with the presence of a spatial transient at the beginning of the active section and explains the divergence observed between experimental measurements and direct numerical simulations.

5.3 Spatial transient

Hot-film measurements were also carried out to investigate the spatial transient of the drag reduction along the streamwise direction of the regulated flow downstream the active section of the pipe. We decided to discretize the wall forcing by means of 6 segments in order to develop a more homogeneous test field. The campaign was carried out at the same values of Re and A of the drag reduction experiments and the wall oscillation frequency was kept fixed at $f = 0.07\ Hz$, that corresponds to $\omega^+ \simeq 0.01$, a value near the maximum drag reduction. Measurements along the axial direction were conducted at 7 equispaced axial positions: the first and the last position are located at $x = 0\ cm$ and $x = 18\ cm$ downstream the active section respectively. For each axial position the radial run is discretized by means of 16 points; each measurement point consists of an acquisition of 150 s, the highest possible sampling interval safely available in our setup, at a frequency of 20 kHz, with a lower settling time of 20 s because in this case the frequency of the wave was kept fixed. The parameters employed are summarized in the table 5.3.

Table 5.3: *Experimental parameters of the spatial transient campaign*

Re_{tau}	A^+	ω^+	k^+	**Sampl.rate[kHz]**	**Sampl.period[s]**
179	12	0.09	0.004	20	120

In Figure 5.9 the mean velocity profile at $x = 12\ cm$ is compared to the velocity profile of the reference flow. The near wall slope of the mean velocity $\langle U \rangle$ increases as the distance from the

active section increases as shown in 5.10. Each profile shows a lower velocity in the near wall region, with a moderate increase at the centerline. This general trend is well shown in Figures 5.11 and 5.12, obtained after an interpolation of the measured values. The mean velocity profiles have been integrated among the cross-section in order to evaluate the volumetric flow rate and thus the accuracy of the measurements, and the maximum error is about 2.5%.

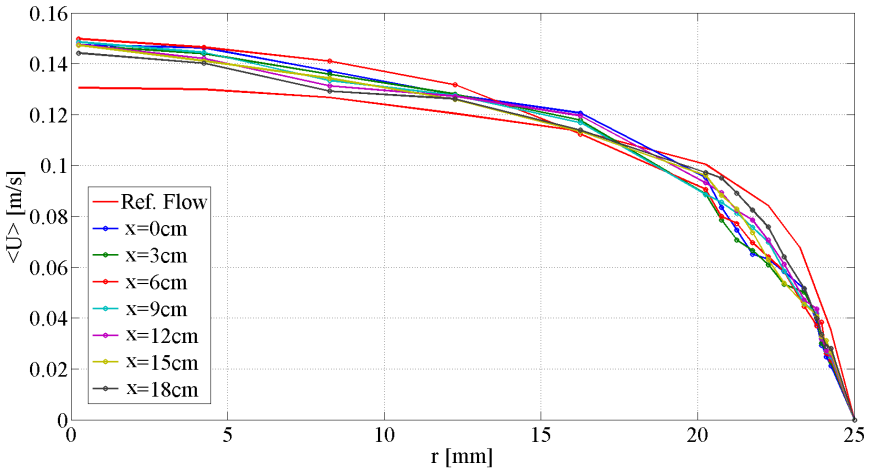

Figure 5.9: *Comparison between mean velocity profile at different axial position at* $A^+ = 12$ *and* $Re_\tau \simeq 179$ *for* $k_{6s}^+ = 0.004$. *The reference flow is unmarked.*

The drag reduction rate along the transient was estimated by means of the mean velocity profile slope and the results are shown in Figure 5.13.

The rate at the outlet of the active section is $R \simeq 0.38$ and slowly decreases to $R \simeq 0.19$ at a distance $x^+ = 1250$ and thus we can infer that the spatial transient should extend for $2000 - 2500$ viscous units.

The component $\langle u^2 \rangle$ of the Reynolds stress tensor and the root mean square value of the streamwise velocity u_{rms} were analyzed in all the spatial transient. The influence of the travelling waves on the flow turbulent structures is not restricted to the

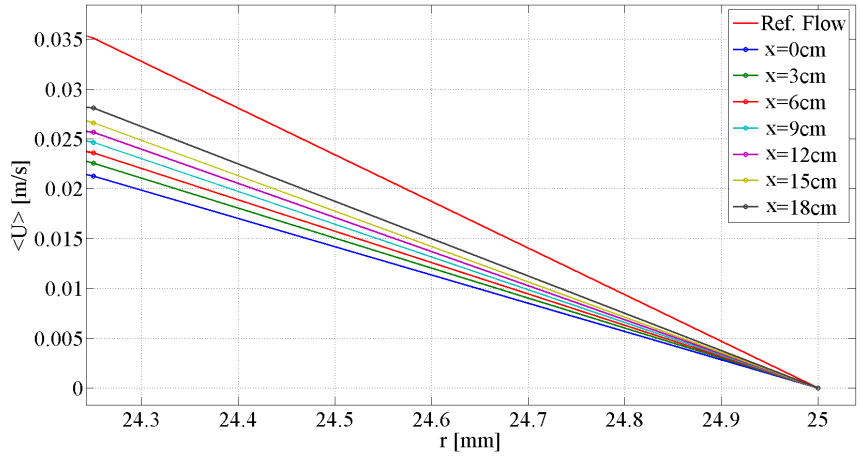

Figure 5.10: *A zoom of the comparison between mean velocity profile at different axial position at* $A^+ = 12$ *and* $Re_\tau \simeq 179$ *for* $k_{6s}^+ = 0.004$. *The reference flow is unmarked.*

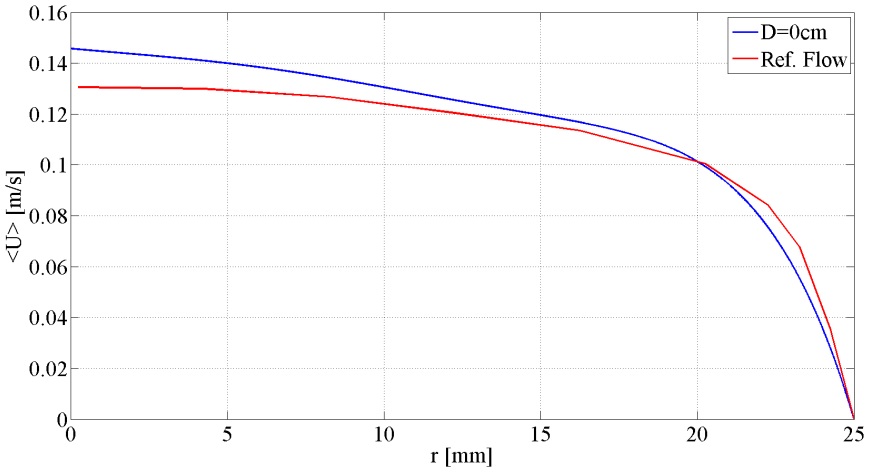

Figure 5.11: *Comparison between mean velocity profile at* $x = 0\ cm$ *(circles) at* $A^+ = 12$ *and* $Re_\tau \simeq 179$ *for* $k_{6s}^+ = 0.004$ *and the reference flow.*

near wall region but extend to the whole flow as shown in figures 5.14 and 5.15, where $\langle u^2 \rangle$ is normalized with u_τ of the reference flow. Each map was computed after a linear interpolation of the data acquired.

The Reynolds stress slowly increases moving away from the active section but its behaviour seems to be slightly slower com-

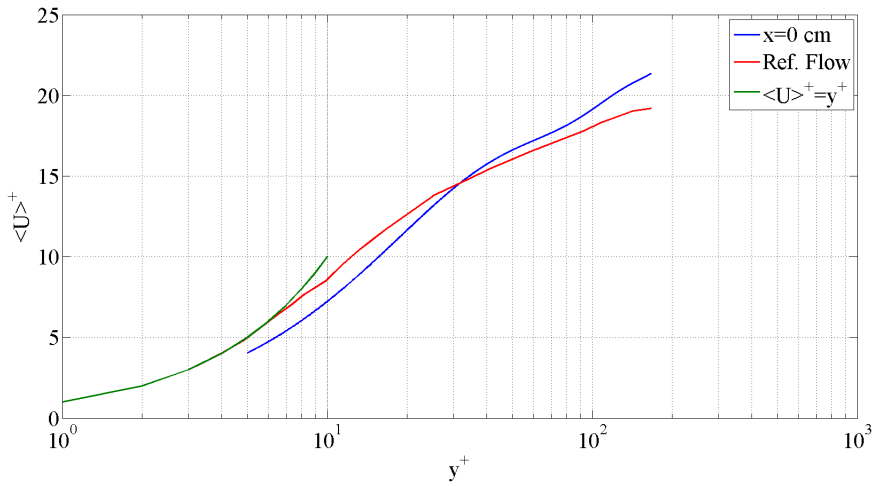

Figure 5.12: *Comparison between mean velocity profile at $x = 0\ cm$ (circles) at $A^+ = 12$ and $Re_\tau \simeq 179$ for $k_{6s}^+ = 0.004$ and the reference flow in viscous units. The law of the wall is represented by the green line.*

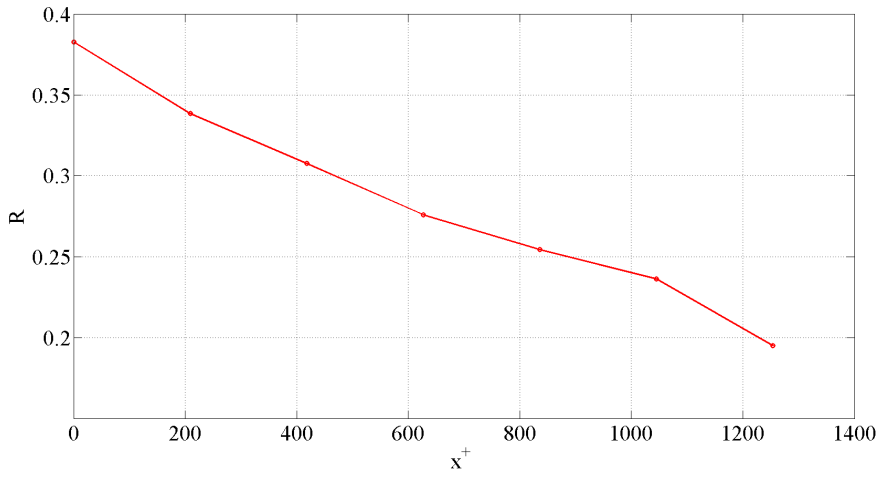

Figure 5.13: *Drag reduction rate spatial transient along the streamwise direction downstream the active section of the flow from $x^+ = 0$ to $x^+ \simeq 1250$ at $A^+ = 12$ and $Re_\tau \simeq 179$ for $k_{6s}^+ = 0.004$.*

pared to that of drag reduction. In Figure 5.16 u_{rms} at $x = 0\ cm$ and $x = 6\ cm$ positions is compared to u_{rms} of the reference flow. The turbulence intensity is lower at the outlet of the active section with a peak located at a longer distance from the wall in respect to the reference flow: this effect is largely due

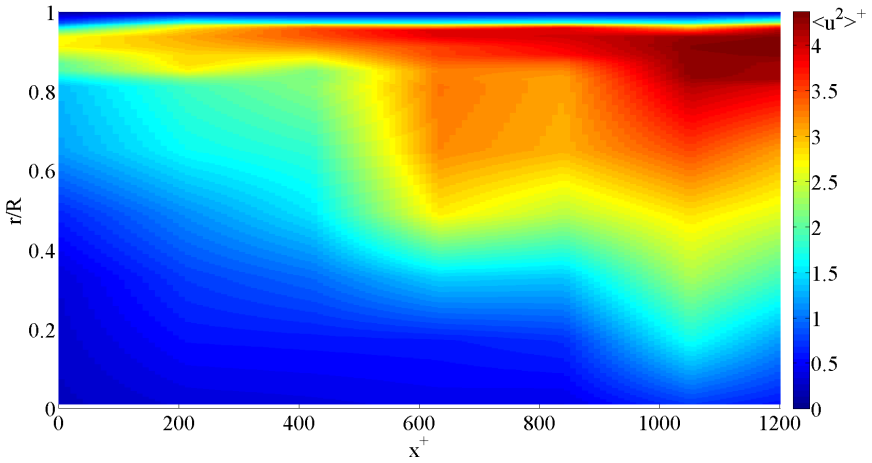

Figure 5.14: *Map of* $\langle u^2 \rangle^+$ *in the spatial transient at* $A^+ = 12$ *and* $Re_\tau \simeq 179$ *for* $k_{6s}^+ = 0.004$ *from* $x^+ = 0$ *to* $x^+ \simeq 1250$. $\langle u^2 \rangle^+$ *at each axial position is normalized with* u_τ *of the reference flow.*

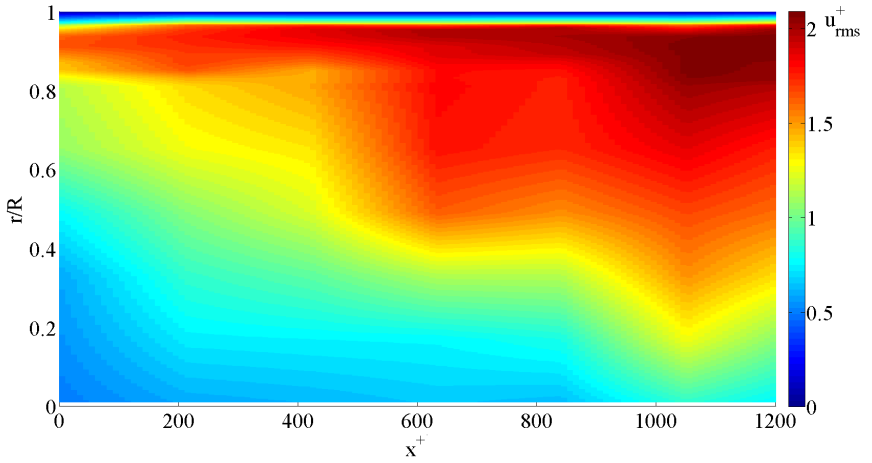

Figure 5.15: *Map of* u_{rms}^+ *in the spatial transient at* $A^+ = 12$ *and* $Re_\tau \simeq 179$ *for* $k_{6s}^+ = 0.004$ *from* $x^+ = 0$ *to* $x^+ \simeq 1250$. u_{rms}^+ *at each axial position is normalized with* u_τ *of the reference flow.*

to the presence of the generalized Stokes layer, that influences the near wall quantities and slowly decreases as the flow leaves the active section. However the curves obtained are too sharp and better results in terms of mean values and curve smoothness could be achieved with longer sampling time.

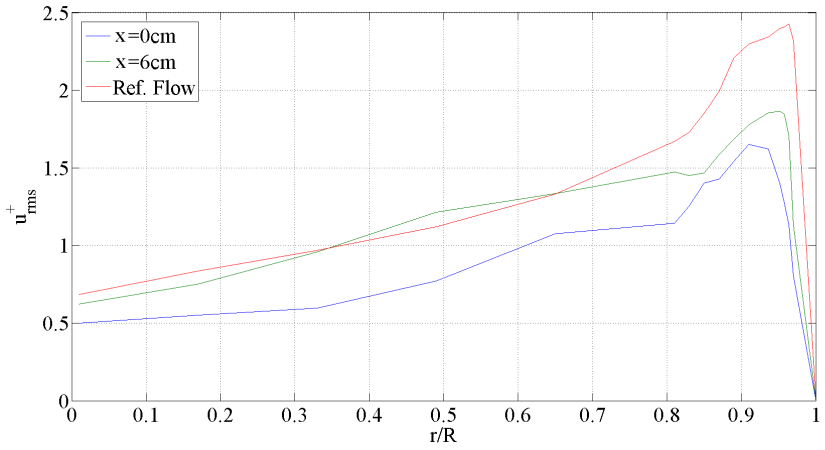

Figure 5.16: *u^+_{rms} as a function of the adimensional radius at different axial position at $A^+ = 12$ and $Re_\tau \simeq 179$ for $k^+_{6s} = 0.004$. $x = 0\ cm$ (blue line), $x = 6\ cm$ (green line) and reference flow (red line). u^+_{rms} at each axial position is normalized with u_τ of the reference flow.*

.

5.4 Turbulent kinetic energy

In this section the turbulent kinetic energy spectra measured at $x^+ = 0$ are presented and compared to the reference flow spectra. The turbulent kinetic energy is defined as the trace of the Reynolds stress tensor:

$$E_k = \frac{1}{2}\left(u^2 + v^2 + w^2\right) \tag{5.12}$$

where we adopted the notation defined in 4.2. As described in 4.2 with our setup we are able to measure only the streamwise velocity fluctuation and thus the spectra obtained are only an approximation of the real spectra:

$$E_k \simeq \frac{1}{2}u^2 \tag{5.13}$$

However the radial velocity fluctuation is a second-order term and thus can be neglected. Because of the rotation of the slabs, in the near-wall region the azimuthal velocity is of the order of

the streamwise one and thus its influence has been taken into account calculating the stramwise velocity as suggested by Ricco and Wu in [31]:

$$U = \sqrt{U_{meas}^2 - k_T W_{GSL}^2} \tag{5.14}$$

where W_{GSL} is the generalized Stokes layer solution as described in 4.3. However those measurements are corrected for the channel flow analytical solution of the azimuthal component and thus a low influence of segments motion is still recognizable in the spectra. The experimental campaign was carried out at a fixed value of $Re = 4900$ and $A = 0.079\ m/s$. We investigated the spectra for six different frequencies and for two different wave numbers, $k_{3s} = 57.33\ 1/m$ and $k_{6s} = 28.66\ 1/m$. For each frequency the radial run is discretized by means of 16 points; each measurement point consists of an acquisition of 120 s at a frequency of 20 kHz, with a settling time of 20 s. The acquisition time has been reduced in order to carry the experiments at a fixed wavelength in a single day because some frequencies required several acquisitions until a good discretization of the wave was achieved. The parameters employed in this campaign are shown in the table 5.4. For each measurement point the voltage signal was converted into velocity and was divided into 30 s signals with a 50% overlap and then a Hanning window was applied. Finally, the signals are transformed by means of FFT and averaged in order to suppress noise.

Table 5.4: *Experimental parameters of the turbulent kinetic energy spectra campaign*

Re_{tau}	A^+	ω^+	**Sampl.rate[kHz]**	**Sampl.period[s]**
179	12	$-0.1 \div 0.1$	20	120

In Figures 5.17 and 5.18 the turbulent kinetic energy spectra at $y^+ = 5$ at different travelling wave frequencies are compared with the reference flow spectra at the same location in order

to evaluate the influence of the drag reduction device. In each spectrum the peak located at twice the frequency of the travelling wave (because of signal rectification) has been suppressed by the correction. For both the wave numbers, slow forward-travelling waves largely modify the whole spectrum while faster forward-travelling waves and backward-travelling waves are not as effective in turbulence suppression. Furthermore, the waves discretized with 6 segments seem to be more effective than those discretized with 3 segments in the spectrum low frequency region. However this region is influenced by the wall motion, which frequency is in the range $-0.7 \div 0.7\ Hz$, and thus the real spectra may differ from the shown ones. An analysis of the influence of the drag reduction as function of the distance from the wall was carried out for $k_{6s}^{+} = 0.004$ and $\omega^{+} \simeq 0.01$ and the results are shown in Figure 5.19. The travelling wave effect on the energy spectrum slowly decreases as the distance from the wall increases as expected: when drag reduction occurs the wall-cycle of the turbulent structures is weakened and the turbulent production is therefore interrupted in accordance with Karniadakis and Choi in [23]. The mechanism of drag reduction seems to be very effective only in the $y^{+} < 15$ region and thus changes at the flow centerline are only a resulting effect of the modification of the near-wall region and are exclusively related to mean flow.

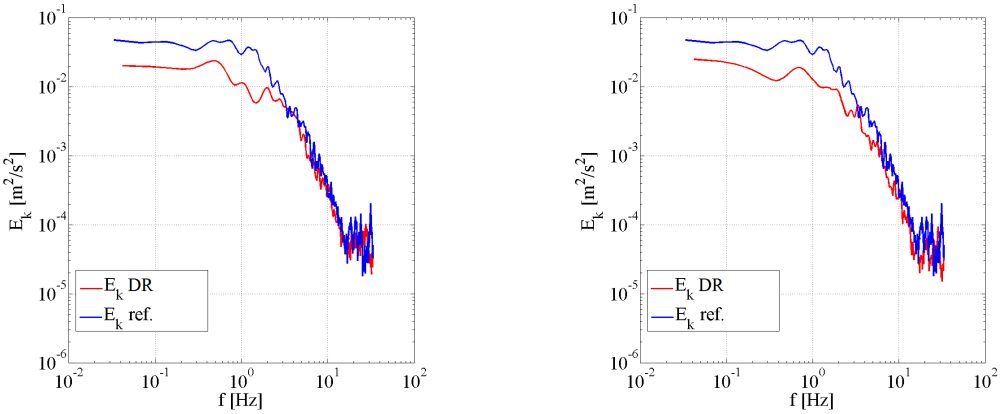

(a) $f = -0.7\ Hz$ **(b)** $f = -0.35\ Hz$

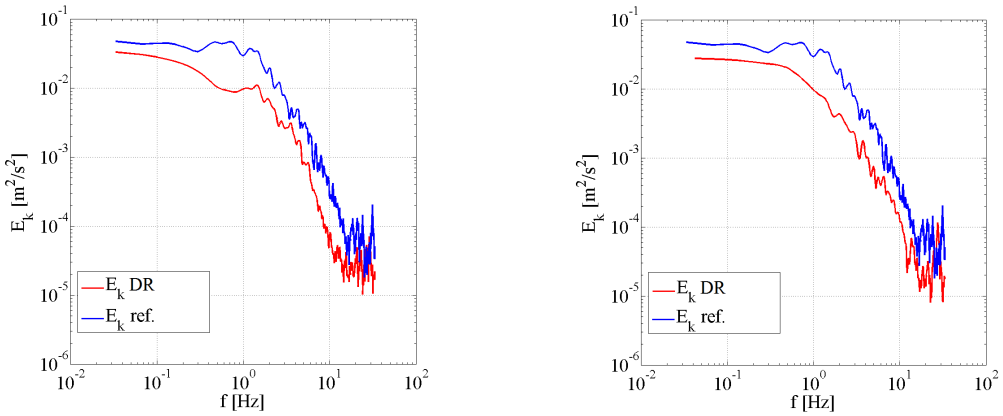

(c) $f = 0.07\ Hz$ **(d)** $f = 0.14\ Hz$

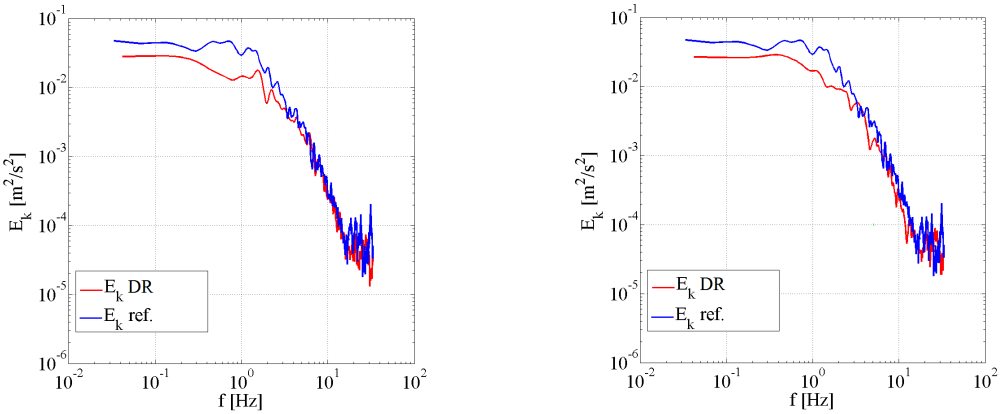

(e) $f = 0.35\ Hz$ **(f)** $f = 0.7\ Hz$

Figure 5.17: *Turbulent kinetic energy spectra at* $A^+ = 12$ *and* $Re_\tau \simeq 179$ *for* $k_{6s}^+ = 0.004$ *for six different frequencies of the wall forcing. Reference flow (blue line).*

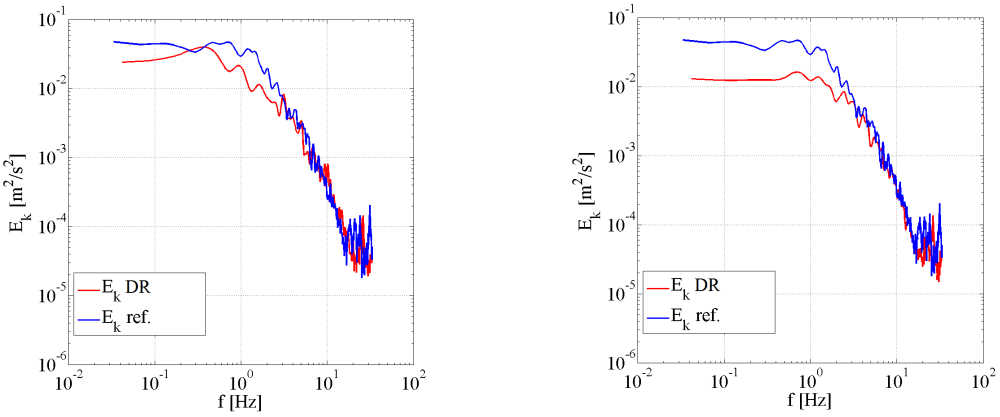

(a) $f = -0.7\ Hz$ **(b)** $f = -0.35\ Hz$

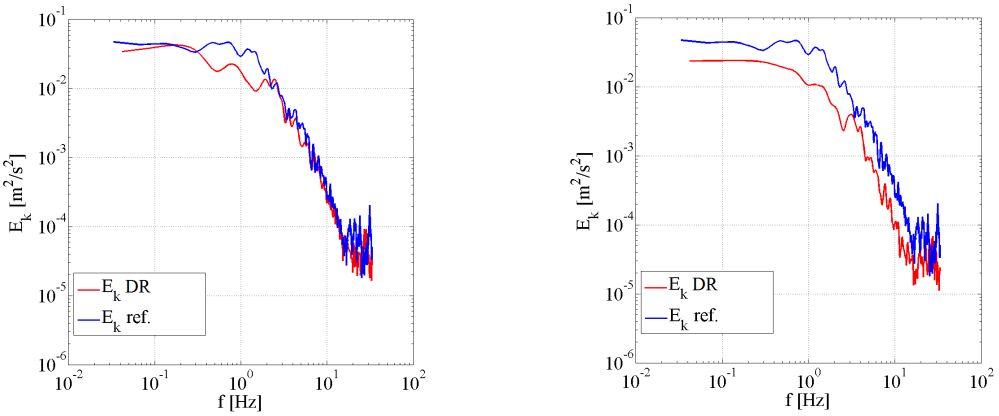

(c) $f = 0.07\ Hz$ **(d)** $f = 0.14\ Hz$

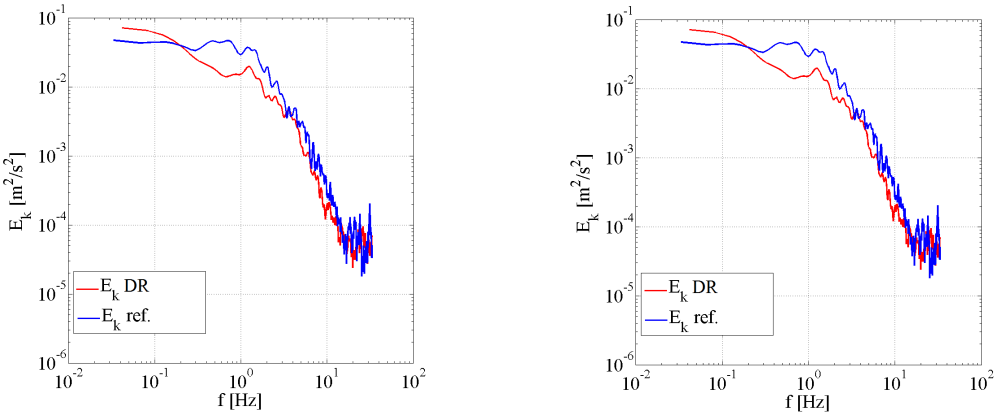

(e) $f = 0.42\ Hz$ **(f)** $f = 0.7\ Hz$

Figure 5.18: *Turbulent kinetic energy spectra at* $A^+ = 12$ *and* $Re_\tau \simeq 179$ *for* $k_{3s}^+ = 0.008$ *for six different frequencies of the wall forcing. Reference flow (blue line).*

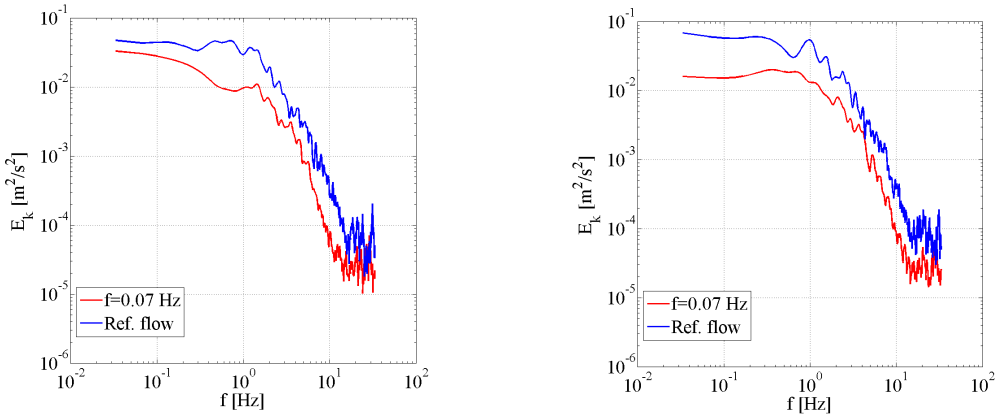

(a) $y^+ = 5$ **(b)** $y^+ = 6$

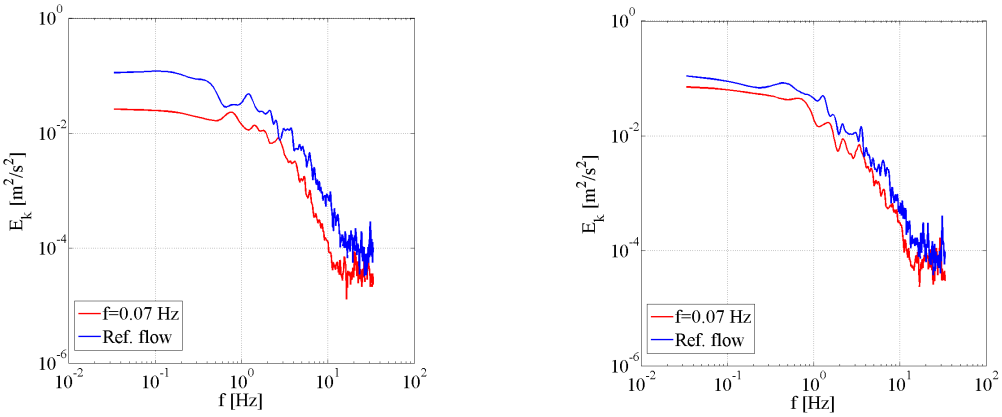

(c) $y^+ = 7$ **(d)** $y^+ = 8$

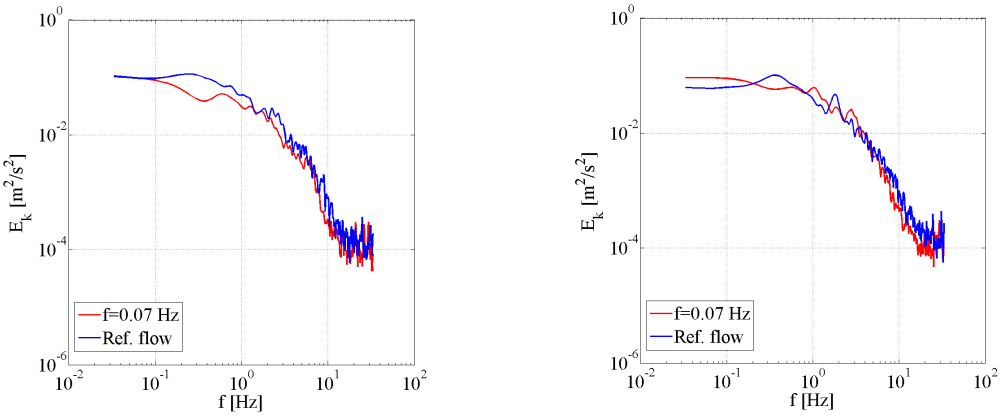

(e) $y^+ = 11$ **(f)** $y^+ = 15$

Figure 5.19: *A comparison of turbulent kinetic energy spectra with those of the reference flow at* $A^+ = 12$ *and* $Re_\tau \simeq 179$ *for* $k_{6s}^+ = 0.004$ *at different distance from the wall. Reference flow (blue line).*

Chapter 6

Conclusions

The experimental campaigns carried out in this thesis have required a lot of effort in the maintenance of the complex facility and a careful attention to the use of an hot-film for measurements in water at very low flow velocity. The calibration procedure to take into account the temperature drift was fundamental in order to achieve a great repeatability and accuracy in the measurements. Because of the nature of our setup the evaluation of the Jorgensen tangential coefficient was performed in order to correct the near-wall streamwise velocity.

The drag reduction campaign carried out by means of a pressure transducer is in good agreement with direct numerical simulation, mostly from a qualitative point of view. The quantitative discrepancies were mainly addressed to the presence of a spatial transient at the beginning of the active section of the pipe, where the drag reduction mechanism develops. For few frequencies the turbulent skin-friction has been evaluated by means of the mean streamwise velocity slope at the wall and the results show higher drag reduction rate, confirming the influence of the transient.

The spatial transient at the outlet of the drag reduction device shows an increase of the turbulent friction from the regulated level to the unperturbed one as the distance from the outlet of the active section increases and thus a decrease of the drag reduction rate. A general increase of turbulent statistics

was observed along the transient and furthermore the peak of turbulence slowly moves toward the wall as the distance from the outlet increases.

Eventually turbulent energy spectra at the outlet of the active section of the pipe were measured showing a weakening of the wall turbulent structures, especially for slow forward-travelling waves, as expected from drag reduction measurements and direct numerical simulation. However the low frequency spectra are influenced by the velocity induced by wall motion and the results are not as good as those in the high frequency spectra.

Future developments

The whole experimental campaign was carried out at fixed Re and A and thus a parametric investigation of the actual influence of these two parameters on the drag reduction mechanism should be verified.

The drag reduction rate analysis by means of near-wall velocity measurements could be extended to a wider frequency range in order to obtain a better comparison with the numerical data.

A more accurate analysis of the turbulent flow could be achieved by introducing a transparent pipe at the outlet of the active section of the pipe in order to carry out the measurements by means of laser Doppler velocimetry or stereoscopic PIV. In this way a longer length of the spatial transient could be analyzed and thus any influence of the azimuthal component of the velocity on the measurements could be avoided.

Furthermore, the turbulent skin friction reduction could be experimentally achieved in a completely new way by means of streamwise travelling wave of radial wall velocity (i.e peristalsis) that could lead to a complete relaminarization of the flow at low Reynolds numbers, as observed in direct numerical analysis.

Bibliography

[1] M. Gad-el Hak. Flow control: the future. *Journal of Aircraft*, 38(3):402–418, 2001.

[2] M. Gad-el Hak. *Flow control: passive, active, and reactive flow management*. Cambridge University Press, 2000.

[3] A. G. Kravchenko, H. Choi, and M. Parviz. On the relation of near-wall streamwise vortices to wall skin friction in turbulent boundary layers. *Physics of Fluids A*, 5(12), 1993.

[4] W. J. Jung, N. Mangiavacchi, and F. L. Akhavan. Suppression of turbulence in wall-bounded flows by high-frequency spanwise oscillations. *Physics of Fluids A*, 8:1605–1607, 1992.

[5] A. Baron and M. Quadrio. Turbulent drag reduction by spanwise wall oscillations. *Applied Scientific Research*, 55:311–326, 1996.

[6] C. Viotti, M. Quadrio, and P. Luchini. Streamwise oscillation of spanwise velocity at the wall of a channel for turbulent drag reduction. *Physics of Fluids*, 21, 2009.

[7] M. Quadrio, P. Ricco, and C. Viotti. Streamwise-traveling waves of spanwise wall velocity for turbulent drag reduction. *Physics of Fluids*, 2009.

[8] F. Auteri, A. Baron, M. Belan, G. Campanardi, and M. Quadrio. Experimental assessment of drag reduction by traveling waves in a turbulent pipe flow. *Physics of Fluids*, 22, 2010.

[9] S. Raina. Studio e realizzazione di un sistema a film caldo per misure in flussi interni turbolenti. Master's thesis, Politecnico di Milano, 2013.

[10] C. Tropea, A. L. Yarin, and J. F. Foss. *Handbook of experimental fluid mechanics*. Springer, 2007.

[11] J. P. J. van Beeck, L. Vervisch, D. Veynante, and J-.M. Buchlin. *VKI lecture series*. Von Karman Institute for Fluid Dynamics, 2007.

[12] H. Leschziner, H. Choi, and K.-S. Choi. Flow control approaches to drag reduction in aerodynamics. *Phil. Trans. R. Soc. A*, 369(1940):1349–1351, 2011.

[13] S. B. Pope. *Turbulent flows*. Cambridge University Press, 2000.

[14] S. J. Kline and S. K. Robinson. *Quasi-coherent structures in the turbulent boundary layer. I - Status report on a community-wide summary of the data*, pages 200–217. Routledge, 1989.

[15] W. W. Willmarth and S. S. Lu. Structure of the reynolds stress near the wall. *Journal of Fluid Mechanics*, 55:65–92, 1972.

[16] J. M. Wallace, R. S. Brodkey, and H. Eckelmann. Pattern-recognized structures in bounded turbulent shear flows. *Journal of Fluid Mechanics*, 83:673–693, 1977.

[17] J. Jimenez and A. Pinelli. The autonomous cycle of near-wall turbulence. *Journal of Fluid Mechanics*, 389:335–359, 1999.

[18] M. Quadrio and P. Ricco. Critical assessment of turbulent drag reduction through spanwise wall oscillations. *Journal of Fluid Mechanics*, 521:251–271, 2004.

[19] F Laadhari, L. Skandaji, and R. Morel. Turbulence reduction in a boundary layer by a local spanwise oscillating surface. *Physics of Fluids A*, 6:3218–3220, 1994.

[20] K.-S. Choi and M. Graham. Drag reduction of turbulent pipe flows by circular-wall oscillation. *Physics of Fluids*, 10:7–9, 1998.

[21] J. Kim and F. Hussain. Propagation velocity of perturbations in turbulent channel flow. phys. fluids. *Physics of Fluids A*, 5(3):695–706, 1993.

[22] Y. Du, V. Symeonidis, and G. E. Karniadakis. Drag reduction in wall-bounded turbulence via a transverse travelling wave. *Journal of Fluid Mechanics*, 457:1–34, 2002.

[23] G. E. Karniadakis and K.-S. Choi. Mechanisms on transverse motions in turbulent wall flows. *Annual Review of Fluid Mechanics*, 35:45–62, 2003.

[24] A. Bertolucci. Studio sperimentale di onde viaggianti in flussi turbolenti di parete. Master's thesis, Politecnico di Milano, 2010.

[25] C. G. Lomas. *Fundamentals of Hot Wire Anemometry.* Cambridge University Press, 1986.

[26] F. E. Jorgensen. Directional sensitivity of wire and fiber film probes. *DISA inf.*, 11:31–37, 1971.

[27] G. Lemonis and T. Dracos. A new calibration and data reduction method for turbulence measurement by multi-hotwire probes. *Exp. Fluids*, 18:319–328, 1995.

[28] J. M. J. den Toonders and T. M. Nieuwstadt. Reynolds number effects in a turbulent pipe flow for low to moderate re. *Physics of Fluids*, 9:3398–3409, 1997.

[29] M. Quadrio and P. Ricco. The laminar generalized stokes layer and turbulent drag reduction. *Journal of Fluid Mechanics*, 667:135–157, January 2011.

[30] M. Biggi. Riduzione di resistenza in flussi turbolenti di parete: confronto tra esperimenti e simulazione numerica diretta. Master's thesis, Politecnico di Milano, 2012.

[31] P. Ricco and S Wu. On the effects of lateral wall oscillations on a turbulent boundary layer. *Experimental Thermal and Fluid Science*, 29:41–52, 2004.

Appendix A

Estratto in lingua italiana

In questa appendice viene riportato un estratto del contenuto della tesi in lingua italiana.

A.1 Introduzione

La possibilità di poter controllare determinati tipi di flussi è sicuramente una delle sfide più interessanti in ambito fluidodinamico. Tra i differenti obiettivi di controllo figurano certamente l'aumento della portanza, la riduzione della resistenza, il ritardo della transizione e la possibilità di evitare la separazione. La riduzione della resistenza rappresenta certamente la sfida di più complicata e di maggiore interesse industriale. Sebbene siano stati sviluppati dispositivi di controllo attivi e passivi, i primi garantiscono delle prestazioni decisamente migliori. Per quanto riguarda i flussi in condotti circolari, tra le tecniche di controllo attivo in anello aperto la più promettente risulta essere senza dubbio l'applicazione di onde longitudinali viaggianti di velocit à azimutale di parete come mostrato in figura A.1. L'equazione generale di tale onde è la seguente:

$$W_w(x,t) = Asin(k_x x - \omega t) \tag{A.1}$$

Tali oscillazioni si traducono in una generale diminuzione delle strutture turbolente a parete e dunque in una diminuzione dello sforzo turbolento a parete. I risultati sperimentali ottenuti sono alquanto incoraggianti, con una riduzione massima di resistenza ottenuta di circa il 33%. Tali risultati, in presenza di un adeguato sistema di attuazione delle onde viaggianti, permetterebbero un bilancio netto di energia decisamente positivo. Lo scopo principale di questa tesi è l'analisi sperimentale, mediante anemometria a film caldo, del transitorio spaziale che si genera a valle della sezione attiva del tubo, al fine di comprendere al meglio i meccanismi di soppressione della turbolenza.

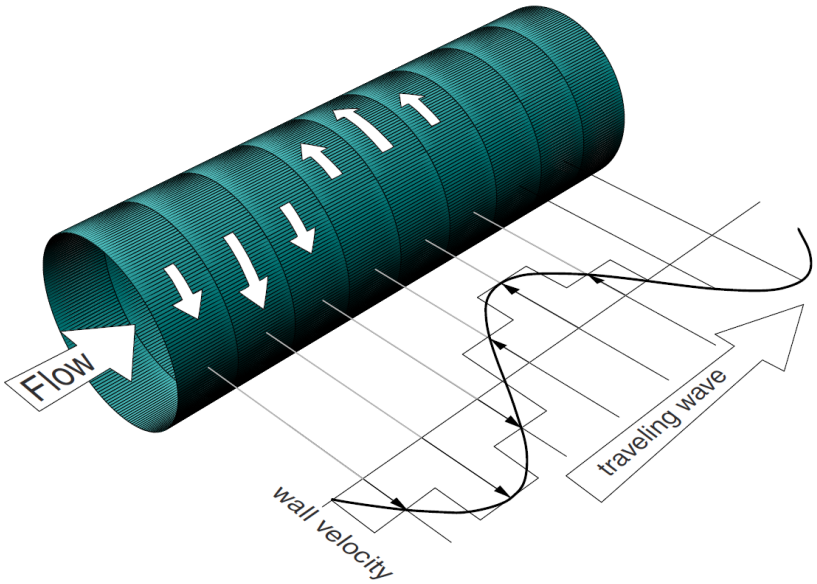

Figure A.1: *Implementazione della tecnica delle onde viaggianti in un condotto a sezione circolare*

A.2 Descrizione dell'impianto

Le prove sperimentali sono state svolte al laboratorio di aerodinamica del politecnico di Milano nell'impianto mostrato in figura A.2.

La sezione attiva del nostro impianto presenta un diametro $D = 50\ mm \pm 0.05\ mm$ ed una lunghezza totale di circa $44D$. Le onde viaggianti vengono generate per mezzo di 60 segmenti rotanti azionati da 6 motori indipendenti. La sezione attiva è collegata alla pompa centrifuga mediante un condotto rigido d'alluminio lungo circa $50D$ in cui è situata la strumentazione per il supporto del film caldo. Il condotto di ritorno, in cui è situato il flussimetro magnetico, presenta un diametro leggermente inferiore. Prima della sezione attiva è presente un ulteriore condotto rigido d'alluminio lungo $120D$ in cui è presente un nido d'ape per ottenere un flusso quanto più uniforme. L'impianto è dotato inoltre di un vaso di espansione per garantire una pressione interna leggermente superiore a quella esterna, per evitare che il grasso presente tra i segmenti contamini il flusso. Per le di-

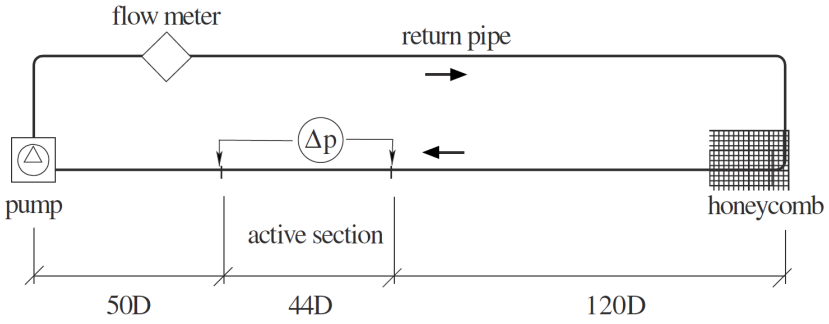

Figure A.2: *Apparato sperimentale a circuito chiuso di sezione circolare composto da una sezione attiva, una pompa centrifuga, un condotto di ritorno con flussimetro e nido d'ape.*

verse campagne sperimentali sono stati utilizzati un flussimetro magnetico per misurare la portata del flusso, una sonda PT100 per misurare la temperatura, un trasduttore di pressione barometrico per misurare la pressione nell'impianto e un trasduttore differenziale di pressione al fine di misurare la perdita di carico a cavallo della sezione attiva.

A.3 Risoluzione dei problemi

L'impianto di supporto della sonda a film caldo risultava decisamente compromesso e dunque non è stato possibile procedere immediatamente con la campagna sperimentale. I principali problemi riscontrati sono stati:

- Scarsa movimentazione assiale a causa dell'attrito delle molle di ritorno dell'albero porta sonda.
- Movimentazione assiale insufficiente per l'indagine della regione a parete.
- Instabilità dell'apparato a causa di un cattivo serraggio di uno dei supporti verticali.
- Impossibilitdì retrazione del cavo del film caldo, con conseguente rischio per la sonda.
- Fuoriuscita delle boccole premistoppa dalla loro sede durante la movimentazione.
- Impossibilità di una ripetibilità del posizionamento radiale.

La risoluzione di tali problemi ha richiesto un'attenta analisi e diverse settimane di lavoro ed una successiva calibrazione del posizionamento assiale e radiale della sonda.

A.4 Anemometria a filo caldo

Le misure di velocità sono state effettuate mediante anemometria termica mediante una sonda a film caldo per misure di strato limite. A causa delle bassissime velocità del flusso è stata necessaria un'accurata procedura di calibrazione, soprattutto per tener conto dell'aumento di temperatura del flusso durante l'esecuzione delle prove, come mostrato in figura A.3.

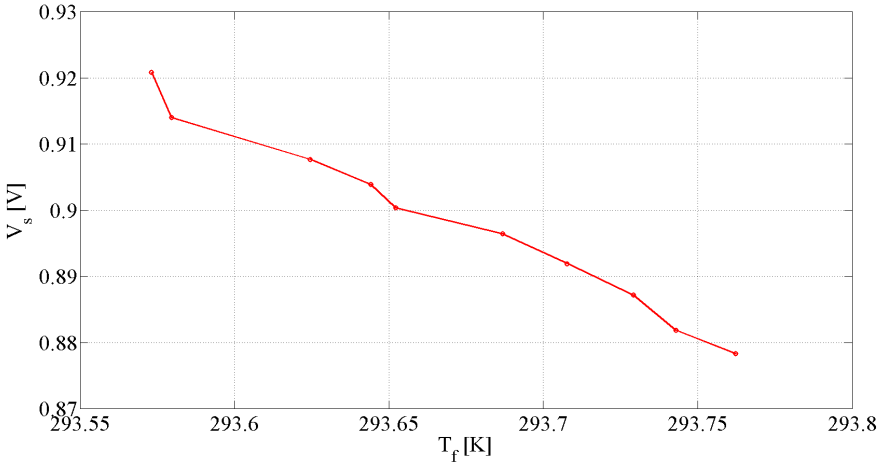

Figure A.3: *Tensione in uscita dall'anemometro in funzione della temperatura del fluido*

Il supporto della sonda a film caldo presentava inoltre un declino, dovuto al gioco meccanico tra albero principale e albero portasonda, nelle configurazioni ad albero esteso. Questo si traduceva in un impreciso posizionamento della sonda e dunque si sono rese necessarie delle prove per individuare correttamente il centro vena del flusso.

A.5 Risultati

Prima di procedere con le prove sperimentali è stato necessario misurare sperimentalmente il coefficiente di influenza del flusso azimutale sulle misure ottenute mediante film caldo. Tale valore è stato poi utilizzato per poter correggere le misure effettuate nella regione a parete in prossimità della sezione attiva, valutando la componente di velocità azimutale attraverso la soluzione laminare dello strato limite di Stokes generalizzato e sottraendola all'effettivo segnale misurato. Per valutare gli effetti della discretizzazione dell'onda e delle diverse frequenze della forzante applicata sono state svolte varie prove sperimen-

tali a numero di Reynolds $Re = 4900$ ed ampiezza dell'onda $A = 0.079\ m/s$ fissati. Per due differenti numeri d'onda, $k_{3s} = 57.33\ 1/m$ and $k_{6s} = 28.66\ 1/m$ (che corrispondono rispettivamente a 3 e 6 segmenti indipendenti), è stato analizzato un intervallo di frequenze $f = -1.5 \div 1.5\ Hz$. In figura A.4 viene proposto un confronto tra le misure di riduzione di resistenza ottenute con un'onda discretizzata mediante 3 segmenti ed un'onda discretizzata con 6. In entrambi i casi il valore percentuale massimo di riduzione riscontrato risulta $R \simeq 0.35\%$. I dati forniti dalle simulazioni numeriche indicano chiaramente che l'onda con numero d'onda maggiore dovrebbe fornire un picco di riduzione di resistenza decisamente maggiore. Risulta dunque che i risultati ottenuti a k_{3s} risento maggiormente degli effetti della discretizzazione. In figura A.5 vengono confrontate le misure di riduzione di resistenza ottenuta sperimentalmente a k_{3s} e quelle ottenute mediante simulazioni numeriche con onde viaggianti discretizzate. Il comportamento qualitativo dell'onda rispecchia pienamente quello delle simulazioni numeriche e le discrepanze qualitative sono dovute principalmente ad una lieve differenza nell'ampiezza dell'onda nei due casi (l'ampiezza del caso numerico è leggermente maggiore) e alla presenza nella prova sperimentale, nella prima parte della sezione attiva, di un transitorio spaziale in cui gli effetti dell'onda viaggiante si sviluppano.

È stata inoltre svolta un'analisi del transitorio spaziale a valle della sezione attiva dell'impianto, in cui il flusso controllato lentamente ritorna nella condizione indisturbata. Le misure sono state ottenute mediante un film caldo singolo per una lunghezza totale a valle della sezione attiva di $18cm$. Per tale prova sono stati utilizzati i medesimi valori di Re ad A della campagna sperimentale della riduzione di resistenza con una frequenza di oscillazione fissata a $f = 0.07\ Hz$, un valore prossimo a quello di massima resistenza. Le misure sono state effettuate in 7 dif-

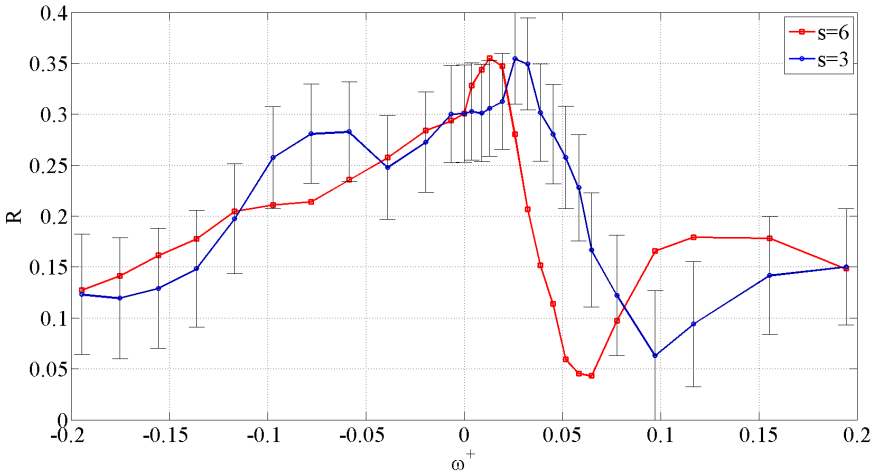

Figure A.4: *Rateo di riduzione della resistenza in funzione della frequenza dell'oscillazione per s=3(cerchi) e s=6(quadrati).* $k_{3s}^{+} = 0.008$ *(cerchi) and* $k_{6s}^{+} = 0.004$ *(quadrati).*

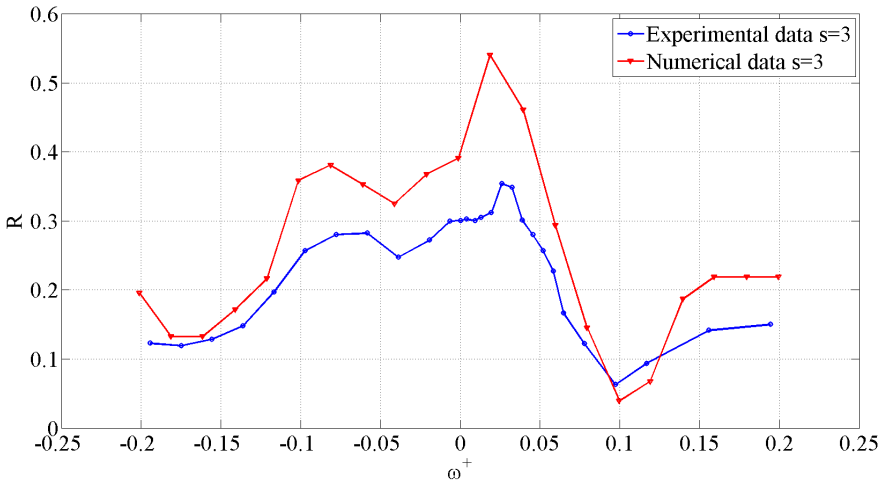

Figure A.5: *Confronto tra la riduzione di resistenza ottenuta sperimentalmente e quella numerica in funzione della frequenza dell'oscillazione per* $k_{3s}^{+} = 0.008$. *Le simulazioni numeriche (triangoli) sono state svolte ad* $A^{+} = 14.3$ *e* $Re_{\tau} \simeq 169$, *mentre quelle sperimentali ad* $A^{+} = 12$ *and* $Re_{\tau} \simeq 179$

ferenti sezioni assiali equispaziate.

In figura A.6 è mostrato un evidente aumento della pendenza del profilo di velocità medio a parete, e pertanto un aumento della resistenza d'attrito, all'aumentare della distanza

dalla sezione attiva. Risulta inoltre molto evidente in figura A.7 che l'influenza delle onde viaggianti non è limitata alla sola zona in prossimità della parete: lo sforzo di Reynolds assiale tende infatti ad aumentare sia in direzione assiale che radiale lungo tutto il transitorio.

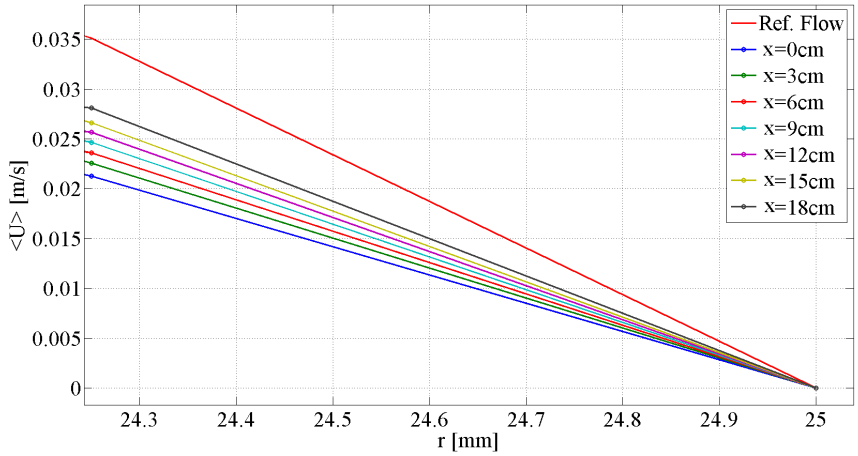

Figure A.6: *Confronto della pendenza a parete del profilo medio di velocità in differenti sezioni assiali per* $A^+ = 12$ *e* $Re_\tau \simeq 179$.

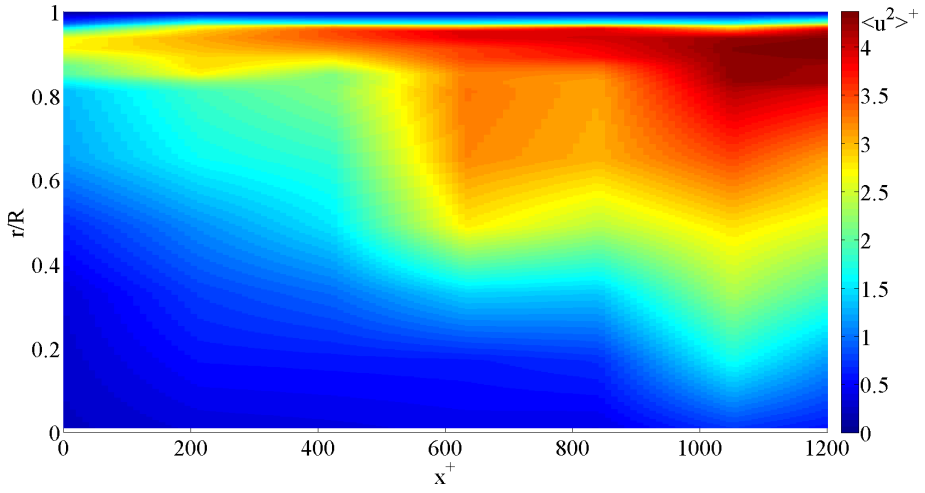

Figure A.7: *Mappa di* $\langle u^2 \rangle^+$ *nel transitorio spaziale a valle della sezione attiva da* $x^+ = 0$ *a* $x^+ \simeq 1250$. $\langle u^2 \rangle^+$ *è normalizzato con* u_τ *del flusso base.*

Appendix B

Error propagation

In this appendix the residual sum of squares (RSS) is illustrated in order to deduce some quantitative information about measures accuracy.

B.1 Friction coefficient accuracy

The drag reduction rate results shown in 5.2 have been deduced from an estimation of the friction coefficient f by means of the pressure drop along the active section and by means of the mean velocity gradient at the wall. In both measurements the error can be estimated by means of RRS starting from the accuracy of the instruments used. In the first case the friction coefficient has been evaluated through the definition:

$$f = \frac{2\Delta p}{\rho U_b^2 L/D} \tag{B.1}$$

Each quantity in equation B.1 is affected by error:

- The pressure drop has been measured using a $-2-2\ mbar$ $\pm$ 0.1% Druck LPM9481 pressure transducer.
- The temperature, which affects density and viscosity, has been measured using a PT100 thermocouple with accuracy of $\pm 0.2\ K$.

- The bulk velocity has been measured by means of a magnetic flow meter with 0.2% accuracy.
- The diameter of the pipe has a $\pm 0.05\ mm$ accuracy.
- The length of the active section has a $\pm 0.05\ mm$ accuracy.

The error in the evaluation of the friction coefficient has been calculated as:

$$e_f = \sqrt{\sum_i \left(\frac{\partial f}{\partial x_i} e_{x_i} \right)^2} \tag{B.2}$$

where $\frac{\partial f}{\partial x_i}$ represents the influence of a generic quantity x_i on the measurement of f and e_{x_i} is the uncertainty in the measurement of the quantity x_i. The drag reduction rate has been calculated according to:

$$R = 1 - \frac{f}{f_0} \tag{B.3}$$

As the uncertainty of f_0 is of the same order of the uncertainty of f, the uncertainty of R can be evaluated by means of RSS as previously done. As shown in figure 5.3 the uncertainties in the measurements of R by means of the pressure drop are of the order of 0.05. The larger source of error is the uncertainty on the pressure drop measurement, because the pressure transducer full scale is too large for our measurements (the requirement of water filling made its use unavoidable).

The same process can be applied to hot-wire measurements where f is defined as:

$$f = \nu \frac{\langle U \rangle}{y U_b^2} \tag{B.4}$$

where y is the distance from the wall and $\langle U \rangle$ is the mean streamwise velocity at y. From the calibration procedure described in 4.3 the standard deviation of velocity measurements is

0.0012 m/s and the error in the probe placement can be consider of the order of the viscous length $l_\nu = 0.15\ mm$. This statement has been verified by moving the probe toward the wall with a l_ν step starting from the reference wall position shown in figure 4.14: the velocity signal acquired was higher because the grab screw, that had reached the wall, caused a temporary bend of the probe support resulting in a larger distance of the hot-film from the wall. Once the error in the evaluation of f was measured, the drag reduction rate has been calculated according to B.3 and thus the error in the evaluation of f_0 has to be taken into account in the hot-film measurements too. The uncertainties on the friction coefficient are shown in figure 5.8 and are of the order of 0.04.